



Radar Systems and
Remote Sensing Laboratory

NASA-CR-199644

PSB
NASA
IN-47-CR
5617
p. 122



(NASA-CR-199644)

~~(NIPS-95-05617)~~ RADIOMETRIC
CORRECTION OF SCATTEROMETRIC WIND
MEASUREMENTS (Kansas Univ. Center
for Research) 122 p

N96-13225

Unclas

G3/47 0072812

THE UNIVERSITY OF KANSAS CENTER FOR RESEARCH, INC.

2291 Irving Hill Road
Lawrence, Kansas 66045-2969

**RADIOMETRIC CORRECTION OF
SCATTEROMETRIC WIND MEASUREMENTS**

Nalanimohan Kambhammettu

**Radar Systems and Remote Sensing Laboratory
Department of Electrical Engineering and Computer Science, University of Kansas
2291 Irving Hill Road, Lawrence, Kansas 66045-2969
TEL: 913/864-4835 * FAX: 913/864-7789 * E-MAIL: graham@ardneh.rsl.ukans.edu**

RSL Technical Report 9280-1

September 1995

Sponsored by:

**EOS subcontract through Jet Propulsion Laboratory
Pasadena CA 91109**

Document No. 959073

Abstract

Use of a spaceborne scatterometer to determine the ocean-surface wind vector requires accurate measurement of radar backscatter from ocean. Such measurements are hindered by the effect of attenuation in the precipitating regions over sea. The attenuation can be estimated reasonably well with the knowledge of brightness temperatures observed by a microwave radiometer.

The NASA SeaWinds scatterometer is to be flown on the Japanese ADEOS-II. The AMSR multi-frequency radiometer on ADEOS II will be used to correct errors due to attenuation in the SeaWinds scatterometer measurements. Here we investigate the errors in the attenuation corrections. Errors would be quite small if the radiometer and scatterometer footprints were identical and filled with uniform rain. However, the footprints are not identical, and because of their size one cannot expect uniform rain across each cell.

Simulations were performed with the SeaWinds scatterometer (13.4 GHz) and AMSR (18.7 GHz) footprints with gradients of attenuation. The study shows that the resulting wind speed errors after correction (using the radiometer) are small for most cases. However, variations in the degree of overlap between the radiometer and scatterometer footprints affect the accuracy of the wind speed measurements.

Contents

1	Introduction	1
1.1	Why Measure Wind Vector ?	1
1.2	Need for Satellite based Wind Vector Determination	1
1.3	Need for Integrated Scatterometer-Radiometer Systems	2
2	Scatterometry	4
2.1	Scatterometry	4
2.1.1	Components Of the Ocean	5
2.2	Measurement of Radar Backscatter from the sea	6
2.2.1	Azimuthal Variation of Radar Backscatter	7
2.2.2	Dependence of backscatter on the angle of incidence	10
2.2.3	Geophysical Model Function	10
2.2.4	The SASS model function	13
2.2.5	Need for multiple measurements	14
2.2.6	Drawbacks of earlier scatterometer systems	14
2.2.7	Requirements of scatterometer system	16
2.2.8	Advantages of scanning pencil-beam over fan-beam systems	17
3	Evaluation of atmospheric attenuation using radiometer	18
3.1	Radiometry	18
3.1.1	Theoretical background	19

3.1.2	Radiative transfer equation	20
3.1.3	Radiative transfer - Neglecting Scattering	21
3.1.4	Absorption Models	23
3.1.5	Effect of Scattering	24
3.1.6	Mie scattering	26
3.1.7	Rayleigh-approximation for scattering	28
3.1.8	Volume scattering	29
3.2	Cloud Models	33
3.2.1	Rain absorption coefficient	35
3.2.2	Porter and Kreiss cloud models	36
3.2.3	Valley Rain Model	38
3.3	Deirmendjian Models	39
3.3.1	Cloud Models	39
3.3.2	Comparison of Theoretical Results With and Without Pre- cipitation Scattering	44
3.4	Relation between Attenuation and Excess Apparent Temperature	46
3.4.1	Relation at Single Frequency	46
3.4.2	Errors of the attenuation estimate	51
3.4.3	Theoretical Relation at Different Frequencies	52
3.4.4	Frequency Dependence of the Absorption Coefficient at a Fixed Altitude	53
3.4.5	Attenuation vs. Excess Apparent Temperature at Different Frequencies	53
3.5	Dependence of Regression Coefficients on the Surface Parameters	53
3.5.1	Dependence on Surface Pressure	53
3.5.2	Dependence on Surface Water Vapor Density	55
3.5.3	Dependence on Surface Temperature	55
4	SeaWinds scatterometer & AMSR Radiometer	59

4.1	SeaWinds Scatterometer	59
4.2	AMSR Radiometer	62
5	Simulations	63
5.1	Different stages in simulation	63
5.2	Simple cases to illustrate correction algorithm	64
5.2.1	Identical scatterometer & radiometer cells	64
5.2.2	Simulation results for some simple cases	71
5.2.3	Simulation results for cases with more than one sub-cell . .	73
5.2.4	Simulations with SeaWinds & AMSR footprints	80
6	Conclusions And Future Research Recommendations	105
6.1	Conclusion	105
6.2	Future Research Recommendations	107

List of Figures

2-1	Azimuthal Variation of NRCS - HH-Pol	8
2-2	Azimuthal Variation of NRCS - VV-Pol	9
2-3	Dependence of NRCS on incidence angle - VV-Pol	11
2-4	Dependence of NRCS on incidence angle - VV-Pol	12
2-5	Loci of possible vector winds associated with colocated noise-free σ^0 measurements	15
3-1	Contributions to Radiometric measurement	23
3-2	Scattering and extinction efficiency factors for a water sphere as a function of radius [Fraser, 1975]	30
3-3	Benoit's fit to the cloud absorption values [Benoit, 1968]	34
3-4	Frequency Dependence of empirical rainfall attenuation parameters	37
3-5	The mean droplet-size distribution of various cloud types [Mason, 1957]	40
3-6	Normalized Deirmendjian of top layer for the steady rain 3 mm/hr model (21-2)	43
3-7	Effect of scattering on apparent temperature measurement	45
3-8	Excess Apparent Temperature versus Total Atmospheric Attenua- tion at 10.69 GHz [Dome, 1980]	49
3-9	Excess Apparent Temperature versus Total Atmospheric Attenua- tion at 37 GHz [Dome 1980]	50

3-10 Attenuation vs. Excess Apparent Temperature at Different Frequencies	54
3-11 Temperature dependence of regression coefficient A1	56
3-12 Temperature dependence of regression coefficient A2	57
3-13 Temperature dependence of regression coefficient A3	58
5-1 Cubic relation between excess brightness temperature and attenuation	67
5-2 Probability Distribution of wind error. $T_{max} = 200$ K	74
5-3 Probability Distribution of wind error. $T_{max} = 150$ K	75
5-4 Probability Distribution of wind error. $T_{max} = 100$ K	76
5-5 Probability Distribution of wind error. $T_{max} = 200$ K	77
5-6 Probability Distribution of wind error. $T_{max} = 150$ K	78
5-7 Probability Distribution of wind error. $T_{max} = 100$ K	79
5-8 Geometry for Cases (i)	81
5-9 Geometry for Cases (ii)	82
5-10 Geometry for Cases (iii)	83
5-11 Typical brightness temperature assignment, $r_0 = 10$	85
5-12 Typical brightness temperature assignment, $r_0 = 10$	85
5-13 Typical brightness temperature assignment, $r_0 = 10$	86
5-14 Typical brightness temperature assignment, $r_0 = 10$	86
5-15 Typical brightness temperature assignment, $r_0 = 7.07$	87
5-16 Typical brightness temperature assignment, $r_0 = 7.07$	87
5-17 Typical brightness temperature assignment, $r_0 = 7.07$	88
5-18 Typical brightness temperature assignment, $r_0 = 4.47$	88
5-19 Typical brightness temperature assignment, $r_0 = 4.47$	89
5-20 Typical brightness temperature assignment, $r_0 = 4.47$	89
5-21 Probability distribution of wind error for Case I, $r_o = 10$	94
5-22 Probability distribution of wind error for Case I, $r_o = 7.07$	95

5-23	Probability distribution of wind error for Case I, $\tau_o = 4.47$	96
5-24	Probability distribution of wind error for Case II, $\tau_o = 10$	97
5-25	Probability distribution of wind error for Case II, $\tau_o = 7.07$	98
5-26	Probability distribution of wind error for Case II, $\tau_o = 4.47$	99
5-27	Probability distribution of wind error for Case III, $\tau_o = 10$	100
5-28	Probability distribution of wind error for Case III, $\tau_o = 7.07$. . .	101
5-29	Probability distribution of wind error for Case III, $\tau_o = 4.47$. . .	102
5-30	All radiometer cells with centers inside scatterometer cell	103
5-31	Wind error Distribution when all radiometer cells are used for cor- rection, $\tau_o = 10$	104

List of Tables

3.1	Porter's overcast models	38
3.2	Kreiss' cloud models	38
3.3	Valley's Rain Model	38
3.4	Properties of standard cloud models	42
4.1	SeaWinds Key Parameter Table	61
4.2	AMSR Main Performance Summary	62
5.1	Wind Estimate in m/s for a True Wind Speed = 20 m/s	72
5.2	Wind Estimate in m/s for a True Wind Speed = 10 m/s	72
5.3	Wind Estimate in m/s for a True Wind Speed = 5 m/s	73

Chapter 1

Introduction

1.1 Why Measure Wind Vector ?

Wind stress is the single largest source of momentum to the upper ocean. Winds drive oceanic motions on scales ranging from the surface waves to basin-wide current systems. Winds over ocean also modulate air-sea fluxes of heat, moisture, gases and particulates, thus regulating the crucial coupling between atmosphere and the ocean that establishes and maintains global and regional climate. Measurements of the surface wind velocity can be assimilated into regional and global numerical weather and wave models, thereby extending and improving our ability to predict future weather patterns and wave spectra on many scales [1].

1.2 Need for Satellite based Wind Vector Determination

Although measurements of ocean surface wind vector are of critical importance in many geophysical studies, data sets available currently are deficient in coverage and/or accuracy. Most ship borne measurements are geographically and phenomenologically biased (since for safety and economic reasons ships avoid active

storm regions). Ship reports of wind velocity are notoriously inaccurate owing to untrained observers, poor instrumentation, badly placed anemometers, contamination owing to ship motion, and data transcription and transmission errors [2]. While measurements from moored meteorological bouys are considered highly accurate they are few in number and are concentrated in coastal regions in the northern hemisphere. Only satellite-borne instruments can acquire wind data with global coverage, high spatial resolution and frequent sampling. Both satellite altimeters and multichannel radiometers can be used to estimate all-weather wind speed; however, these instruments do not measure wind direction, and thus cannot be used to calculate air-sea momentum fluxes (inherently vector quantities) nor directly to gain increased understanding of atmospheric dynamics.

Satellite borne scatterometers can acquire hundreds of times more observations of surface wind velocity each day than can ships and bouys. In addition, the accuracies of scatterometer measurements are nearly independent of conditions and location, and the measurements are globally distributed rather than being geographically and phenomenologically biased [3]. Scatterometers are the only remote sensing systems able to provide accurate, frequent, high resolution measurements of ocean surface wind speed and direction in both clear-sky and cloudy conditions.

1.3 Need for Integrated Scatterometer-Radiometer Systems

The first discussion of the advantage of combining joint radar and radiometer measurements was presented by Moore and Ulaby [4]. This concept was further developed and a satellite system was later proposed by Moore and Pierson [5] for worldwide ocean wind and wave predictions. Using a combined sensor system to

view the ocean allows estimates of the wind speed to be made by both sensors during clear sky conditions. The radiometer portion, however, is more severely affected by intervening atmosphere. When heavy wet cloud cover or precipitation is present, measurements by the radiometer may only consist of contributions from the intervening atmosphere. Use of a radiometer, therefore, allows regions of cloud cover and precipitation to be located. Furthermore, information from the radiometer can be used to estimate the attenuation seen by the radar, and thus, allow meaningful estimation of the wind speed even under these conditions. Here we investigate the effects of attenuation on scatterometer measurements. For this study we consider 18.7 GHz radiometer cells that are not uniformly filled with rain. A simple algorithm for correcting the errors in the scatterometer measurements using radiometer measurements is presented. An outline of this thesis is as follows.

Chapter 2 gives an overview of the principles of scatterometry. Chapter 3 deals with the concept of radiometry and the relationship between attenuation and excess brightness temperature. The SeaWinds scatterometer and the Advanced Microwave Scanning Radiometer (AMSR) systems are described briefly in Chapter 4. Chapter 5 outlines the simulation methodology used for correcting scatterometer measurements using a radiometer. Chapter 6 is a discussion of the simulation results and areas that need to be explored further for improving the wind error estimates.

Chapter 2

Scatterometry

2.1 Scatterometry

Any radar that measures the scattering or reflective properties of surfaces and/or volumes is called a scatterometer. The wind vector scatterometer is a radar specifically designed for backscatter measurements and it is calibrated so that accurate scattering measurements with it are possible. Scatterometers may be designed to measure at a particular angle, frequency, and polarization or over a range of one or more of these parameters.

Spaceborne scatterometers transmit microwave pulses to the ocean surface and measure the backscattered power received at the instrument. Since the atmospheric motions themselves do not substantially affect the radiation emitted and received by the radar, the scatterometers use an indirect technique to measure the wind vector over the ocean. Wind stress over the ocean generates waves which roughen the sea surface. Changes in the wind velocity cause changes in the surface roughness, which in turn modifies the radar cross section and hence the magnitude of backscattered power. Scatterometers measure this backscattered power, allowing estimation of the normalized radar cross section (σ^0) of the sea surface. To extract the wind velocity from these measurements, the relationship

between radar cross section and the near-surface winds must be known.

The radar cross section σ^o is calculated using the basic radar equation:

$$\sigma^o = \frac{(4\pi)^3 R^4 L P_r}{P_t G^2 \lambda^2 A} \quad (2.1)$$

where R is the slant range to the surface, P_t is the transmitted power, P_r is the received backscattered power, L represents known system losses, G is antenna gain, A is the effective area of illumination, and λ is the wavelength of the transmitted radiation.

From each illuminated location on the earth, the total received power is the sum of the backscattered power P_r and a contribution P_n resulting from instrument noise and the natural emissivity (at that frequency) from the earth-atmosphere system. To determine P_r accurately, the noise power P_n must be estimated and subtracted from the total received power $P_{(r+n)}$; the radar equation can then be used to calculate σ^o .

2.1.1 Components Of the Ocean

The backscattering at most angles of incidence is strongly related to the speed and direction of wind. For angles of incidence above 20 degrees the predominant mechanism is the Bragg scattering. The radar wavelengths normally used are resonant to the components of the ocean surface that are either the short gravity waves or the surface tension waves. For convenience, we use ripples to describe both the short gravity waves and the surface tension waves. These very short waves ride upon the larger ocean waves, but the resonant effect is so strong that capillary waves of the order of one millimeter high are dominant even when the underlying ocean waves are many meters high.

Waves on the ocean are very complex. If the wind starts to blow over a

calm sea, the first waves to form due frictional drag on the wind are the shortest ones. As these waves build up, non-linear interactions transfer energy to waves with larger amplitude and longer wavelengths. As wind continues to blow, longer and longer waves are generated until an equilibrium point is reached such that dissipation mechanisms balance the tendency for wave growth. The equilibrium point depends on the strength of the wind such that stronger winds generate longer and higher waves. The primary transfer of energy from the atmosphere to the sea is at the very shortest wavelengths. If the wind were to die out suddenly, the shortest waves would decay rapidly, whereas the longer waves would last long.

The waves so generated propagate away from their source, with longer waves attenuating more slowly than the shorter waves, and thus the longer waves can propagate to great distance, whereas the shorter waves are more localized. Because of this, the waves at any point on the surface are complex summations of the locally generated wind waves and the waves that have propagated in from other areas. As these waves come from different directions, their interaction makes the surface more complex than it would otherwise be.

The amplitude of the radar signal is dominated by the Bragg-resonant ripples and the local angle of incidence, so its average is governed by the local wind speed. Its distribution, however, depends on the slopes of the longer waves that determine the local angle of incidence.

2.2 Measurement of Radar Backscatter from the sea

Spaceborne scatterometers are the only proven method for global all-weather measurement of wind vectors at the ocean surface. Such measurements are critical inputs in the studies of oceanic circulation and air/sea interaction. The scatterometer does not directly measure the wind. Instead, it measures the normalized radar

backscatter of the ocean's surface which is related to the wind.

2.2.1 Azimuthal Variation of Radar Backscatter

The azimuthal variation of the radar backscatter from the sea at the midrange of angles of incidence is described by [6]:

$$\sigma^o = A + B\cos\phi + C\cos 2\phi \quad (2.2)$$

where ϕ is the horizontal angle between the radar look direction and the upwind direction. The coefficients A , B and C are functions of angle of incidence, wind speed, frequency and polarization. This variation is shown in the Figure 2-1 for horizontal polarization and in Figure 2-2 for vertical polarization [7]. The maximum signal occurs when the radar looks in the upwind direction, a somewhat smaller signal when the radar looks in the downwind direction, and a much smaller signal when the radar looks normal to the wind direction

The factors A , B and C may be related to the wind speed u by

$$A = a(\theta)u^{\gamma_a(\theta)} \quad (2.3)$$

$$B = b(\theta)u^{\gamma_b(\theta)} \quad (2.4)$$

$$C = c(\theta)u^{\gamma_c(\theta)} \quad (2.5)$$

Both the magnitude constants (a, b, c) and the wind-speed exponents ($\gamma_a, \gamma_b, \gamma_c$) are functions of the angle of incidence.

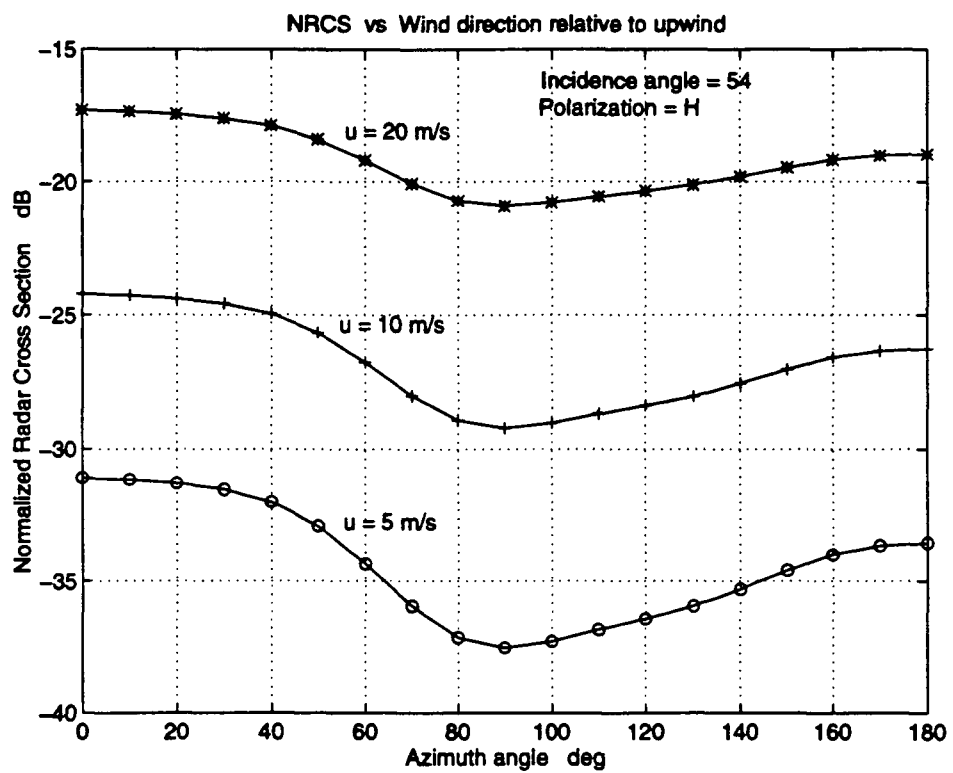


Figure 2-1: Azimuthal Variation of NRCS - HH-Pol

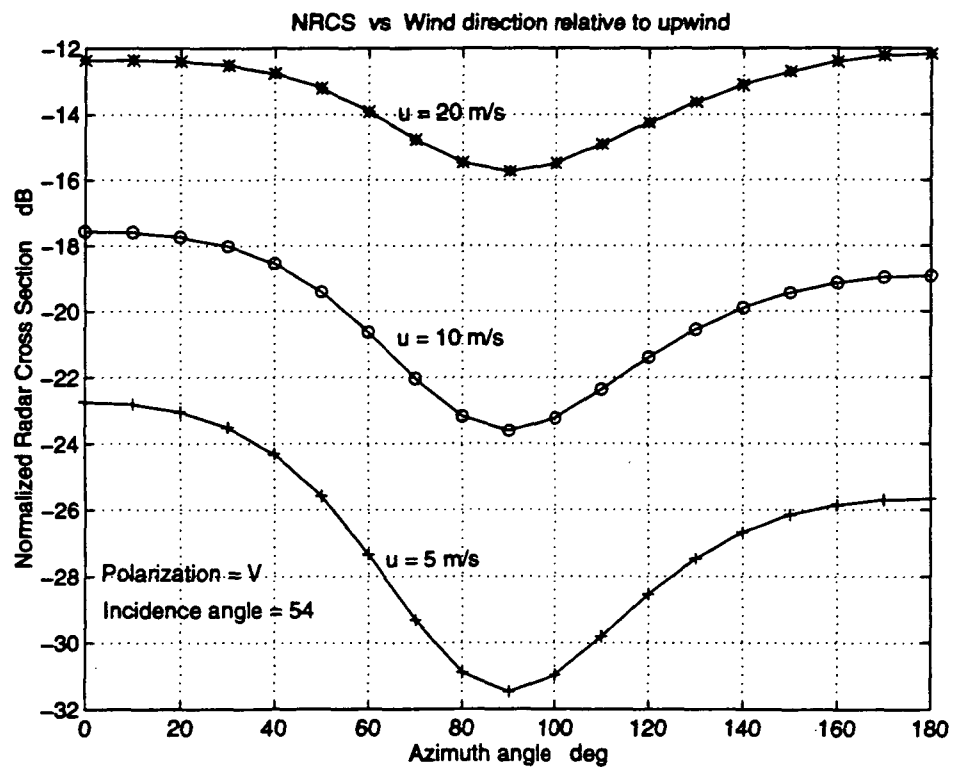


Figure 2-2: Azimuthal Variation of NRCS - VV-Pol

2.2.2 Dependence of backscatter on the angle of incidence

Near vertical incidence, the signals produced by the Bragg scattering are dominated by those produced by the geometric optic mechanisms. In this region the slopes are such that one can achieve specular reflection from facets on the surface of the sea, and many facets having narrow backscattering patterns are close enough to the specular condition that the signals returned by the quasi-specular mechanism are strong. At and near vertical incidence the strongest backscattering would occur from a perfectly flat surface or the one that was very gently undulating. As the surface gets rougher, more of the incident energy is scattered away from the radar receiver. Hence, radar backscattering decreases with increasing wind speed and wave height near vertical incidence, whereas it increases with increasing wind speed at angles beyond about 12 degrees. The variation of normalized radar cross section (σ^0) for two different incidence angles (47° and 54°) for V-polarization is shown in Figure 2-3 and that for H-polarization is shown in Figure 2-4 [7]. The surface wind speed assumed in these cases is 10 m/s.

2.2.3 Geophysical Model Function

The relationship between σ^0 and the near-surface wind vector is known as the "geophysical model function" and has been the subject of intense study over the last two decades. The model function should, in principle, be derivable from theory alone. However, such a task requires the complete understanding of both the relationship between the wind and the sea surface geometry, and the interaction between electromagnetic radiation and sea surface. Even though significant progress has been made in these area, the gaps in our knowledge are formidable.

Lacking rigorous theoretically based expressions, empirical models have been established to relate ocean radar cross section and the near-surface wind. With

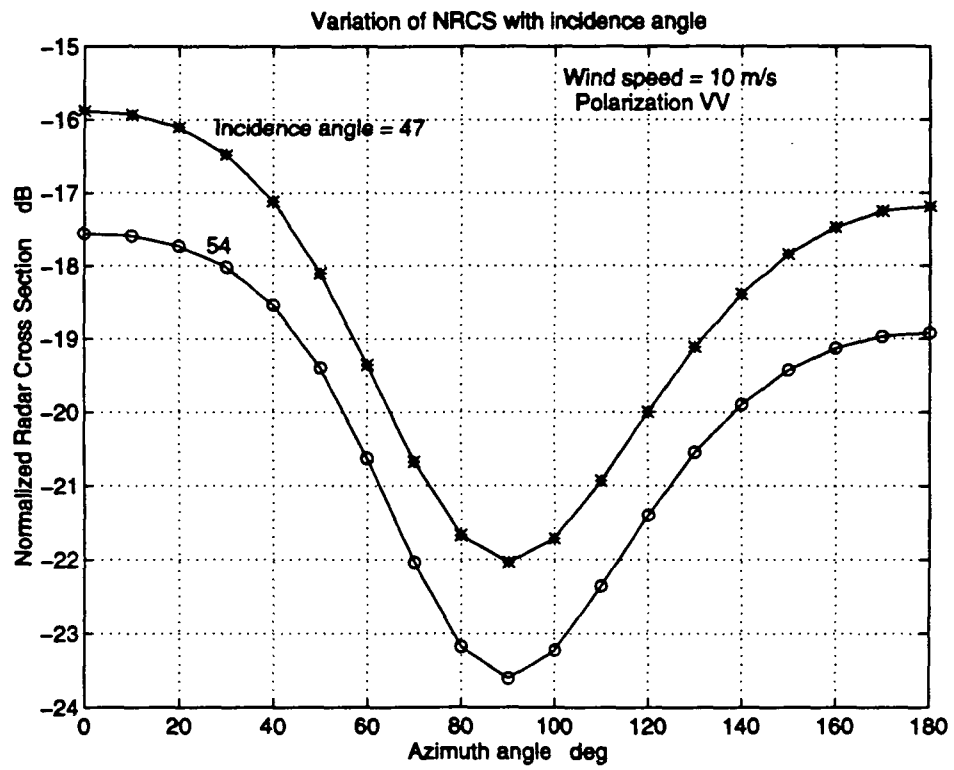


Figure 2-3: Dependence of NRCS on incidence angle - VV-Pol

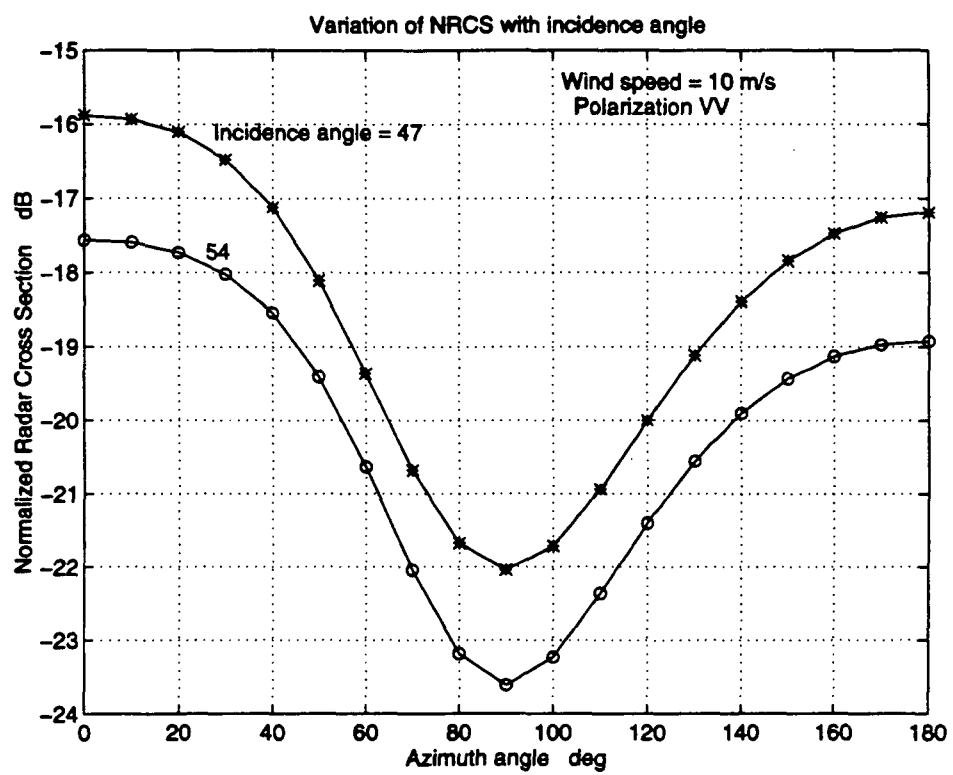


Figure 2-4: Dependence of NRCS on incidence angle - VV-Pol

the flight of the first spaceborne scatterometer on Seasat in 1978, several million calibrated σ° measurements became available for use in model function refinement studies, along with several thousand high quality *in situ* meteorological and oceanographic measurements spanning a range of atmospheric and oceanic conditions.

The geophysical model function can be written most generally as

$$\sigma^\circ = f(|U|, \phi, \dots, \theta, f, pol) \quad (2.6)$$

where $|U|$ is the wind speed, ϕ is the azimuthal angle between the incident radiation and the wind vector, ... represents the smaller effects of non-wind variables such as long waves, stratification, temperature, etc., θ is the incidence angle measured in the vertical plane, f and pol are the frequency and polarization respectively of the incident radiation.

2.2.4 The SASS model function

The SASS (SEASAT-A Satellite Scatterometer) model function [8], [9] is an empirical relationship between the ocean normalized radar cross section (σ°) of the ocean and the wind vector at a height of 19.5 m above the surface, assuming neutral stability. For the wind vector algorithm, the relationship is specified in the form of a table that gives two coefficients G and H in the equation [7]

$$\sigma^\circ(dB) = 10[G(\theta, \phi) + H(\theta, \phi)\log_{10}U] \quad (2.7)$$

or its equivalent in ratio form, with $G' = 10^{G(\theta, \phi)}$

$$\sigma^o = G'(\theta, \phi) U^{H(\theta, \phi)} \quad (2.8)$$

The G and H coefficients are tabulated separately for V and H polarizations every 2° in incidence and every 10° in azimuth. The tables relate backscatter to wind velocity, given the aspect and incidence angles.

2.2.5 Need for multiple measurements

Estimation of wind vector from a σ^o measurement involves inversion of the model function given by 2.8. However, for a single σ^o measurement, no unique solution exists; a single scalar measurement (such as σ^o) is insufficient to solve for both wind speed and wind direction as shown in Figure 2-5. The heavy solid line in the figure represents all possible vector winds (i.e., pairs of wind speed $|U|$ and wind direction ϕ) that are consistent with a single noise-free σ^o measurement. If a second measurement of σ^o is obtained from the same region of the sea surface but from an antenna oriented 90° with respect to the first, yield a second possible solution loci. Since each curve represents all possible $(|U|, \phi)$ values corresponding to the σ^o measurements, the solution consistent with both measurements must be one of the (up to 4) intersections.

2.2.6 Drawbacks of earlier scatterometer systems

The fourfold ambiguity in the wind direction resulting from σ^o measurements at only two angles severely detracted from the utility of the Seasat scatterometer data. Significant and time consuming ground-based processing using auxillary meteorological information was required to select the correct wind direction from the possible solutions. However, additional σ^o values obtained from antennas at yet other angles and/or using different polarizations yield additional possible so-

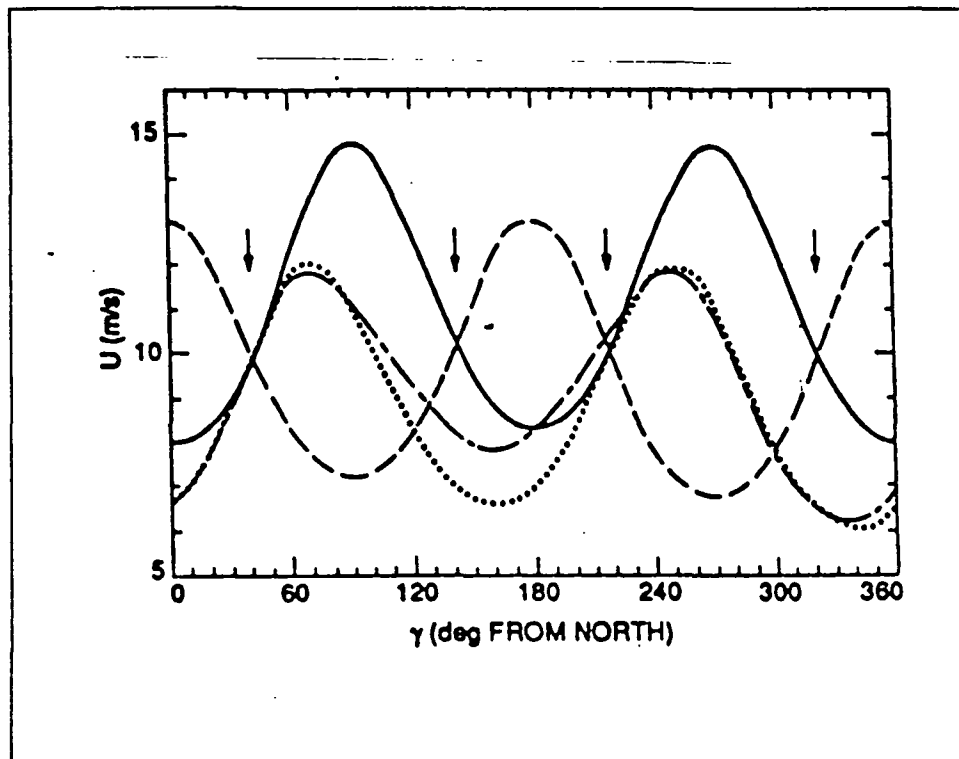


Figure 2-5: Loci of possible vector winds associated with colocated noise-free σ^o measurements

lution loci. In the case of noise-free measurements, the additional measurements allow a single intersection of all four curves to be identified [10], [11], [12], [13]. In practice, even with several σ° measurements, the model function inversion results in multiple solutions (corresponding to "near intersection" of all four curves) having nearly the same speed but different direction. These multiple solutions (historically known as "ambiguous vectors") result from a combination of instrumental noise, geophysical noise, and the small upwind-downwind asymmetry of the model function. The solution loci intersect at values of ϕ separated by 180° (corresponding to upwind-downwind asymmetry). While additional processing is still required to select a unique wind direction, the magnitude and complexity of the task are greatly reduced over that required for the fourfold case of SASS.

2.2.7 Requirements of scatterometer system

As discussed earlier, estimation of wind vector from scatterometers requires multiple co-located measurements of backscatter from different azimuth angles. In addition, to realize frequent global coverage, a wide observation swath must be imaged during each satellite orbit. The antenna concept dictates the swath width as well as the number and geometry (azimuth and incidence angles) of the σ° measurements.

Although the dual objective of multiple azimuth viewing and wide swath coverage can be met using multiple fan beam antennas or scanning spot beams, the Seasat SASS and NSCAT scatterometers rely on multiple fan beams. In early 1999, NASA will fly a new Ku-band scatterometer design, "SeaWinds" (SWS), as a part of the NASDA ADEOS-II mission [14]. The SWS instrument will provide crucial surface wind velocity measurements as a part of the NASA/international Earth Observing System (EOS). SeaWinds will be a departure from previous instruments, as it will be a dedicated conically scanning, dual pencil-beam scatterometer.

2.2.8 Advantages of scanning pencil-beam over fan-beam systems

The scanning pencil-beam design of SeaWinds has many advantages compared with traditional fan beam scatterometers [14]:

1. σ° measurement accuracy: The large pencil-beam antenna gain results in much higher signal-to-noise ratios than for fan-beam systems at the same incidence angle and transmit power.
2. Continuous swath: The incidence angle for σ° measurements is nominally constant for each beam, resulting in a continuous swath in which all σ° measurements are sensitive to wind. Fan-beam approaches have incidence angles that vary systematically across the swath; as σ° is insensitive to wind direction at small incidence angles, dual-swath fan-beam scatterometers have "nadir-gaps" of several hundred km between the swaths. The continuous SWS swath results in increased coverage and simplified processing.
3. Fixed incidence angles: The model function relating σ° to wind vector must be known only near the two incidence angles at which measurements are acquired, rather than the broad range of incidence angles required for fan-beam systems. By operating at relatively large incidence angles (47° and 54°), the wind velocity sensitivity of the instrument is improved.
4. Processor complexity and data rate: Fan-beam scatterometers require complicated on-board Doppler or range-gating schemes to achieve along-beam resolution and reduce data rate. The pencil-beam design requires neither a sophisticated on-board processor nor a high data rate.

Chapter 3

Evaluation of atmospheric attenuation using radiometer

3.1 Radiometry

Radiometry is a field of science and engineering related to the measurement of electromagnetic emission. The term "radiometry" means the measurement of incoherent radiant electromagnetic energy. A microwave radiometer can be used to estimate the total atmospheric attenuation experienced by a signal passing through the atmosphere. This passive instrument, which measures microwave emissions, is more sensitive to attenuation than an active-microwave sensor. Thus, the microwave radiometer can be used to provide an estimate of the total atmospheric attenuation to correct measurements by an active instrument, particularly a scatterometer, for atmospheric losses.

To measure the radar backscatter from the ocean with enough accuracy to allow determination of the wind vector, the effect of attenuation in the precipitating regions over the ocean must be considered. When condensed water is present in clouds and rain, the return signal is attenuated by the atmosphere and must be corrected before a wind determination can be made. The first discussion of the

advantage of combining joint radar and radiometric measurements was presented by Moore and Ulaby [4]. This concept was further developed and a satellite system was later proposed by Moore and Pierson [5] for worldwide ocean wind and wave predictions. Using a combined sensor system to view the ocean allows estimates of the wind speed to be made by both sensors during the clear sky conditions. The radiometer portion, however, is more severely affected by the intervening atmosphere. When heavy wet cloud cover or precipitation is present, measurements by the radiometer may only consist of contributions from the intervening atmosphere. Use of a radiometer, therefore, allows regions of cloud cover and precipitation to be located. Furthermore, information from the radiometer can be used to estimate the attenuation seen by the scatterometer, and thus, allow meaningful estimation of the wind speed even under these conditions.

3.1.1 Theoretical background

The bulk of the energy received by the earth is in the form of solar electromagnetic radiation. Part of the incident solar energy is scattered and absorbed by the earth's atmosphere, and the remainder is transmitted to the earth's surface. Of the latter, a part is scattered outward and the remainder is absorbed. The electromagnetic energy absorbed by a material medium is transformed into thermal energy, which is accompanied by a rise in the thermometric temperature of the material. The reverse process, that of thermal emission, serves to create a balance between absorbed solar radiation and the radiation emitted by the earth's surface and its atmosphere. The theory of radiative transfer explains the transformation process.

The apparent temperature of a material is the temperature of an equivalent blackbody which radiates the same power. Since a blackbody at some temperature always radiates more power than any other material at the same temperature, the apparent temperature of any material is always less than its physical temperature. It is this naturally occurring quantity, apparent temperature, that a radiometer

measures. The radiative transfer equation relates apparent temperature to radiation from the ground, the atmosphere, and the cosmos. Stogryn [15] developed a form of this equation for the case of a downward looking radiometer. He assumed uniform horizontally stratified atmosphere. If scattering is negligible, a simplified version of the transfer equation, also developed by Stogryn, may be used. The individual contributions to the apparent temperature are readily recognized in this form of the equation. If the effects of scattering are significant, the scattering contributes to the apparent temperature in the radiative transfer equation.

3.1.2 Radiative transfer equation

For the case of a downward-looking microwave radiometer, the total radiation measured is called the apparent temperature, and consists of contributions from both the surface and the intervening atmosphere.

$$\cos\theta \frac{dT_{aj}(z, \theta, \phi)}{dz} + [\alpha(z) + \beta_{sc}(z)]T_{aj}(z, \theta, \phi) = \alpha(z)T_{air}(z) + \beta_{sc}(z) \int_0^{2\pi} \int_0^\pi \gamma(\cos < H >) T_{aj}(z, \theta_s, \phi_s) \sin(\theta_s) d\theta_s d\phi_s \quad (3.1)$$

where

$T_{aj}(z, \theta, \phi)$ = apparent temperature with j polarization at an altitude z and in the direction θ and ϕ

$\alpha(z)$ = total absorption coefficient of atmosphere per unit path length

$\beta_{sc}(z)$ = scattering coefficient of precipitation per unit path length

$\gamma(\cos < H >)$ = scattering phase function of precipitation per unit solid angle

θ and ϕ = observing angles

θ_s, ϕ_s scattering angles

$\alpha(z)T_{air}(z)$ is contribution due to thermal radiation from the atmosphere, while the integral term is the contribution due to particle scattering of the incident

radiation from all directions into the direction of interest.

3.1.3 Radiative transfer - Neglecting Scattering

If the effects of scattering in the atmosphere are negligible, the radiative transfer equation reduces to

$$\cos\theta \frac{dT_{aj}(z, \theta, \phi)}{dz} + \alpha(z)T_{aj}(z, \theta, \phi) = \alpha(z)T_{air}(z) \quad (3.2)$$

Assuming no ϕ variation, Stogryn (1967) determined that the solution takes the following form:

$$T_{aj}(z, \theta) = L(z, \theta)(T_{aj}(0, \theta) + T_{atm}(z, \theta)) \quad (3.3)$$

where

$T_{aj}(z, \theta)$ = apparent temperature at the altitude z , and the nadir angle θ

$L(z, \theta) = \exp[-\sec\theta \int_0^z \alpha(u)du]$ = Transmittance

$T_{atm}(z, \theta) = \sec\theta \int_0^z T_{air}(z')\alpha(z')\exp[-\sec\theta \int_{z'}^z \alpha(u)du] =$ atmospheric temperature

$T_{air}(z)$ = thermometric temperature profile of the air

The apparent temperature at the surface is not affected by any atmospheric losses. The transmittance is unity, and the atmospheric temperature is zero. Hence $T_{aj}(0, \theta)$ is simply the sum of the surface emission and the reflected sky

temperature.

$$T_{aj}(0, \theta) = \epsilon(\theta)T_g + T_{rj}(\theta) \quad (3.4)$$

where

$\epsilon(\theta)$ = surface emissivity in the direction of θ

T_g = surface thermometric temperature in kelvin

$T_{rj}(\theta)$ = reflected sky temperature at the surface

$$T_{rj}(\theta) = \frac{1}{4\pi} \int_0^{2\pi} \int_0^{\pi/2} \gamma_j(\theta, \theta_s, \phi_s) T_{SKY}(\theta_s) \sin \theta_s d\theta_s d\phi_s \quad (3.5)$$

$\gamma_j(\theta, \theta_s, \phi_s)$ = polarized differential scattering coefficient of the surface

$T_{SKY}(\theta_s)$ = total sky temperature at the surface

$$T_{SKY}(\theta_s) = \sec \theta_s \int_0^\infty T_{air}(z') \alpha(z') \exp[-\sec \theta_s \int_0^{z'} \alpha(u) du] dz' \quad (3.6)$$

ignoring the small term for radiation from space.

$$T_{aj}(z, \theta) = L(z, \theta) [\epsilon_j(\theta)T_g + T_{rj}(\theta)] + T_{atm}(z, \theta) \quad (3.7)$$

Figure 3-1 shows how several contributions add up, leading to the equation

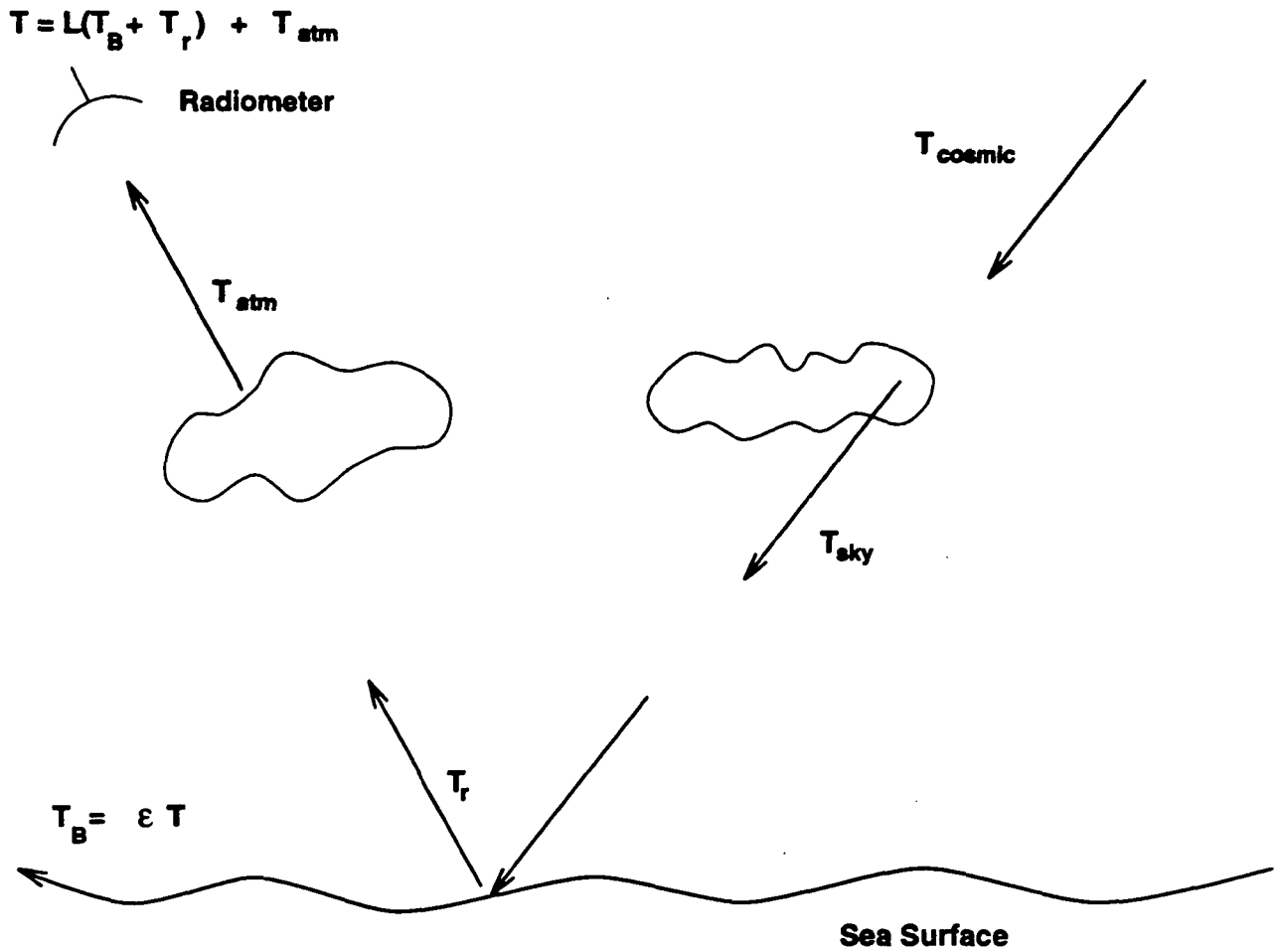


Figure 3-1: Contributions to Radiometric measurement

3.7. The reflected sky temperature and ground emission must pass through the atmosphere to the observation height z .

3.1.4 Absorption Models

Absorption of energy by the Earth's atmosphere arises from several sources. In clear sky conditions, absorption at microwave frequencies occurs due to water vapor and molecular oxygen. Under cloudy conditions, additional absorption arises from the liquid water content of the clouds. When precipitation occurs, the total absorption is further increased. Consequently, the total absorption, $\alpha(z)$, may

be expressed as

$$\alpha(z) = \alpha_{cs}(z) + \alpha_{cd}(z) + \alpha_{rain}(z) \quad (3.8)$$

where

α_{cs} = clear sky absorption coefficient

α_{cd} = cloud absorption coefficient

α_{rain} = rain absorption coefficient

If rain is present, the rain absorption coefficient will predominate. If only clouds are present, the cloud absorption coefficient will predominate. If neither rain nor clouds are present, then $\alpha(z)$ is caused by clear sky absorption only. Extinction coefficient of rain at 18 GHz for a rain rate of 10 mm hr^{-1} is approximately 1 db km^{-1} . The cloud extinction coefficient at 18 GHz for a cloud with liquid water content $m_v = 0.3 \text{ gm}^{-3}$ is approximately 0.1 db km^{-1} [16]. The above values show that rain dominates if it is present.

3.1.5 Effect of Scattering

When a particle is present in the atmosphere, power is absorbed by the particle and an additional fraction is scattered in all directions. The behavior of the electromagnetic waves in the presence of such particles is characterized by the absorption and scattering of the electromagnetic energy [17]. If S_i is the power density (Wm^{-2}) incident upon a particle of geometrical cross-section area A , the ratio of the power absorbed P_a to the incident power density S_i is defined as the absorption cross-section, Q_a :

$$Q_a = \frac{P_a}{S_i} \quad m^2 \quad (3.9)$$

The ratio of Q_a to the physical cross-section A is known as the absorption efficiency factor, ϵ_a . For a spherical particle of radius r , $A = \pi r^2$ resulting in

$$\epsilon_a = \frac{Q_a}{\pi r^2} \quad (3.10)$$

Consider an incident plane wave traveling in the z -direction, with $S_s(\theta, \phi)$ is the power density of the radiation scattered in the direction (θ, ϕ) at a distance R from the particle. The total power scattered by the particle is the integral of $S_s(\theta, \phi)$ over the spherical surface of radius R centered on the particle:

$$P_s = \int_{4\pi} S_s(\theta, \phi) R^2 d\Omega \quad (3.11)$$

Similar to the absorption cross-section, the scattering cross-section, Q_s , and scattering efficiency factor ϵ_s , are defined as

$$Q_s = \frac{P_s}{S_i} \quad m^2 \quad (3.12)$$

$$\epsilon_s = \frac{Q_s}{\pi r^2} \quad (3.13)$$

The extinction (or attenuation) cross-section, Q_e , is defined as the ratio of total power removed from the incident electromagnetic wave to the area, and is

the sum of the absorption and scattering cross-sections:

$$Q_e = Q_a + Q_s \quad m^2 \quad (3.14)$$

The extinction efficiency factor is

$$\epsilon_e = \epsilon_a + \epsilon_s \quad (3.15)$$

The radar backscattering cross-section, σ_b , is defined as the power density scattered in the backwards direction towards the radiation source, $S_s(\theta = \pi)$, such that σ_b multiplied by the incident power density would be equal to the total power radiated by an equivalent isotropic radiator. At a distance R from the scatterer, $S_s(\theta = \pi)$ is given by

$$S_s(\theta = \pi) = \frac{S_i \sigma_b}{4\pi R^2} \quad Wm^{-2} \quad (3.16)$$

Solving for the radar backscattering cross-section,

$$\sigma_b = 4\pi R^2 \frac{S_s(\theta = \pi)}{S_i} \quad m^2 \quad (3.17)$$

3.1.6 Mie scattering

The calculation of the absorption, scattering, and backscattering cross-sections for an arbitrary shape is very difficult. However, the solution for a dielectric sphere of radius r was derived by Mie [18]. The results are given in the form of a converging series:

$$\epsilon_s(n, \chi) = \frac{2}{\chi^2} \sum_l^{\infty} (2l+1)(|a_l|^2 + |b_l|^2) \quad (3.18)$$

$$\epsilon_e(n, \chi) = \frac{2}{\chi^2} \sum_l^{\infty} (2l+1) \operatorname{Re}\{a_l + b_l\} \quad (3.19)$$

$$\epsilon_b(n, \chi) = \frac{1}{\chi^2} \sum_l^{\infty} |(-1)^l (2l+1)(a_l - b_l)^2| \quad (3.20)$$

with χ defined as

$$\chi = k_b r = \frac{2\pi r}{\lambda_b} = \frac{2\pi r}{\lambda_o} \sqrt{\epsilon_{rb}} \quad (3.21)$$

and n as

$$n = \frac{n_p}{n_b} = \sqrt{\frac{\epsilon_{cp}}{\epsilon_{cb}}} \equiv \sqrt{\epsilon_c} \quad (3.22)$$

where: a_l and b_l are known as the Mie coefficients,
 k_b = the wave number in the background medium,
 ϵ'_{rb} = the real part of the relative dielectric constant of the background medium,
 λ_b = the wavelength in the background medium,
 λ_o = the free-space wavelength,
 n_p = complex index of refraction of the particle material,
 n_b = complex index of refraction of the background medium,
 ϵ_{cp} = complex dielectric constant of the particle material,

ϵ_{cb} = complex dielectric constant of the background medium,

ϵ_c = complex dielectric constant of the particle relative to the background medium.

When the background medium is air, as is true in the atmosphere, then $\epsilon'_{rb} \approx 1$, $n_b \approx 1$, and $\lambda_b \approx \lambda_o$. The equations for the Mie coefficients are not repeated here but can be obtained from several references [18], [17].

3.1.7 Rayleigh-approximation for scattering

When the particle size is much smaller than the wavelength of the incident wave, such that $|n\chi| \ll 0.5$ is satisfied, the Mie expression for ϵ_s and ϵ_e may be expressed by only the first two terms of the Mie series. It then takes the form

$$\epsilon_s = \frac{8}{3}\chi^4|K|^2 \quad (3.23)$$

and

$$\epsilon_e = 4\chi \text{Im}(-K) + \frac{8}{3}\chi^4|K|^2 \quad (3.24)$$

where

$$K = \frac{n^2 - 1}{n^2 + 2} = \frac{\epsilon_c - 1}{\epsilon_c + 2} \quad (3.25)$$

Here $\epsilon_c = n^2$ is the complex dielectric constant of the droplet relative to the background medium. The absorption efficiency is obtained as

$$\epsilon_a = \epsilon_e - \epsilon_s = 4\chi \text{Im}\{-K\} \quad (3.26)$$

The corresponding scattering and absorption cross-sections for a single spherical scatterer can now be determined. To determine the cross-sections for a spherical particle of radius r at a given wavelength, only the values for $|K|^2$ and $\text{Im}(-K)$ are required. For water, the value of $|K|^2$ is approximately equal to 0.9 for frequencies between 3 GHz and 30 GHz and temperatures from 0° C to 20° C, while $\text{Im}(-K)$ increases with increasing frequency and decreasing temperature [17].

Since the Rayleigh approximation only applies when the particle diameters are small compared to the incident wavelength this implies $|n\chi| < 0.5$. The Mie and Rayleigh approximations for the extinction and scatter efficiency factors, ϵ_s , and ϵ_e of water clouds [19] are shown in Figure 3-2

Ice clouds may contain particles with radii up to about 10 mm, but due to the smaller refractive index, the Rayleigh criterion is applicable up to about 70 GHz for ϵ_e , and up to 200 GHz for ϵ_s [17].

3.1.8 Volume scattering

In a cloud resolution volume, the scatterers (water or ice particles) are randomly distributed within the volume, so there are no coherent phase relationships between the fields scattered by the individual particles. This assumption allows the use of non-coherent scattering theory when computing the average absorption and backscattering within the volume. Additionally, the concentration of particles is usually small enough to support the assumption that shadowing effects can be ignored.

The volume scattering coefficient, k_s , is the total scattering cross-section per unit volume, and its units are $(N\text{pm}^{-3}) \times \text{m}^2 = N\text{pm}^{-1}$. The volume scattering

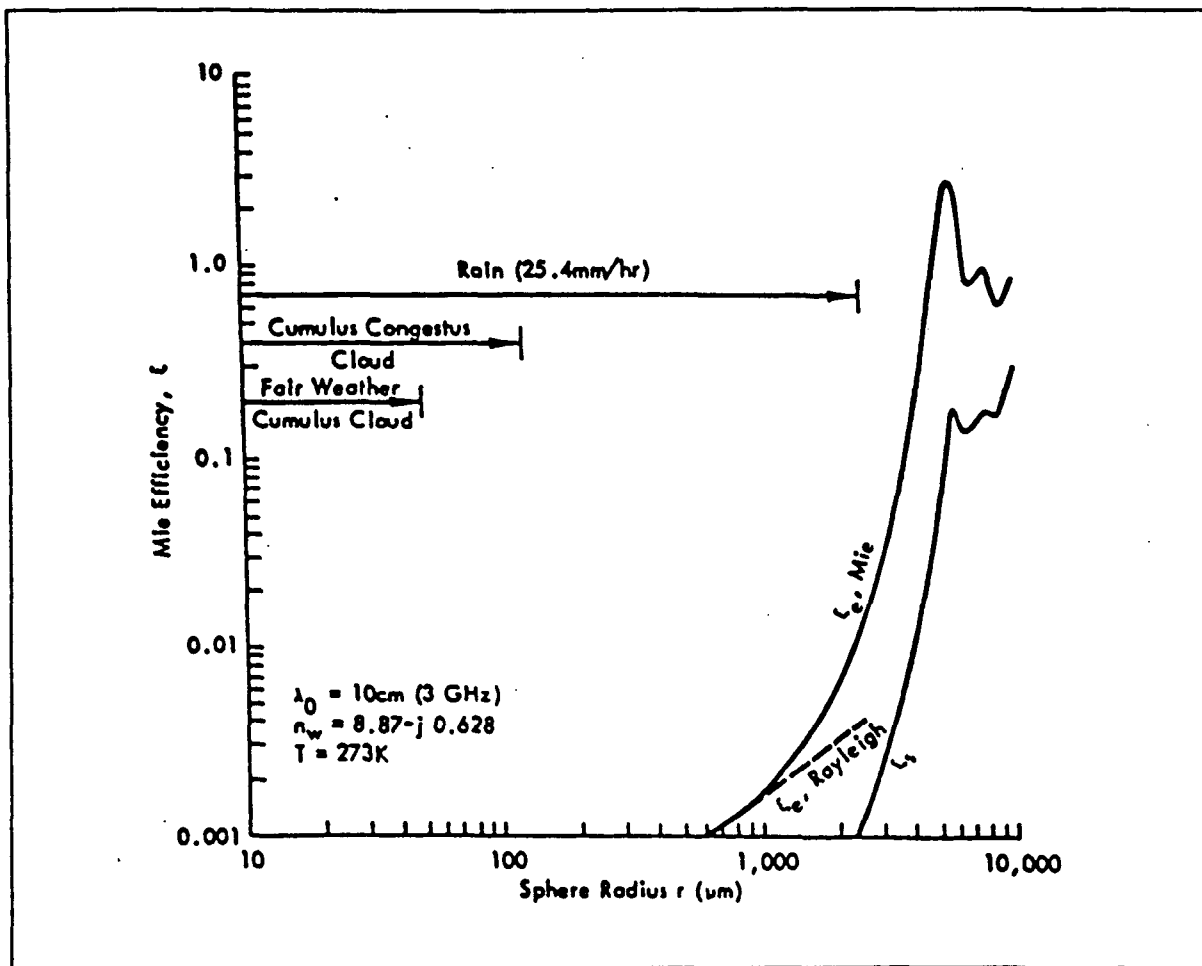


Figure 3-2: Scattering and extinction efficiency factors for a water sphere as a function of radius [Fraser, 1975]

coefficient is defined by

$$k_s = \int_{r_{min}}^{r_{max}} p(r) Q_s dr \quad Npm^{-1} \quad (3.27)$$

where $p(r)$ represents the drop-size distribution (number of drops per m^3 per unit increment of r), Q_s is the scattering cross-section of sphere with radius r , and r_{max} and r_{min} are the upper and lower limits of the drop radii contained in the cloud. If the Rayleigh criterion is satisfied, the volume scattering coefficient reduces to

$$k_s = \frac{2\pi^5}{\lambda^4} |K|^2 \sum_{i=1}^N D_i^6 \quad Npm^{-1} \quad (3.28)$$

where N is the total number of droplets per unit volume of the cloud and D_i is the diameter of the i th droplet per unit volume.

Similarly the volume absorption coefficient can be determined by

$$k_a = \int_{r_{min}}^{r_{max}} p(r) Q_a dr \quad Npm^{-1} \quad (3.29)$$

this equation can be represented as

$$k_a = \frac{\pi^2}{\lambda} Im(-K) \sum_{i=1}^N D_i^3 \quad Npm^{-1} \quad (3.30)$$

The volume extinction coefficient can be obtained as

$$k_e = k_a + k_s \quad Npm^{-1} \quad (3.31)$$

It can be seen that, for smaller droplet radii, the value of the absorption cross-section dominates in determining the extinction cross-section. This is due to the D^6 scattering-coefficient dependence as compared with D^3 absorption-coefficient dependence in the Rayleigh region. Since the cloud volume-extinction coefficient k_e is the sum of the volume absorption coefficient and the volume scattering coefficient, it is approximately equal to the volume absorption coefficient for small droplet radii.

As with the scattering and absorption volume coefficients, a similar definition is used for the volume backscatter coefficient, σ_b , that of a summation (or integral) of backscattering cross-sections of the individual drops in a unit volume.

$$\sigma_v = \int_{r_{\min}}^{r_{\max}} p(r) \sigma_b dr \quad m^{-1} \quad (3.32)$$

which after suitable substitutions gives

$$\sigma_v = \frac{\pi^5}{\lambda^4} |K|^2 \sum_{i=1}^N D_i^6 \quad m^{-1} \quad (3.33)$$

In terms of reflectivity factor (Z), σ_v can be expressed as

$$\sigma_v = \frac{\pi^5}{\lambda^4} |K|^2 Z 10^{-18} \quad m^{-1} \quad (3.34)$$

where Z is the reflectivity factor and is the summation of all the droplet diameters per unit volume. The 10^{-18} factor allows for Z to be expressed in units of $mm^6 m^{-3}$, commonly used in the meteorology community.

3.2 Cloud Models

Ryde and Ryde [20] were the first to develop theoretical expressions for cloud and rain absorption coefficients using Mie's scattering theory [18]. Gunn and East [21] summarized Ryde's work. They divided clouds into two types, according to composition:

- Water clouds
- Ice clouds

Since the dielectric constant of water is very different from that of ice, absorption coefficients for each category of cloud were computed separately.

The cloud absorption coefficient values calculated by Gunn and East as a function of frequency and temperature, for both water and ice clouds, are shown in Figure 3-3.

The lines in Figure 3-3 are the Benoit [22] fits to the data of Gunn and East. Interpolating with respect to temperature, as well as frequency, Benoit developed the expression for cloud absorption coefficient

$$\alpha_{cd}(z) = M f^b \exp(a) \quad (3.35)$$

where

M = liquid water content of clouds, gm/m^3

f = propagation frequency in GHz

b = frequency index

$b_w = 1.95$ for water clouds

$b_i = 1.006$ for ice clouds

a = temperature coefficient

$a_w = -6.866[1 + 0.0045(T_{air}(z) - 273)]$

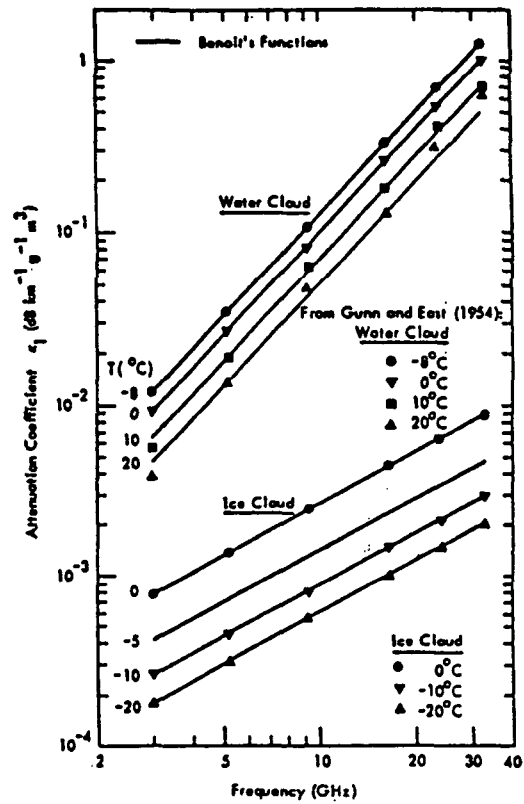


Figure 3-3: Benoit's fit to the cloud absorption values [Benoit, 1968]

$$a_i = -8.26[1 - 1.767 \times 10^{-2}(T_{\text{air}}(z) - 273) - 4.374 \times 10^{-4}(T_{\text{air}}(z) - 273)^2]$$

3.2.1 Rain absorption coefficient

Ryde and Ryde also developed theoretical expressions for rain absorption coefficients. Gunn and East [21] derived an empirical expression for rain absorption of the form:

$$\alpha_{\text{rain}}(z) = k[R(z)]^p \quad (3.36)$$

where

$R(z)$ = rainfall rate at height z in mm/hr

k, p = frequency dependent constants

Medhurst [23] used attenuation measurements taken between 1946 and 1962 to update the values of the parameter k for an assumed value of p equal to one, originally calculated by Ryde and Ryde. Medhurst also compared the rain absorption coefficients computed using the new parameter values with theoretical maximum and minimum rain attenuations. The absorption values were greater than the theoretical maximum. Medhurst concluded that the theoretical calculations were slightly deficient.

de Bettencourt [24], like Medhurst, summarized the results of attenuation experiments up to 1972, including the ones cited by Medhurst. de Bettencourt also computed values for the empirical parameters k and p . His results are presented in Figure 3-4. Medhurst's curves are also presented for comparison. Medhurst's model was too simple to permit a good fit for rain attenuation data. This is mainly due to the fact that Medhurst's model assumed p to be always equal to

one. de Bettencourt's model is valid over a wider range of frequencies because he used results from more experiments.

3.2.2 Porter and Kreiss cloud models

Models developed by Porter [25] classify cloudy skies as

- Light
- Medium
- Heavy overcast

The heights of cloud tops and bottoms, as well as liquid water content are modeled for each type of cloud. Porter's models are presented in Table 3.1. Kreiss [26] modeled

- stratus clouds
- thick stratus clouds
- tall cumulus clouds

His results are presented in Table 3.2. Kreiss models represent thicker clouds which cause greater attenuation.

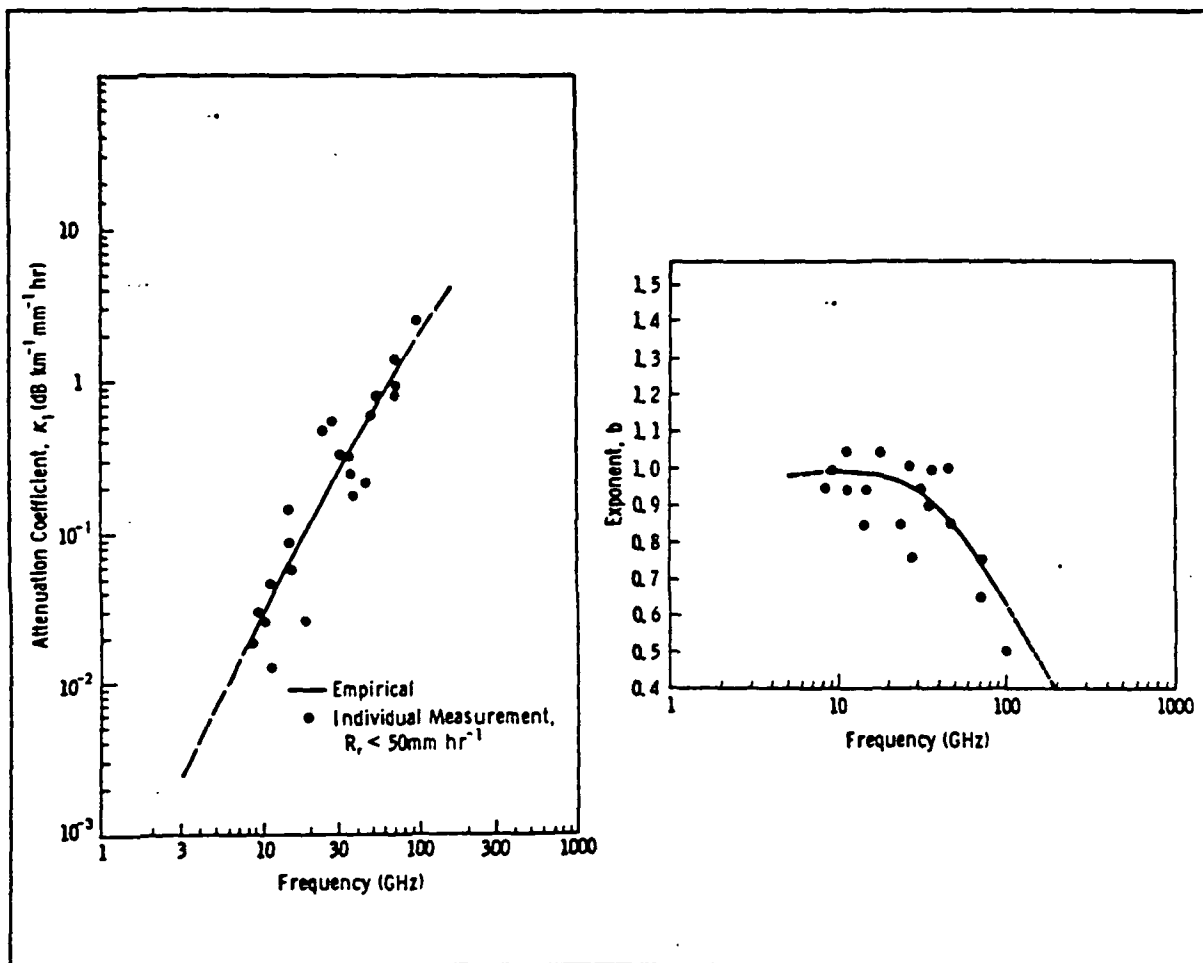


Figure 3-4: Frequency Dependence of empirical rainfall attenuation parameters

Table 3.1: Porter's overcast models

Classification	Altitude Extent (m)	Water Content (gm/m ³)
Light (Sun visible)	300-650	0.33
Medium (Light sky)	400-900	0.67
Heavy	500-3200	1.00

Table 3.2: Kreiss' cloud models

Cloud Type	Altitude Extent (m)	Water Content (gm/m ³)
Stratus	630-1457	0.5, 0.25, 0.15
Stratus	630-1949	0.5, 0.25, 0.15
Thick Stratus	628-3012	4.0, 2.0, 1.0
Tall Cumulus	628-7185	4.0, 1.0, 0.5

3.2.3 Valley Rain Model

Valley's [27] sets of rain models were developed with rain rate measurements over land. Valley's models are used over ocean assuming that the characteristics of precipitation are roughly the same over the land and over ocean. A set of models typical of summer rain in temperate zones and of tropical rains in any season is shown in Table 3.3.

Table 3.3: Valley's Rain Model

Updraft Condition (m/sec)	Rain Parameters		Cloud Parameters	
	Altitude Extent (m)	Precipitation at $z = 0$ (mm/hr)	Altitude Extent (m)	Water Content (gm/m ³)
0.4	0-3100	10.3	3100-7000	0.30
0.3	0-3200	7.9	3200-7000	0.25
0.2	0-3300	5.2	3300-7000	0.15
0.1	0-3500	2.8	3500-7000	0.10

3.3 Deirmendjian Models

3.3.1 Cloud Models

To get an accurate estimate of absorption and scattering coefficients and to generate values for backscatter coefficient, knowledge of either the drop-size distribution or the reflectivity factor is required. All the parameters in the SNR calculation with the exception of drop-size distribution $p(r)$ and Z are easy to measure or model. Many researchers have put considerable effort to accurately model these parameters. The measured drop-size distribution for several cloud types [28] is illustrated in Figure 3-5

The distribution shows a sharp rise in concentration for low values of droplet radii followed by a gradual decrease for the larger drop sizes. This is true for most water clouds. Xin reviewed several distribution models, including the log normal, modified gamma distribution and the Khirgian-Mazin distributions [29]. Propp studied a generalized case of the Khirgian-Mazin distribution developed by Deirmendjian [30]. The Deirmendjian model has the form given by

$$n(r) = Ar^{C_1} \exp(-Br^{C_2}) \quad \mu m^{-4} \quad (3.37)$$

where

$$A = \frac{m_v C_2 B^{[\frac{C_1+4}{C_2}]}}{\frac{4}{3}\pi \times 10^6 \Gamma[\frac{C_1+4}{C_2}]}$$
$$B = \frac{C_1}{C_2 r_c^{C_2}}$$

Γ = gamma function,

m_v = mass density of the cloud, gm^{-3} ,

r_c = mode radius, μm ,

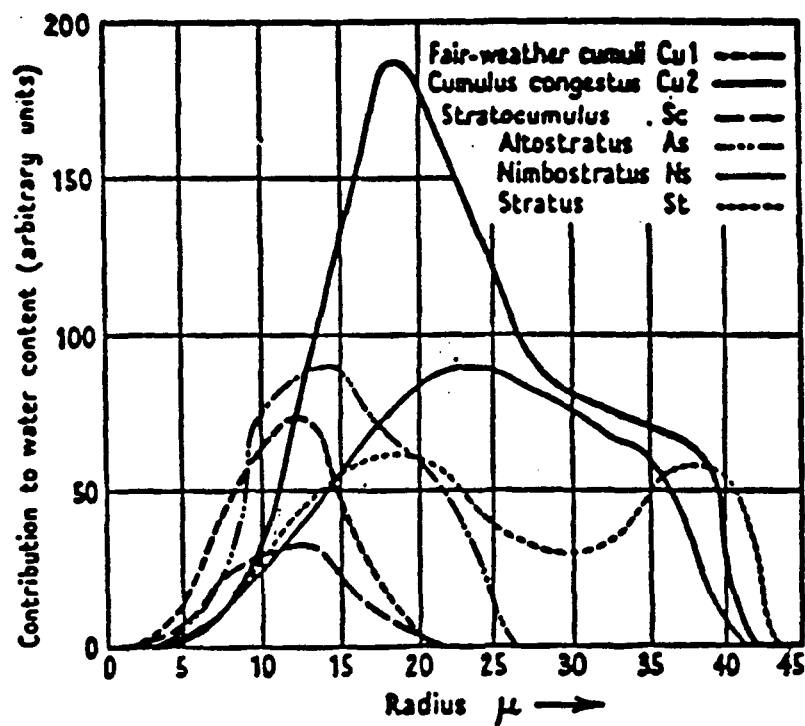


Figure 3-5: The mean droplet-size distribution of various cloud types [Mason, 1957]

C_1 and C_2 = *shape parameters*.

This distribution is based on a modified gamma function which reduces to the gamma function when $C_2 = 1$. Values for r_c , C_1 and C_2 given by Deirmendjian for 10 cloud types [31] and later expanded to include 19 various cloud types by Reifenstein and Gaut [32]. Table 3.4 summarizes these parameters [33]. In this table I, W and R stand for Ice, Water and Rain respectively indicating that these are the principle components of that cloud type.

The Deirmendjian model supports several cloud types, each having one or more horizontal layer(s) for which composition (water, ice or rain), mass density, mode radius, two shape parameters, and altitude limits are specified. The maximum concentration occurs at the mode radius, and the two shape parameters control the shape of the distribution's rising and falling edges. The ability to model different types of clouds at various altitudes is the major advantage of the Deirmendjian model. The comparison of a sample Deirmendjian distribution shown in Figure 3-6 with the data shown in Figure 3-5 reveals a good correlation between the shapes of the Deirmendjian model and the measured data.

Table 3.4: Properties of standard cloud models

Cloud Model	Cloud Name	Cloud Base	Cloud Top	m_w	r_c	C_1	C_2	Prin. Comp.
1-A-1	Cirrostratus	4000	6000	0.1	40	6	0.5	I
1-M-1	Cirrostratus	5000	7000	0.1	40	6	0.5	I
1-T-1	Cirrostratus	6000	8000	0.1	40	6	0.5	I
10-1	Alto cumulus	2400	2900	0.15	10	6	0.5	W
14-1	Alto cumulus	2400	2900	0.15	10	6	1	W
20-1	Low-Lying Stratus	150	650	0.25	10	6	1	W
20-2	Low-Lying Stratus	500	1000	0.25	10	6	1	W
21-1C	Drizzle, 0.2 mm/hr	1000	1500	1	10	6	0.5	W
21-1B		500	1000	2	10	6	0.5	W
21-1A		0	500	1	20	6	0.5	R
21-2D	Steady Rain, 3mm/hr	1000	1500	1	10	6	0.5	W
21-2C		500	1000	2	10	6	0.5	W
21-2B		150	500	1	10	6	0.5	W
21-2A		0	150	0.2	200	5	0.5	R
21-3D	Steady Rain, 15mm/hr	2000	4000	2	10	6	0.5	W
21-3C		1000	2000	3	10	6	0.5	W
21-3B		300	1000	2	10	6	0.5	W
21-3A		0	300	1	200	5	0.5	R
22-1	Stratocumulus	330	660	0.25	10	6	0.5	W
22-2	Stratocumulus	660	1320	0.25	10	6	0.5	W
25-1C	Fair Weather Cumulus	1500	2000	0.5	10	6	0.5	W
25-1B		1000	1500	1	10	6	0.5	W
25-1A		500	1000	0.5	10	6	0.5	W
25-2C	Cumulus, 2.4 mm/hr	1000	3000	2	20	6	0.2	W
25-2B		500	1000	1	20	6	0.2	W
25-2A		0	500	0.1	400	5	0.5	R
25-3C	Cumulus, 12 mm/hr	1000	4000	4	10	6	0.2	W
25-3B		400	1000	2	20	6	0.2	W
25-3A		0	400	0.5	400	5	0.5	R
25-4E	Cumulus Congestus	2500	3000	0.5	20	5	0.3	W
25-4D		2000	2500	1	20	5	0.3	W
25-4C		1600	2000	0.8	20	5	0.3	W
25-4B		1200	1600	0.5	15	5	0.4	W
25-4A		1000	1200	0.3	10	6	0.5	W
26-1F	Cumulonimbus, 150 mm/hr	8000	10000	0.2	40	6	0.5	I
26-1E		6000	8000	3	10	6	0.2	W
26-1D		4000	6000	4	10	6	0.2	W
26-1C		421000	4000	8	10	6	0.2	W
26-1B		300	1000	7	20	6	0.2	W
26-1A		0	300	6.3	400	5	0.2	R

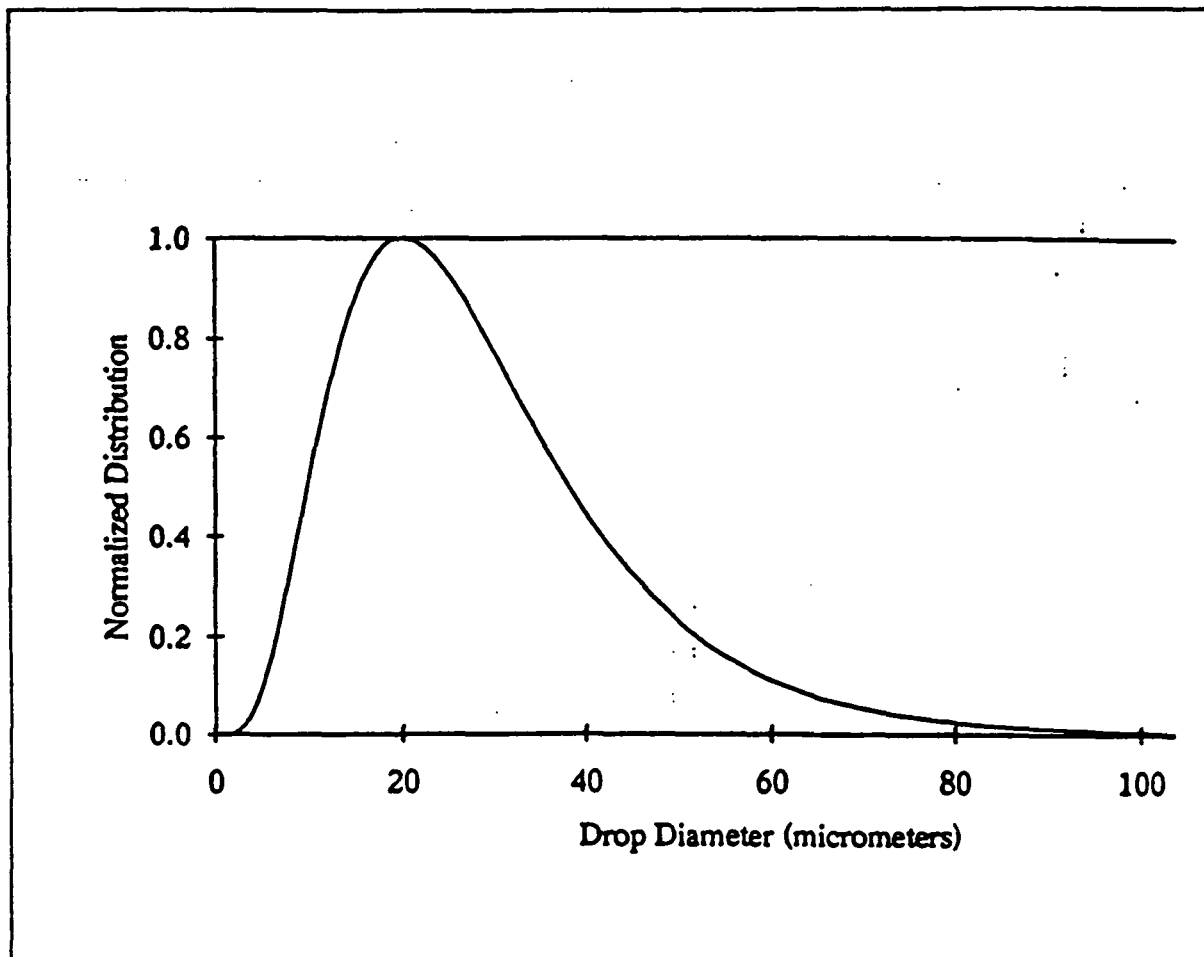


Figure 3-6: Normalized Deirmendjian of top layer for the steady rain 3 mm/hr model (21-2)

3.3.2 Comparison of Theoretical Results With and Without Precipitation Scattering

Wu and Fung compared the apparent temperature with and without the effect of precipitation backscatter. In their analysis, Valley's [27] rain model was employed to provide the precipitation rate and altitude extent. The effect of scatter for a frequency of 13.9 GHz at a wind speed of 5 and 10 m/s with a precipitation rate of 10 mm/hr is shown in the Figure 3-7 . Approximately a 10 K decrease in apparent temperature occurs when the effect of scattering is considered. However, Valley's rain models include rain falling from an altitude of 3 km, which is excessive. Thus, more realistic condition would yield an apparent temperature decrease less than 10 K at 13.9 GHz. At lower frequencies, fewer of the rain drops will exhibit diameters comparable to the wavelength. Wu and Fung [34] showed that the scattering due to precipitation particles is negligible for precipitation rate less than 10 mm/hr and frequencies below 9 GHz. At higher frequencies the wavelength is comparable to the particle size and the effect of scattering is appreciable. Backscatter tends to lower apparent temperature from that which would be observed without backscatter. In addition, the decrease is fairly constant with varying look angle.

The difference between the apparent temperature and the brightness temperature of the surface is defined as the excess apparent temperature.

$$T_{\text{ex}j}(z, \theta) = T_{\text{a}j}(z, \theta) - T_B(\theta) \quad (3.38)$$

where

$T_{\text{ex}j}(z, \theta)$ = excess apparent temperature at the altitude z , and nadir angle θ

$T_B(\theta)$ = surface brightness temperature = $\epsilon_j(\theta)T_g$

If there were not atmospheric attenuation, apparent temperature and bright-

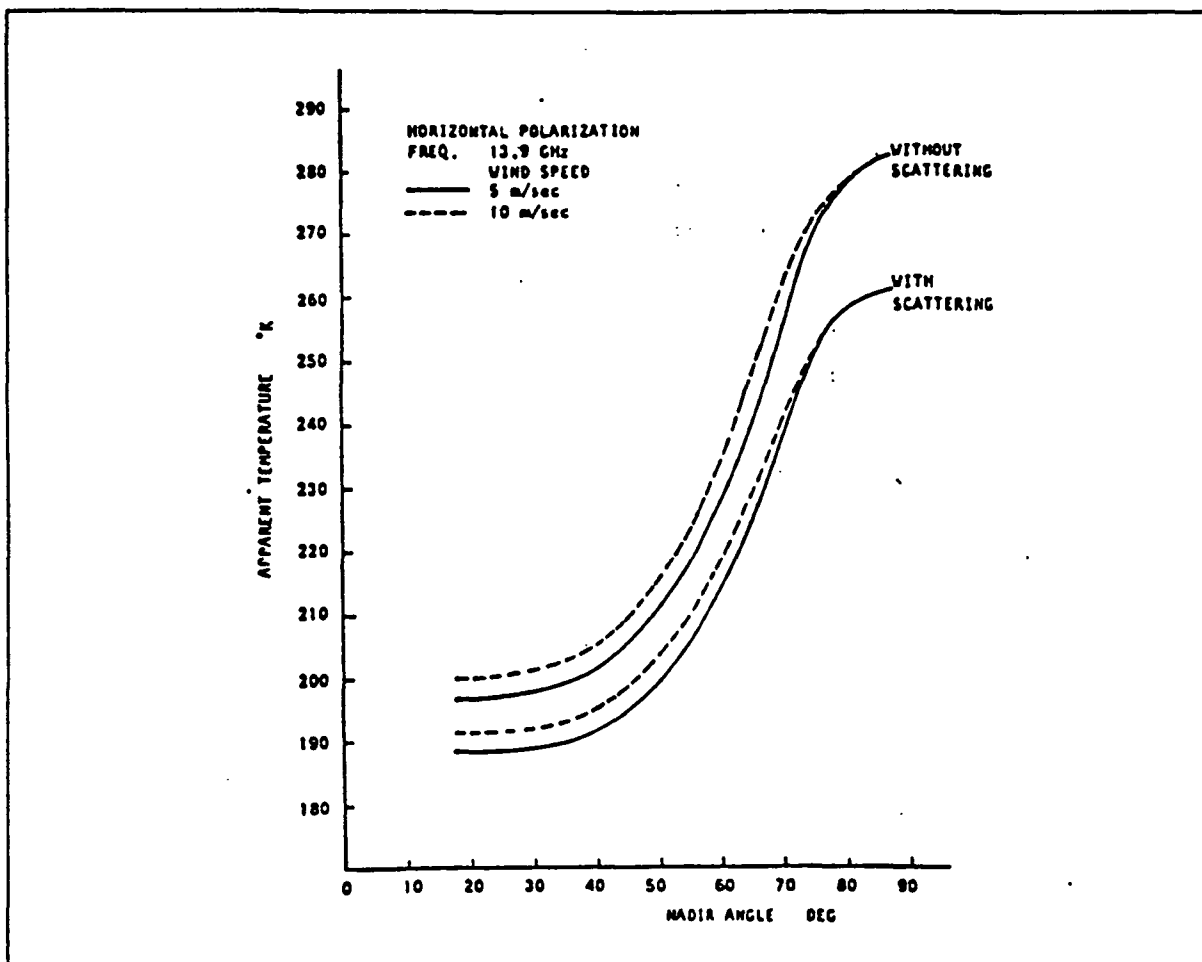


Figure 3-7: Effect of scattering on apparent temperature measurement

ness temperature would be equal, so excess apparent temperature would be zero.

3.4 Relation between Attenuation and Excess Apparent Temperature

3.4.1 Relation at Single Frequency

The atmospheric attenuation has an approximately cubic dependence on excess apparent temperature at the same frequency [Dome, 1980]. In practice, the relationship between attenuation and excess brightness temperature, may be modeled as

$$\alpha(\theta) = A_1 T_{ex}(\theta) + A_2 T_{ex}^2(\theta) + A_3 T_{ex}^3(\theta) \quad (3.39)$$

where A_1 , A_2 and A_3 are empirical coefficients.

It is necessary to model the absorption coefficient for each layer of the assumed horizontally uniform atmosphere, if the simplified radiative transfer equation is to be evaluated. A standard atmosphere model cited by Ulaby (1973) gives the temperature, pressure, and water vapor variations with height.

$$\text{Pressure :} \quad P(z) = P_0 e^{-z/\tau} \quad (3.40)$$

$$\text{Temperature :} \quad T(z) = \begin{cases} T_0 - 6.5z & 0 \leq z \leq 11 \text{ km} \\ T(11) & 11 \leq z \leq 25 \text{ km} \\ T(11) + 3.0(z - 25) & 25 \leq z \leq 47 \text{ km} \end{cases} \quad (3.41)$$

$$\text{Humidity : } \rho(z) = \begin{cases} \rho_s e^{-z/2.1} & 0 \leq z \leq 16 \text{ km} \\ \rho(16) e^{(z-16)/4.2} & 16 \leq z \leq 31 \text{ km} \end{cases} \quad (3.42)$$

where

T_s = surface temperature in $^{\circ}K$

P_s = surface pressure in mm of Hg

ρ_s = surface water vapor density in gm/m^3

z = altitude in km

Clear-sky absorption coefficient can be computed using the standard atmosphere values, but more information is needed if clouds and/or rain are present. Cloud conditions vary from light overcast to heavy overcast and rain rate can be classified as light, moderate and heavy. The Porter and Kreiss cloud models have been discussed already. Valley's rain models characterize light to heavy rainfall. The relation between the attenuation and the excess apparent temperature can be considered approximately linear under non-extreme conditions. The models for cloud and rain can be used to calculate the total absorption coefficient values. These values can then be used to compute attenuation values and their corresponding excess apparent temperature values. In this way a plot of total attenuation versus excess apparent temperature is generated.

Using Porter's cloud models and Valley's rain models, Dome [35] calculated plots of attenuation versus excess apparent temperature for an operating frequency of 10.69 GHz. Note that each model yields one point in Figure 3-8. A similar plot can be obtained using the same surface conditions, and the same models, but a frequency of 37 GHz. It is plausible that the points in the 10.69 GHz case follow a cubic trend, but not so for 37 GHz. In the 37 GHz case, the points resulting from cloud models and those from rain models follow different trends as shown

in Figure 3-9. The cloud-model points might still follow a cubic trend, but the rain model points lie nearly on a vertical straight line. The rain model points are different because the excess apparent temperature saturates in the presence of rain at this high frequency. The radiometer doesn't even sense any radiation from the surface. Instead, it senses the clouds and rain. In terms of the radiative transfer equation the apparent temperature is equal to the atmospheric temperature:

$$T_{aj}(z, \theta) = T_{atm}(z, \theta) \quad (3.43)$$

For this reason, the excess apparent temperature can increase no more. At the high frequency of 37 GHz, even light rain causes saturation. Hence a microwave radiometer operating at this frequency level can be used to detect the presence of rain, but not to estimate its intensity.

Measured apparent-temperature values can be no greater than the highest temperature in the field of view of the radiometer. This implies that excess apparent temperature itself has a theoretical maximum value $T_{aj}(max)$. Assuming Ulaby's atmospheric temperature profile model (1973), the air temperature does not increase with increasing altitude until a height of 25 km has been reached. However, above this level, atmospheric emission is negligible, so that the radiometer cannot sense air temperatures in this region. Therefore, the effective radiometer field of view will contain no portion of the atmosphere above 25 km. Since the maximum air temperature in the lower 25 km of the atmosphere is attained at the surface, the maximum theoretical apparent temperature value $T_a(max)$ is given by:

$$T_a(max) = T_{air}(0) = T_g \quad (3.44)$$

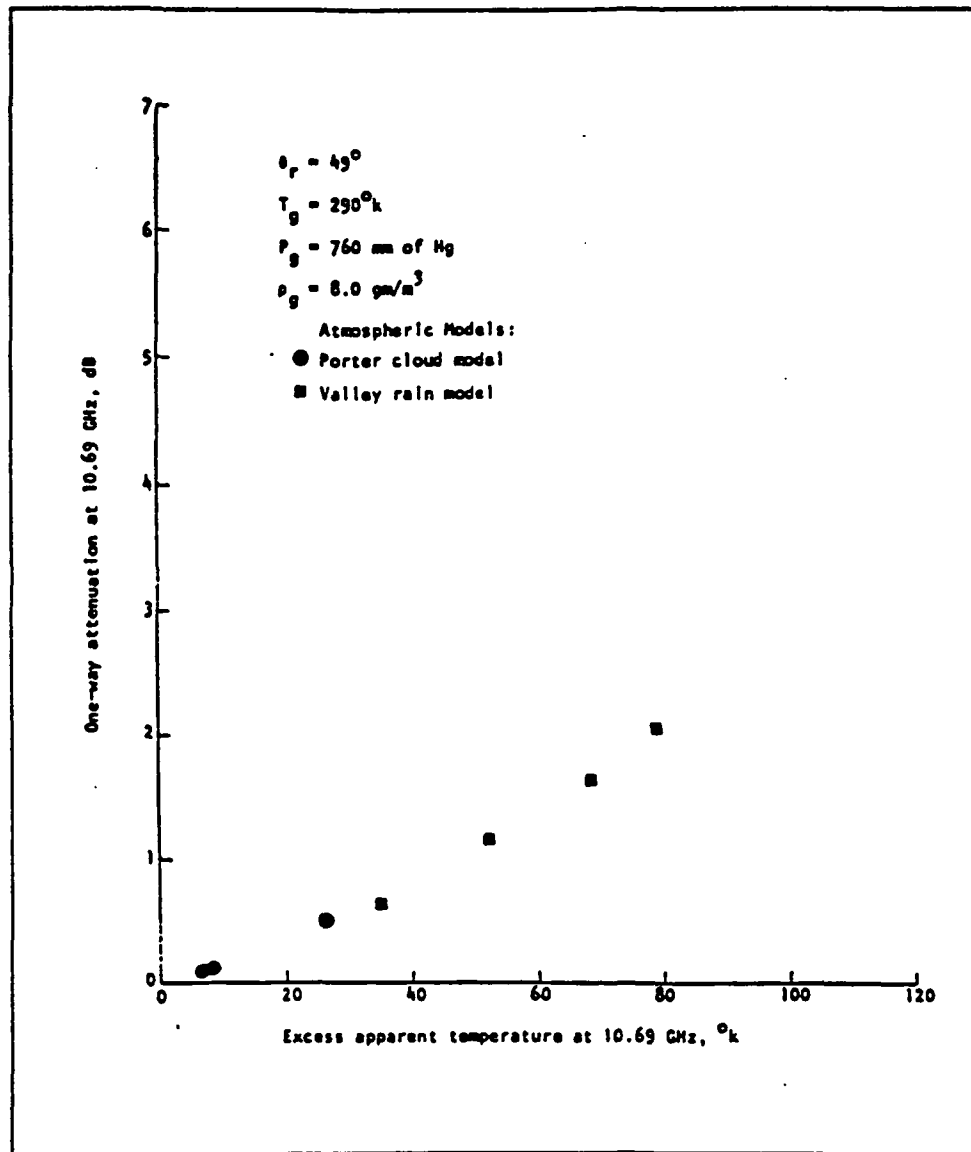


Figure 3-8: Excess Apparent Temperature versus Total Atmospheric Attenuation at 10.69 GHz [Dome, 1980]

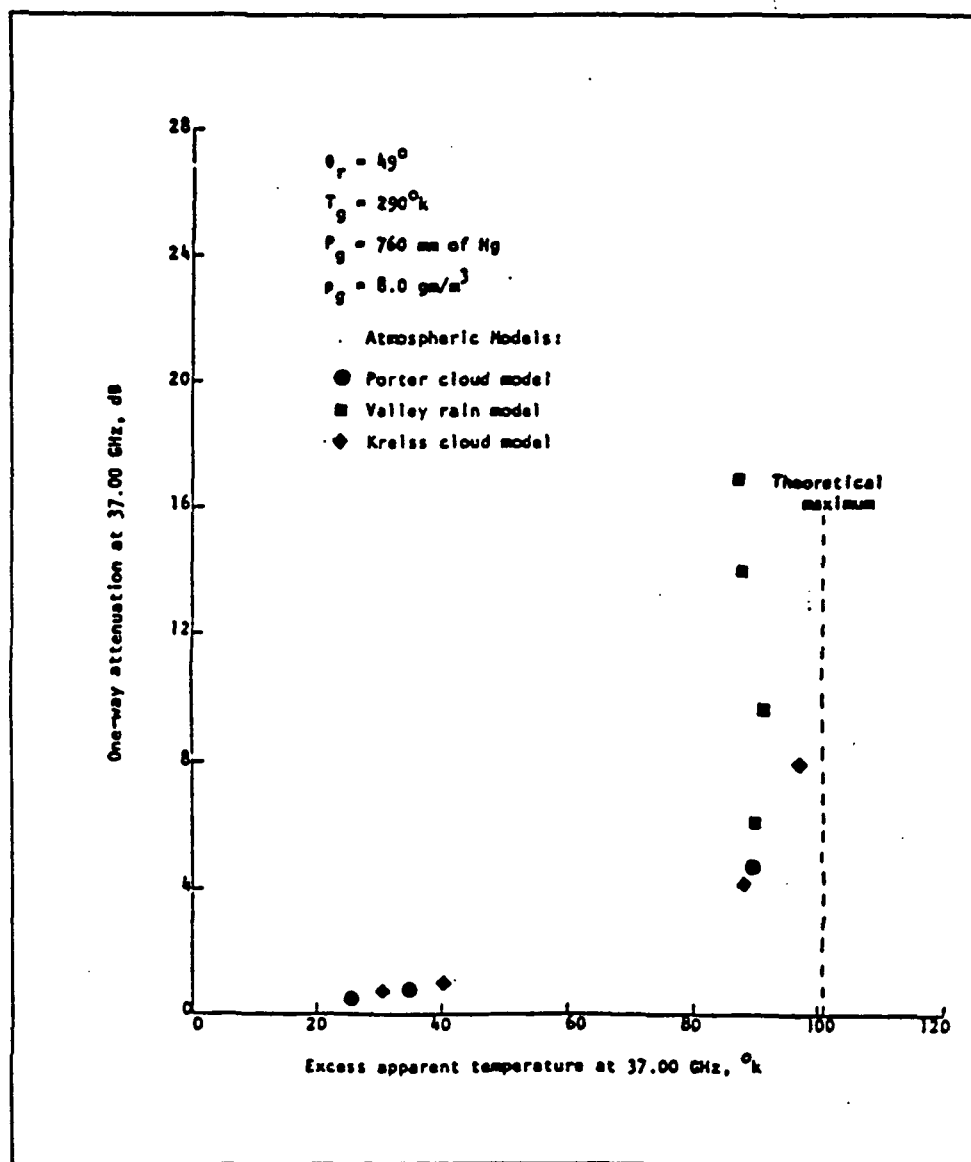


Figure 3-9: Excess Apparent Temperature versus Total Atmospheric Attenuation at 37 GHz [Dome 1980]

The maximum value of the excess apparent temperature is given by

$$T_{\text{ex}}(\text{max}) = T_a(\text{max}) - T_B = T_g(1 - \epsilon) \quad (3.45)$$

Ignoring for now the problem of saturation at high frequency, the procedure for estimating total atmospheric attenuation at a given incidence angle, surface temperature, pressure, and water vapor density, by means of apparent temperature measurements made at the same frequency involves the following steps:

1. Relate total attenuation and the excess apparent temperature at a single frequency.
2. Compute the excess apparent temperature from the apparent temperature.
3. Compute the total attenuation by using excess apparent temperature from 2 in the relation developed in step 1.

3.4.2 Errors of the attenuation estimate

The attenuation estimate from the excess apparent temperature involves two types of errors. The first type is due to the sensitivity of the cubic fit to the errors in apparent temperature, which in turn appear as errors in the excess apparent temperature. This will be the only error if the cubic fit is assumed to be perfect. If the cubic fit is not perfect, which is usually true, there will always be some error in the attenuation estimate regardless of the magnitude of error in the excess apparent temperature estimate. The errors due to the estimation of the apparent temperature can be reduced by improving the accuracy of the radiometer, while the error due the cubic fit can be reduced by obtaining a better fit . The extent of error in apparent temperature that can be tolerated for a desired bound in the attenuation estimate error is the key question.

3.4.3 Theoretical Relation at Different Frequencies

The problem of relating total atmospheric attenuation at a given frequency, f_1 , to excess apparent temperature at some other frequency, f_2 , can be broken into two parts:

1. Computing the total atmospheric attenuation from the excess apparent temperature at the same frequency (f_1).
2. Use of frequency dependence of the total atmospheric attenuation to compute total atmospheric attenuation at the scatterometer frequency (f_2).

Total atmospheric attenuation is given by:

$$\alpha_T = \sec\theta \int_0^\infty \alpha(z) dz \quad (3.46)$$

where

$\alpha(z)$ is the absorption coefficient at altitude z

The absorption coefficient is also frequency dependent, but its frequency dependence is independent of its altitude dependence.

$$\alpha(z, f) = K(z)\alpha(z_0, f) \quad (3.47)$$

where

$K(z)$ = altitude dependent constant

3.4.4 Frequency Dependence of the Absorption Coefficient at a Fixed Altitude

The total atmospheric attenuation has a quadratic dependence on frequency. The theory and equations to derive the frequency dependence of the absorption coefficient at a fixed altitude appears in [35].

3.4.5 Attenuation vs. Excess Apparent Temperature at Different Frequencies

To determine the relation between the attenuation and apparent temperature at different frequencies the same approach as before is followed. The attenuation for an excess apparent temperature at a particular frequency is calculated as before. Then using the frequency dependency of the attenuation, the attenuation at the frequency of interest is obtained. Now a plot of excess apparent temperature at a particular frequency versus the attenuation at some other frequency can be obtained. Figure 3-10 shows one such plot.

3.5 Dependence of Regression Coefficients on the Surface Parameters

3.5.1 Dependence on Surface Pressure

Both molecular-oxygen and water-vapor absorption coefficients are functions of pressure. Since the pressure profile depends on surface pressure, the component of atmospheric attenuation due to clear sky conditions is a function of surface pressure. If rain and/or clouds are present, clear-sky absorption is negligible, as long as the frequency avoids the resonant absorption lines. If the atmosphere is clear, attenuation is caused by clear sky absorption only. In this case surface

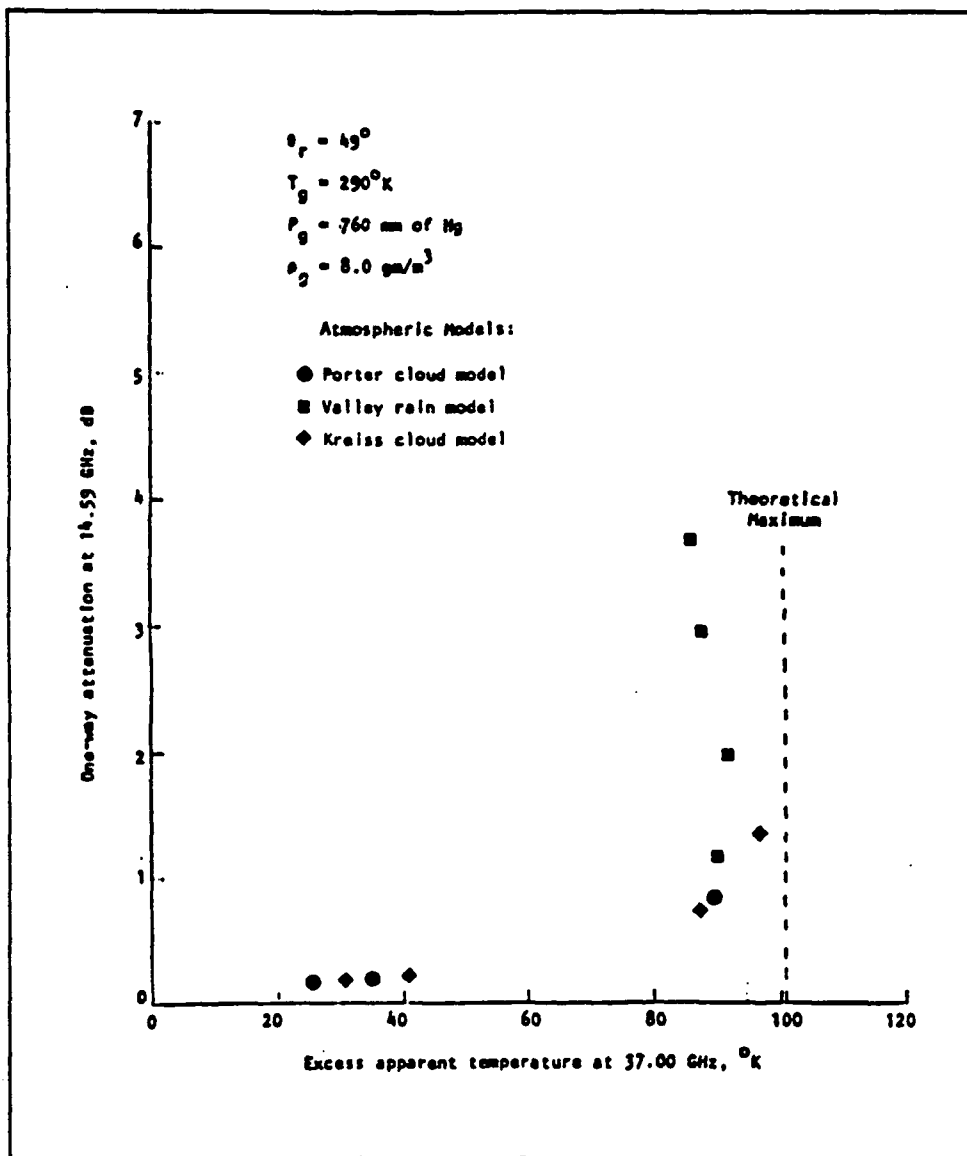


Figure 3-10: Attenuation vs. Excess Apparent Temperature at Different Frequencies

pressure variation has a significant effect on total atmospheric attenuation, in terms of percent, but a small effect in terms of magnitude.

3.5.2 Dependence on Surface Water Vapor Density

If the surface water vapor density is neglected the percentage change in attenuation is quite large for Porter's medium and light overcast models where clear sky absorption is important. The decrease in total atmospheric attenuation caused by the complete removal of water vapor is nearly constant at some small value. Hence, ignoring variation of surface water vapor density about its assumed value leads to a very small error in the correction for total atmospheric attenuation.

3.5.3 Dependence on Surface Temperature

The dependence of total atmospheric attenuation on surface temperature cannot be removed because the coefficients of the cubic fit as well as the cutoff level for the excess apparent temperature at 37 GHz are functions of surface temperature. Linear interpolation of coefficients and cutoff level with respect to the surface temperature results in interpolation error. A 5 K spacing of surface temperatures at which the coefficients and cutoff are computed ensures a small interpolation error. The temperature dependence of the coefficients in the cubic relation are shown in Figures 3-11 through 3-13 for ocean.

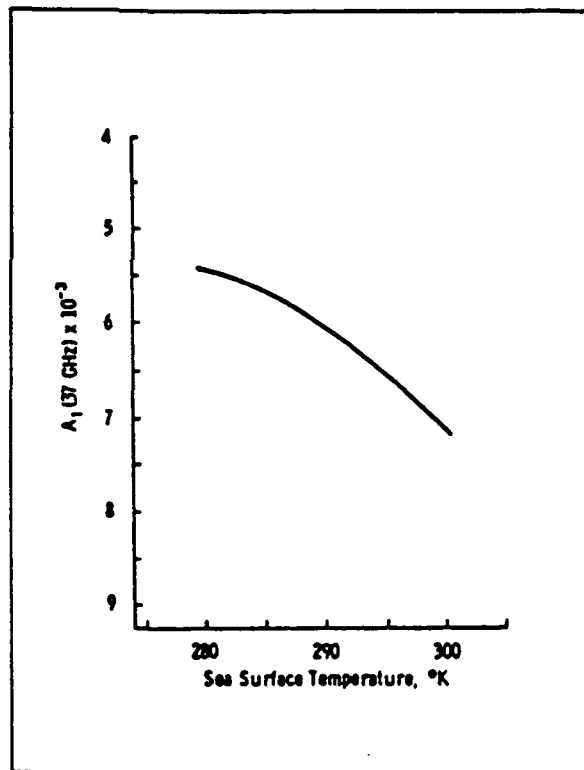


Figure 3-11: Temperature dependence of regression coefficient A_1

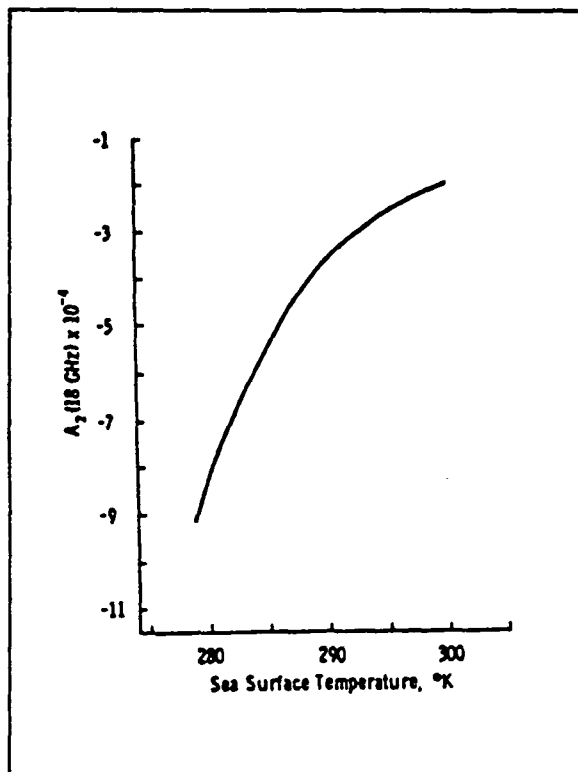


Figure 3-12: Temperature dependence of regression coefficient A_2

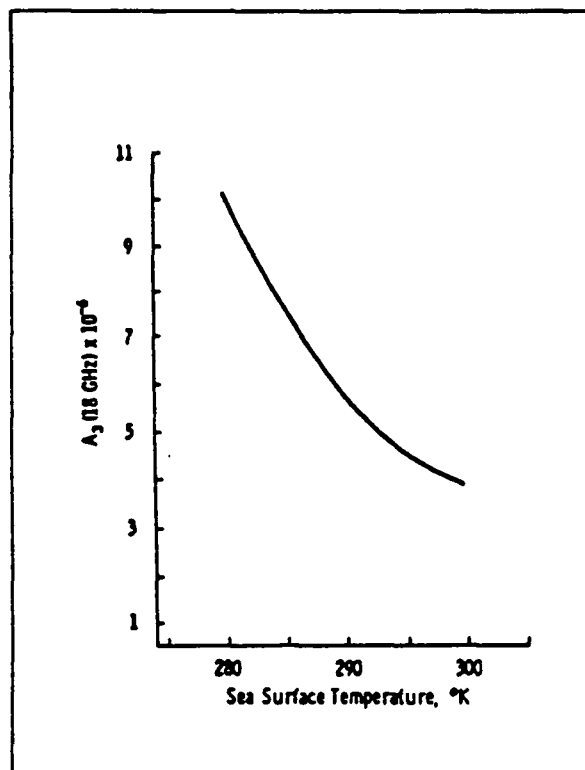


Figure 3-13: Temperature dependence of regression coefficient A_3

Chapter 4

SeaWinds scatterometer & AMSR Radiometer

4.1 SeaWinds Scatterometer

The SeaWinds Scatterometer instrument is currently being developed by NASA/JPL, as a part of the EOS program, for flight on the Japanese ADEOS II mission in 1999. The function of this Ku-Band radar scatterometer is to infer global sea surface wind speed and direction by measuring the normalized backscatter cross-section, σ^0 , of the sea-surface over several different azimuth angles. Previous scatterometer experiments have shown that the radar backscattering coefficient of the sea is a function of the surface wind speed and the wind direction relative to the radar viewing angle. By matching the radar measurements and the experimentally acquired radar backscattering model function, the sea-surface wind speed and direction can be estimated. Based on the wind-related surface scattering models obtained from previous scatterometer flights, the anticipated wind detection performance for the SeaWinds instrument is a speed error of 2 m/s for wind speed up to 20 m/s, and a direction error of 20 degrees or less. Near-global coverage will be obtained every two days.

A set of key parameters for the SeaWinds instrument is given in Table 4.1. The SeaWinds radar scatterometer has a transmitter operating at a carrier frequency of 13.402 GHz, and a nominal power of 110 Watts. The transmitted pulse rate is 192 Hz, with a pulse width of 1.5 milliseconds. A 1.1 m antenna will produce two "pencil" beams. The beamwidth of each one of the two beams is approximately 1.6 degrees. Tapered aperture illumination is applied to suppress sidelobes. The elevation pointing angles for the two beams are approximately 40 and 46 degrees. The radar antenna will scan conically with respect to nadir. At the planned orbit height of 800 km, the conical scan of the two pencil beams will produce a radar measurement swath of up to 900 km on each side of the satellite track. The swath area within 700 km of the satellite subtrack will be covered by scan circles of both the beams. The sea surface from 200 to 700 km from the track will be considered the primary swath of the SeaWinds instrument because the greater number of azimuthal measurements will improve the wind retrieval performance. The two-way antenna radiation pattern on the surface has a half power width of about 25 by 40 km. This dimension corresponds to the resolution of the radar σ^0 measurement cells. A wind vector cell is obtained by registering and merging σ^0 cells from several azimuthal look directions, and then estimating the wind vector for that co-registered location. The desired wind cell resolution of SeaWinds is $50 \times 50 \text{ km}$. The SeaWinds conical scan speed will be at 16 rpm, or 3.75 seconds per revolution. Combined with a radar pulse transmission rate of 192 Hz, which alternates between the two beams, the σ^0 measurement cells for a common scan beam will be spaced by 1 degree, or about 15 km, in azimuth. At a satellite track speed of about 6.6 km per second, the along-track space of σ^0 samples will be approximately 25 km. The conical scan design represents a change from the fixed fan-beam antennas of previous NASA and ESA spaceborne scatterometers. The purpose of this change is a more compact design consistent with the accommodation constraints of the ADEOS II spacecraft.

Table 4.1: SeaWinds Key Parameter Table

Parameter	Value - H	Value - V
Altitude	800 km	
Orbit Period	102 minutes	
Frequency	13.402 GHz	
Peak Power	110 Watts	
Pulse Width	1.5 milliseconds	
Modulation	40 KHz Bandwidth (3 dB)	
PRF	192 Hz	
Antenna Size	Approx. 1.1 m dish	
No. of Beams	2	
Look Angle	40 degrees	46 degrees
Beam Width	1.6 deg	1.4 deg
Polarization	H	V
Incidence Angle	47 deg	54 deg
Scan Rotation Period	3.75 seconds	
Receiver Sensitivity	-135 dBm	
Receiver Dynamic Range	45 dB min	
Total Noise Figure	4 dB max	
Doppler Range	+/- 500 kHz	
Delay Range	6.5 to 9.0 milliseconds	
Doppler Filter BW	80 kHz	
Noise Filter BW	1 MHz	
Radar σ^0 Accuracy	0.5 dB relative in 3 months	
Mission Life	3 Years min	

Table 4.2: AMSR Main Performance Summary

Frequency	6.6 GHz	10.65 GHz	18.7 GHz	23.8 GHz	36.5 GHz
Bandwidth	400 MHz	100 MHz	200 MHz	400 MHz	1000 MHz
Polarization	V&H	V&H	V&H	V&H	V&H
Temperature Resoultion (K = 1)	0.24 K	0.60 K	0.59 K	0.47 K	0.59 K
Temperature Resoultion (K \geq 1)	0.30 K	0.63 K	0.65 K	0.57 K	0.74 K
K =	1.22	1.06	1.12	1.22	1.27
Integration Time	2.6 msec	2.6 msec	2.6 msec	2.6 msec	1.3 msec
3 dB Beam Width (EL)	1.87 deg	1.19 deg	0.65 deg	0.59 deg	0.34 deg
3 dB Beam Width (AZ)	1.84 deg	1.17 deg	0.65 deg	0.63 deg	0.33 deg
IFOV (EL)	71.7 Km	45.6 Km	24.9 Km	22.6 Km	13.0 Km
IFOV (AZ)	40.4 Km	25.7 Km	14.3 Km	13.8 Km	7.3 Km
Spatial Resolution (EL)	71.7 Km	45.6 Km	24.9 Km	22.6 Km	13.0 Km
(AZ)	50.4 Km	35.7 Km	24.3 Km	23.8 Km	12.3 Km
Sampling Interval (EL)	10 Km	10 Km	10 Km	10 Km	5 Km
(AZ)	10 Km	10 Km	10 Km	10 Km	5 Km
Overlap Rate (EL)	0.861	0.781	0.598	0.558	0.616
(AZ)	0.802	0.720	0.588	0.581	0.592
Beam Efficiency	0.944	0.941	0.962	0.967	0.947
Spillover	0.028	0.026	0.015	0.01	0.023
Cross Polarization	0.01	0.01	0.009	0.008	0.01
No. of Feed Horn Ant.& Recv	1	1	1	1	2

4.2 AMSR Radiometer

The main performance summary of the AMSR(Advanced Microwave Scanning Radiometer) is given in Table 4.2

Chapter 5

Simulations

5.1 Different stages in simulation

The simulation of combined scatterometer-radiometer systems for accurate wind-vector determination involves the following stages:

- Define parameters for scatterometer and radiometer systems
- Select models which characterize the scatterometer and radiometer measurements
- Based on the scan geometry of both instruments, select an area of interest and pick measurements by these instruments in selected area
- Simulate conditions of rain and/or cloud over the area of interest
- Obtain the backscattering coefficient and apparent temperature measurement after taking into account the attenuation suffered due to rain and/or cloud. These are effectively the measurements available for the user to process and infer surface wind speed
- Using the radiometer measurements, the scatterometer measurements are corrected using an iterative procedure

- Simplify wherever necessary (like rectangular footprints), to avoid unnecessary complication without affecting main problem

5.2 Simple cases to illustrate correction algorithm

It is easier to understand the correction algorithm with simple case before simulating a complex case. To demonstrate the correction algorithm the following simple cases are considered:

- The simplest case has identical footprints for scatterometer and radiometer. Assuming the same value of attenuation over the entire cell simplifies it further.
- Assuming identical footprints as before but 2 or more sub-cells reflects a more practical situation. Here, all sub-cells are assumed to be of equal area and the attenuation within a subcell is assumed to be constant at some value.

5.2.1 Identical scatterometer & radiometer cells

The assumption for this simulation are :

1. The incidence angle is assumed to be 55° ;
2. Only upwind direction ($\phi = 0^\circ$) is considered;
3. Scatterometer & radiometer cells are assumed to be identical and rectangular in shape;
4. The footprints are assumed to be divided into identical sub-cells;
5. Attenuation inside each sub-cell is assumed to be the same;

6. Excess temperature (which in turn gives attenuation) is assumed to be known;
7. Ocean surface temperature is assumed to be constant over the area of interest.

The required inputs for this simulation are :

1. True surface wind speed;
2. Excess brightness temperature (T_{es}) in the area of interest;
3. Maximum number of iterations for correction procedure.

The simulation process can be divided into three broad sections:

1. Simulation of the scatterometer measurements
2. Simulation of radiometer measurements
3. Correction algorithm

Using the SASS model function the ocean normalized radar cross section is obtained for a true surface wind vector.

$$\sigma_{dB}^o = 10[G(\theta, \phi) + H(\theta, \phi)\log_{10}U] \quad (5.1)$$

$$\sigma^o = 10^{\frac{\sigma_{dB}^o}{10}} \quad (5.2)$$

where

$$\theta = 55^\circ,$$

$$\phi = 0^\circ \text{ (upwind direction),}$$

G , H are the coefficients for the SASS model function,

$$G = -3.494, H = 1.724,$$

U = true surface wind speed.

For assumed excess temperature over each sub-area the corresponding attenuation(at 14.6 GHz) is calculated using the cubic relationi [34].

$$\alpha_{14_db}(sub_cell) = A_1 T_{ex}(sub_cell) + A_2 T_{ex}^2(sub_cell) + A_3 T_{ex}^3(sub_cell) \quad dB \quad (5.3)$$

where A_1, A_2 and A_3 are empirical coefficients. For surface temperature of 290 K

$$A_1 = 1.4 \times 10^{-2}$$

$$A_2 = -3.5 \times 10^{-4}$$

$$A_3 = 5.7 \times 10^{-6}$$

For surface temperature of 300 K

$$A_1 = 9.73 \times 10^{-3}$$

$$A_2 = -1.943 \times 10^{-4}$$

$$A_3 = 3.53 \times 10^{-6}$$

A plot of the cubic relation between excess brightness temperature at 18.7 GHz and attenuation at 14.6 GHz is shown in Figure 5-1. The cubic relation giving attenuation at 14.6 GHz has been established [36]. We use the same relation and scale the attenuation to the frequencies of interest.

Using frequency scaling the attenuation at scatterometer frequency (13.4 GHz) and radiometer frequency (18.7 GHz) are calculated.

$$\alpha_{dB_{scat}}(sub_cell) = \alpha_{14_dB}(sub_cell) \times \left(\frac{13.4}{14.6}\right)^2 \quad dB \quad (5.4)$$

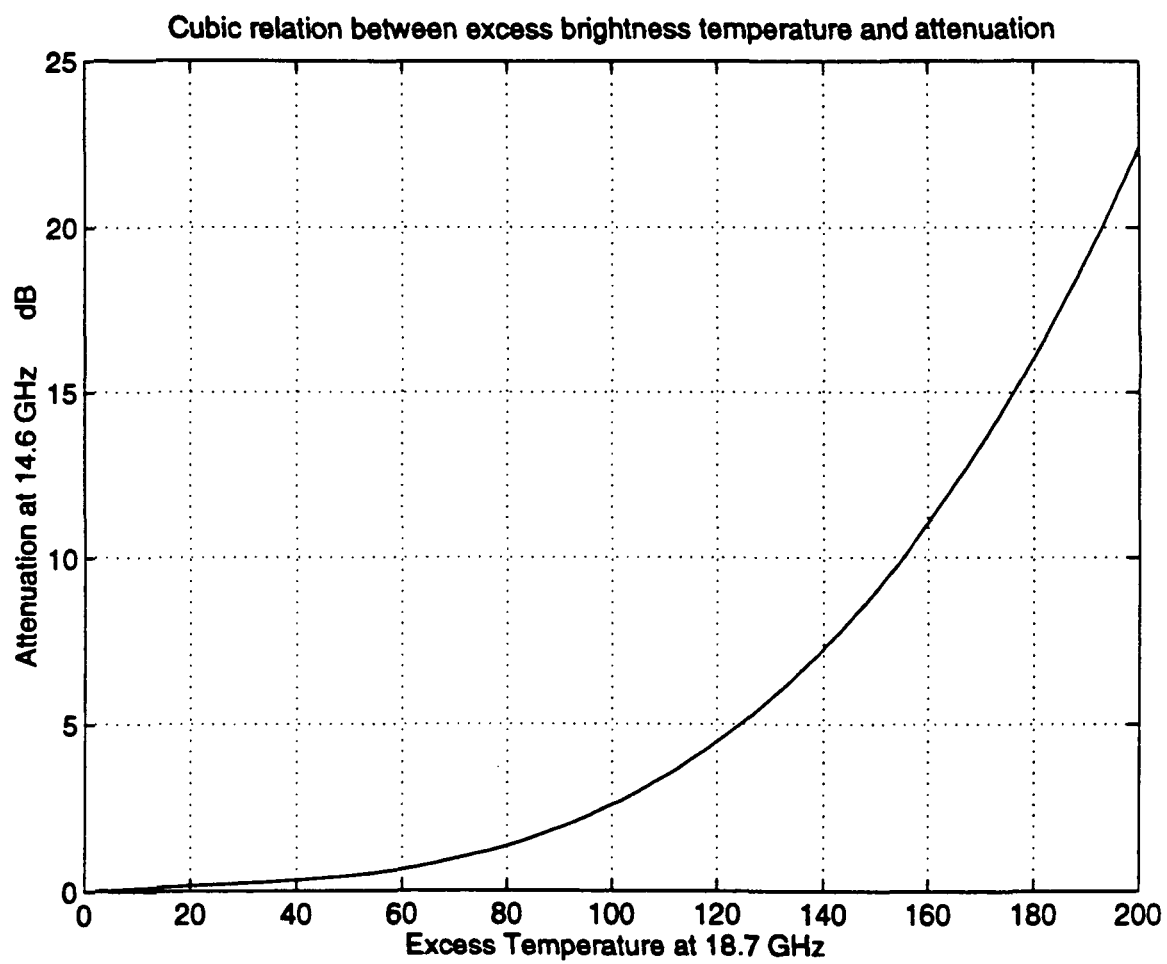


Figure 5-1: Cubic relation between excess brightness temperature and attenuation

$$\alpha_{dB_{rad}}(sub_cell) = \alpha_{14d} B(sub_cell) \times \left(\frac{18.7}{14.6}\right)^2 \quad dB \quad (5.5)$$

The attenuation values in nepers are

$$\alpha_{scat}(sub_cell) = \frac{\alpha_{dB_{scat}}(sub_cell)}{8.686} \quad Np \quad (5.6)$$

$$\alpha_{rad}(sub_cell) = \frac{\alpha_{dB_{rad}}(sub_cell)}{8.686} \quad Np \quad (5.7)$$

The surface contribution of brightness temperature at 18.7 GHz for H-polarization is given by [37]

$$TB_{wind}(u) = 82 + 1.06 \times u \quad (5.8)$$

The surface contribution is attenuated before the radiometer measures it, the attenuated surface contribution is

$$TB_{attn_{wind}}(sub_cell) = TB_{wind} \times \exp(-\alpha_{rad}(sub_cell)) \quad (5.9)$$

The scatterometer signal is also attenuated, but is attenuated twice. The measured scattering coefficient for each sub-cell is therefore

$$\sigma^o_{measured}(sub_cell) = \sigma^o \times \exp(-2 \times \alpha_{scat}(sub_cell)) \quad (5.10)$$

The σ° actually measured by the scatterometer is

$$\sigma^\circ_{measured} = \frac{\sum_{i=1}^N \sigma^\circ_{measured}(sub_cell)}{N} \quad (5.11)$$

The apparent temperature of each sub-cell in the radiometer footprint is

$$TB_{apparent}(sub_cell) = TB_{attn_wind}(sub_cell) + T_{es}(sub_cell) \quad (5.12)$$

The apparent temperature actually measured by the radiometer is the average apparent temperature of all sub-cells

$$TB_{avg_apparent} = \frac{\sum_{i=1}^N TB_{apparent}(sub_cell)}{N} \quad (5.13)$$

The $\sigma^\circ_{measured}$ and $TB_{avg_apparent}$ are inputs to the correction algorithm. An initial guess for the surface wind speed is set at some value u_{bias} . The surface brightness contribution if the wind speed was u_{bias} is calculated as

$$TB_{bias} = 82 + 1.06 \times u_{bias} \quad (5.14)$$

The excess brightness temperature, which is the contribution from intervening sources like clouds, rain and atmospheric gases is calculated by subtracting the contribution of the surface from the total apparent temperature measured by the radiometer.

$$TB_{est_es} = TB_{avg_apparent} - TB_{bias} \quad (5.15)$$

Since the value of attenuation hasn't been estimated yet, the TB_{bias} is not attenuated before calculating TB_{est_ss} .

An estimate of attenuation is made from TB_{est_ss} and it is scaled to get attenuation estimate at radiometer and scatterometer frequencies.

The measured σ^o is corrected for attenuation suffered using the attenuation estimate α_{13_est} .

$$\sigma_{corrected}^o = \sigma_{measured}^o \times \exp(2 \times \alpha_{13_est}) \quad (5.16)$$

$$\sigma_{dB_{corrected}}^o = 10 \times \log_{10}(\sigma_{corrected}^o) \quad (5.17)$$

Surface wind speed can be estimated from corrected sigma by inverting the SASS model function.

$$u_{est} = 10^{\frac{\sigma_{dB_{corrected}}^o - 10G}{10H}} \quad (5.18)$$

The wind speed error is the difference between the u_{est} and the true wind speed u .

$$u_{error} = u_{est} - u \quad (5.19)$$

Using the u_{est} as the new wind bias u_{bias} , the surface contribution is calculated

$$TB_{bias} = (82 + 1.06 \times u_{est}) \times \exp(-\alpha_{18_est}) \quad (5.20)$$

$\exp(-\alpha_{18_{est}})$ accounts for the loss to the surface contribution.

Using this new surface contribution the excess brightness temperature is calculated. An attenuation estimate corresponding to this new value of excess is made and this new attenuation estimate is used to correct the measured sigma to again get an estimate of wind speed. This iterative procedure is continued till the wind error drops to zero or there is no appreciable improvement in wind speed estimation. Care should be taken that iterative procedure doesn't increase the error in the other direction.

5.2.2 Simulation results for some simple cases

For the simplest case with identical radiometer and scatterometer footprints with attenuation the same over the entire cell, values of wind speed estimates are tabulated in Table 5.1 through Table 5.3 for different values of excess brightness temperature (hence attenuation) and for three different values of true wind speed.

In each table the different columns are results of the iterative process (limited to 10 iterations) for different values of excess brightness temperatures (hence attenuation). For $T_{es} = 0$ K, which implies no attenuation, the wind speed estimate is always close to the true wind speed. As the T_{es} increases, the initial estimates of wind speed are bad. But with the iterative procedure the wind speed estimate improves and after 20-25 iterations the estimated wind speed is pretty close to the actual wind speed. Results for only ten iterations are shown in the tables to illustrate the correction process.

For values of T_{es} between 100-150 K the improvement in wind estimate is relatively slow. This might be because the contribution from the surface and that from the clouds and rain are comparable. The iterative process takes a while to estimate the true excess and hence the true attenuation to the radar signal.

Table 5.1: Wind Estimate in m/s for a True Wind Speed = 20 m/s

T_{∞} K	0	50	70	80	100	120	150	200
Iteration #								
1	20.1933	20.0926	19.5709	18.9371	16.7354	13.5402	8.2933	2.3323
2	20.0309	20.0246	19.7930	19.3712	17.5026	14.4358	9.3865	5.0940
3	20.0051	20.0065	19.8990	19.6213	18.0516	15.1536	10.5638	13.1694
4	20.0008	20.0017	19.9505	19.7697	18.4625	15.7591	11.8794	18.9858
5	20.0001	20.0005	19.9756	19.8592	18.7780	16.2833	13.3194	19.9046
6	20.0	20.0001	19.9880	19.9137	19.0241	16.7436	14.7995	19.9915
7	20.0	20.0	19.9941	19.9470	19.2179	17.1505	16.1875	19.9993
8	20.0	20.0	19.9971	19.9674	19.3718	17.5110	17.3608	19.9999
9	20.0	20.0	19.9986	19.9799	19.4944	17.8306	18.2594	20.0
10	20.0	20.0	19.9993	19.9876	19.5926	18.1134	18.8934	20.0

Table 5.2: Wind Estimate in m/s for a True Wind Speed = 10 m/s

T_{∞} K	0	50	70	80	100	120	150	200
Iteration #								
1	10	9.8799	9.5531	9.2289	8.1727	6.6535	4.1102	1.1643
2	10	9.9703	9.7988	9.5709	8.6597	7.1884	4.7150	2.5703
3	10	9.9926	9.9072	9.7548	8.9950	7.6148	5.3800	6.6827
4	10	9.9981	9.9567	9.8581	9.2381	7.9731	6.1307	9.5346
5	10	9.9995	9.9798	9.9174	9.4188	8.2807	6.9432	9.9585
6	10	9.9999	9.9905	9.9517	9.5550	8.5467	7.7467	9.9965
7	10	10.0	9.9955	9.9717	9.6584	8.7769	8.4526	9.9997
8	10	10.0	9.9979	9.9834	9.7375	8.9753	9.0016	10.0000
9	10	10.0	9.999	9.9903	9.7980	9.1453	9.3860	10.0000
10	10	10.0	9.9995	9.9943	9.8445	9.2901	9.6347	10.0000

Table 5.3: Wind Estimate in m/s for a True Wind Speed = 5 m/s

T_{ex} K	0	50	70	80	100	120	150	200
Iteration #								
1	4.9677	4.9096	4.7322	4.5673	4.0457	3.3010	2.0465	0.5817
2	4.9949	4.9784	4.8831	4.7658	4.3138	3.5899	2.3637	1.2910
3	4.9992	4.9947	4.9475	4.8695	4.4954	3.8199	2.7160	3.3659
4	4.9999	4.9987	4.9761	4.9263	4.6252	4.0127	3.1154	4.7774
5	5.0	4.9997	4.9891	4.9582	4.7201	4.1773	3.5440	4.9807
6	5.0	4.9999	4.9950	4.9762	4.7903	4.3182	3.9580	4.9984
7	5.0	5.0	4.9977	4.9864	4.8427	4.4384	4.3088	4.9999
8	5.0	5.0	4.9990	4.9922	4.8819	4.5402	4.5698	5.0
9	5.0	5.0	4.9995	4.9955	4.9113	4.6257	4.7445	5.0
10	5.0	5.0	4.9998	4.9975	4.9333	4.6968	4.8529	5.0

5.2.3 Simulation results for cases with more than one sub-cell

A more practical situation will be one with two or more subcells with the footprint. To simplify the situation all subcells are assumed to be identical with attenuation being constant within each subcell.

Simulations were performed for these cases with excess brightness for each subcell assigned by a random number generator. Two cases were simulated:

- Excess brightness for each subcell generated using a uniform random number generator. The uniform random number is between 0 and T_{max} .
- An exponential random number generator is used to assign excess brightness temperatures for each subcell. The mean is set at some value T_{mean} which is typically 50 K. Care is taken that the excess brightness doesn't exceed 200 K.

Simulation results for the case with two sub-cells and uniform excess brightness temperature distribution are shown in Figures 5-2 through 5-4.

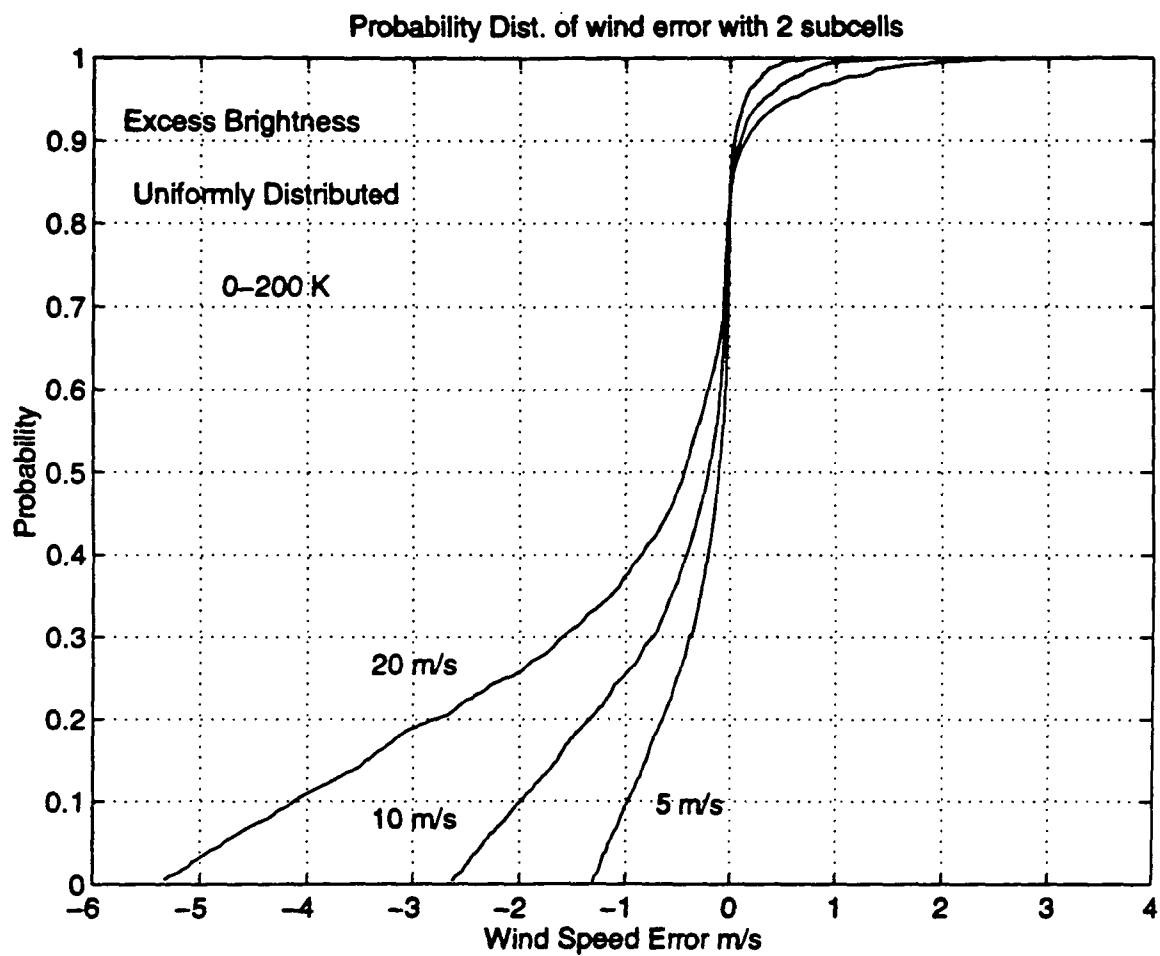


Figure 5-2: Probability Distribution of wind error. $T_{max} = 200$ K

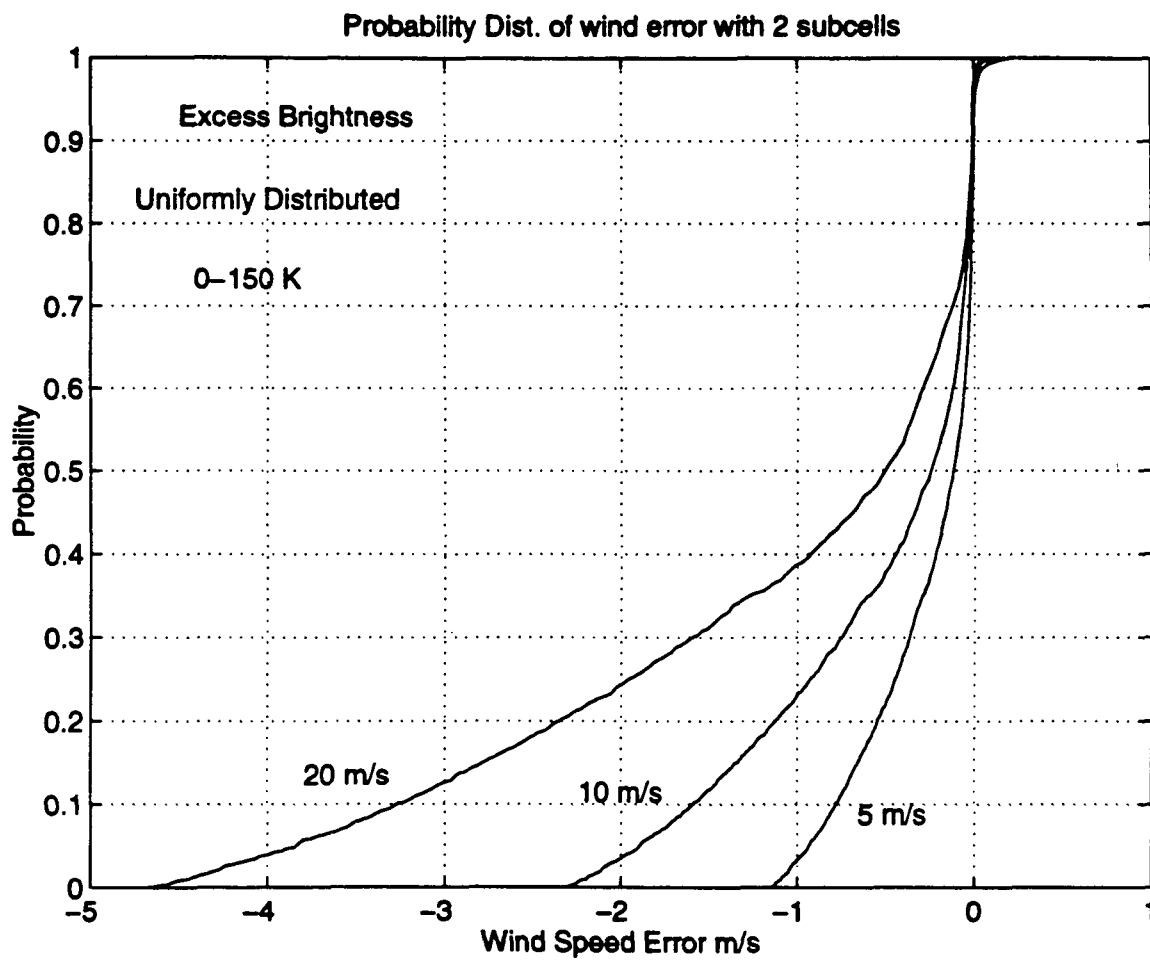


Figure 5-3: Probability Distribution of wind error. $T_{max} = 150$ K

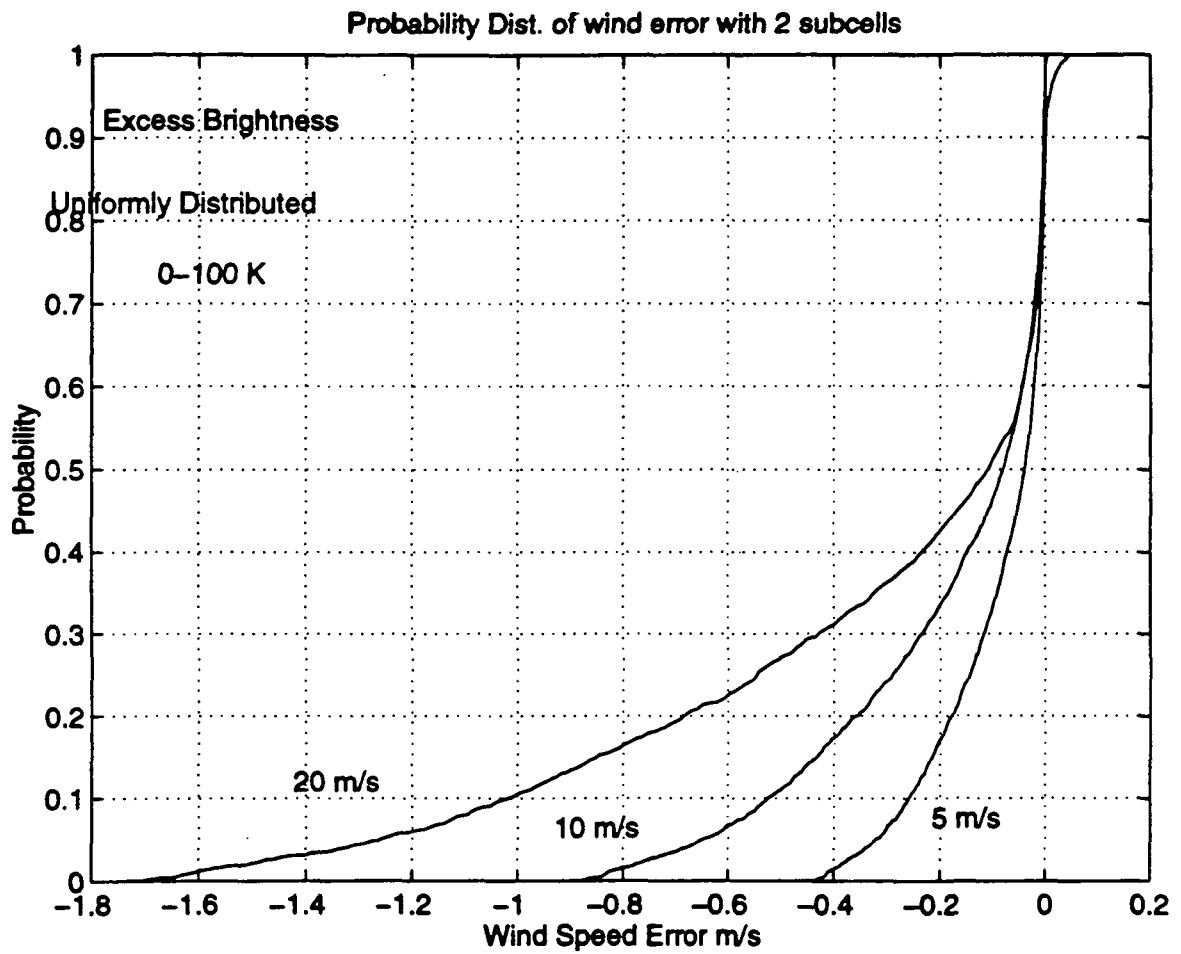


Figure 5-4: Probability Distribution of wind error. $T_{max} = 100$ K

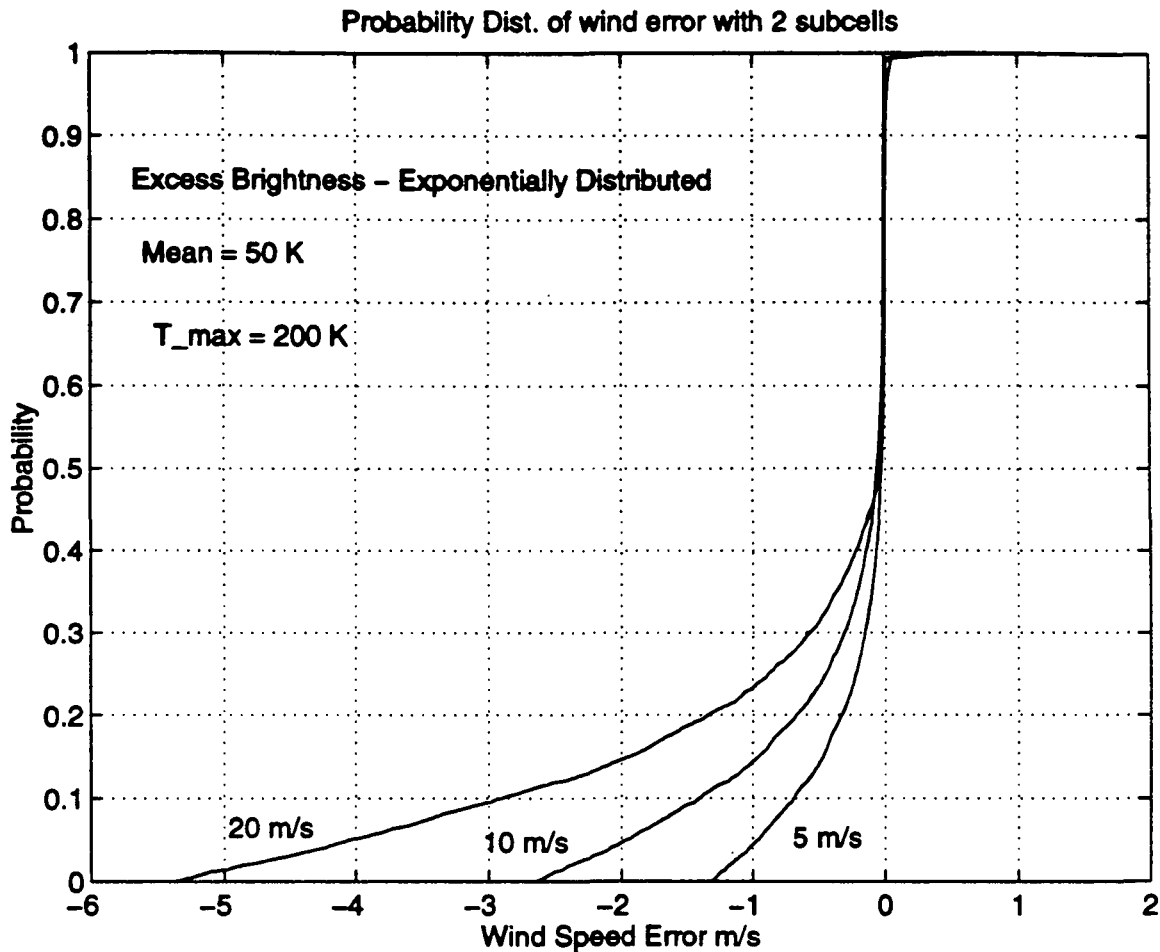


Figure 5-5: Probability Distribution of wind error. $T_{max} = 200$ K

Simulation results for the case with two sub-cells and exponential excess brightness temperature distribution are shown in Figures 5-5 through 5-7.

In all these cases the cumulative distribution functions show a steep rise in the region from -1 m/s to 0 m/s. This implies that most of the time the errors fall in this region. The higher values of error are for the cases where one of the sub-cell has a very low excess brightness and the other has a very high excess brightness temperature. Since the values of excess brightness for each sub-cell are picked using random number generators (uniform or exponential), cases with very low excess in one sub-cell and very high excess in the other are quite possible. For these cases the correction process doesn't improve the wind estimate a whole lot.

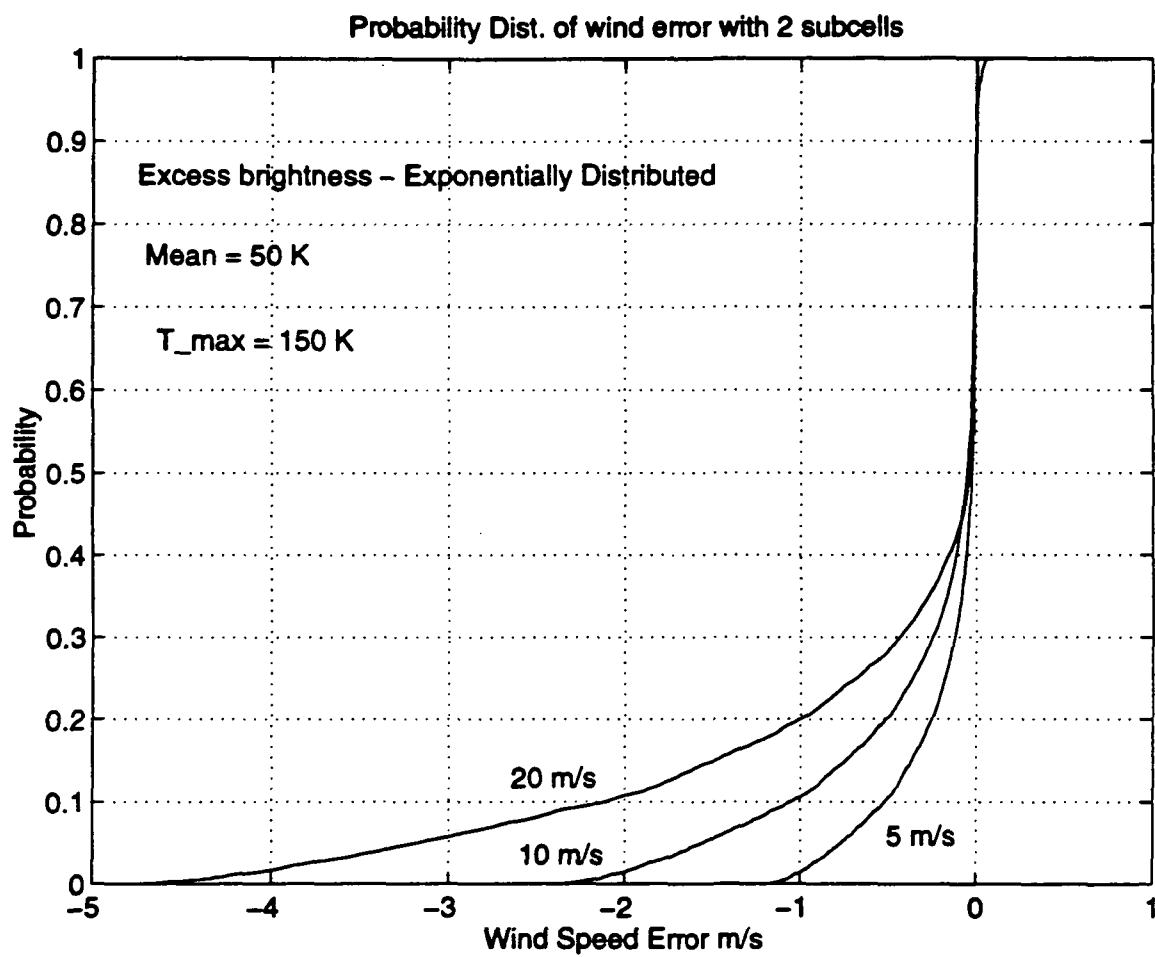


Figure 5-6: Probability Distribution of wind error. $T_{\text{max}} = 150 \text{ K}$

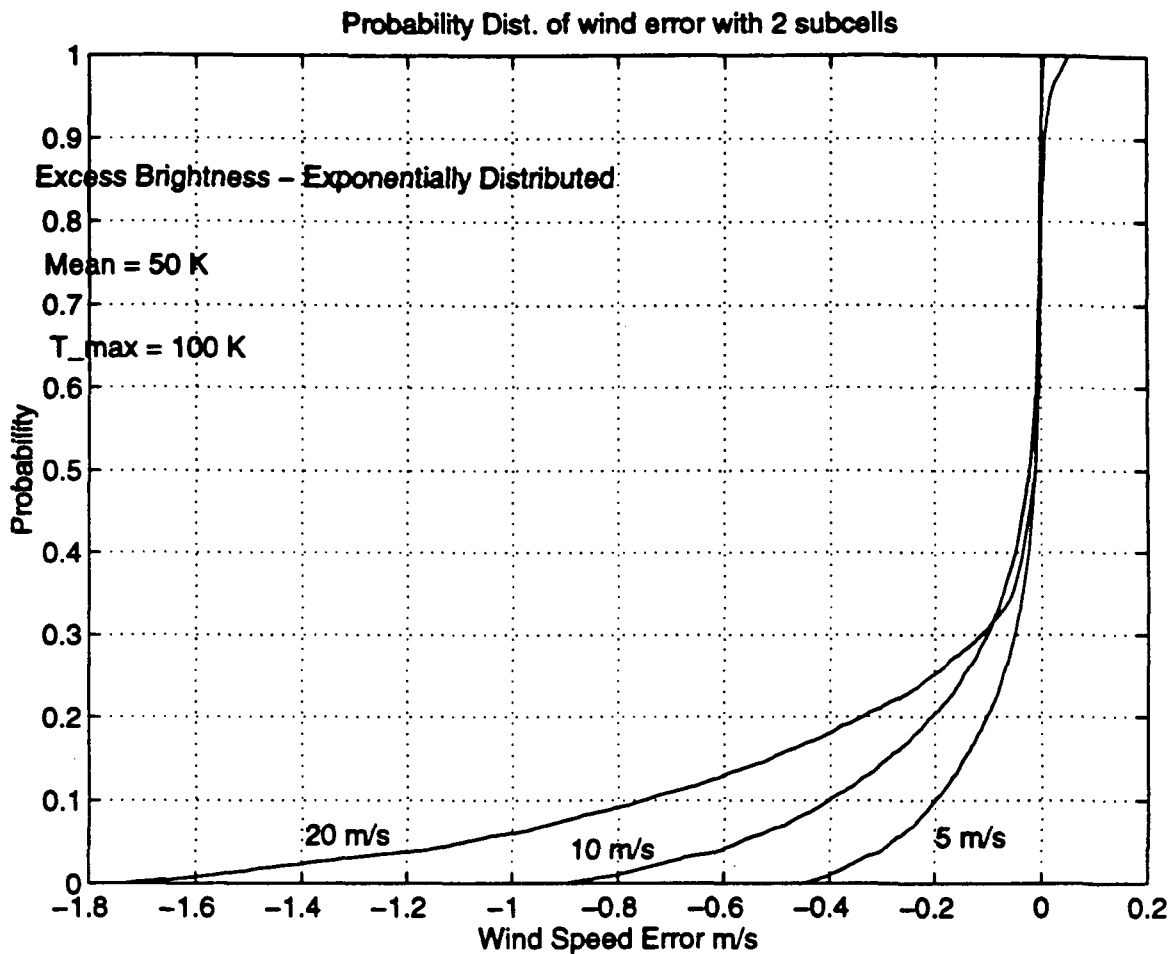


Figure 5-7: Probability Distribution of wind error. $T_{max} = 100$ K

These cases are impractical because a region next to a high storm region (high excess brightness) is always correlated to the high excess brightness and is seldom a very low excess brightness region.

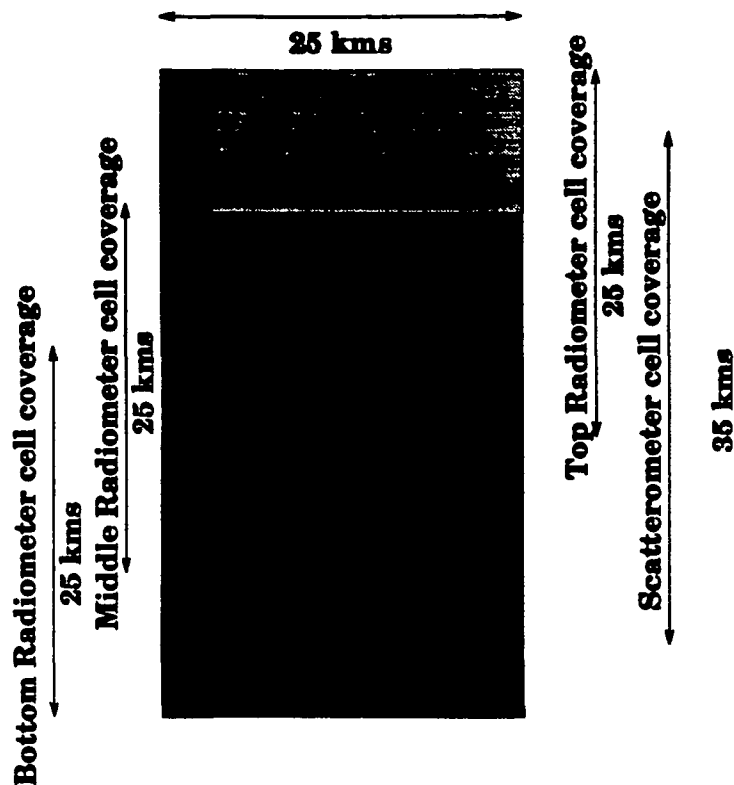
As the T_{max} of random number generator is reduced to a value as low as 100 K the wind errors are always less than 2 m/s. This is because the excess brightness temperatures in the two sub-cells are not too far apart.

5.2.4 Simulations with SeaWinds & AMSR footprints

Here we investigate the effects of attenuation on SeaWinds scatterometer measurements. For this study we consider 18.7 GHz AMSR radiometer cells that are not uniformly filled with rain and which correspond to a particular scatterometer cell.

We used a simple algorithm for correcting the errors in the scatterometer measurements using radiometer measurements. Our simulation shows the sensitivity of the radiometric corrections for the scatterometer to gradients in rainfall and cloud(hence attenuation). The following assumptions were made for this simulation:

- The scatterometer footprint(cell) is 35×25 km and the radiometer cell is 25×25 km approximately. For simplicity, the cells are assumed to be rectangular.
- The radiometer cells are subdivided into subcells of 1.0×1.0 km, each with a different attenuation(rainfall rate).
- The centers of the scatterometer and the radiometer may or may not coincide. The cases considered here are
 - Case (i) The scatterometer and radiometer centers coincide. Only radiometer cells in the along-track track direction are considered.
 - Case(ii) The scatterometer and radiometer centers are offset by 5 kms. Only radiometer cells in the along-track direction are considered.
 - Case (iii) The scatterometer and radiometer centers coincide but we consider radiometer cells in the cross-track direction.
- For the case where the center of the scatterometer cell is aligned with that of the radiometer, three radiometer cells are needed for correcting a single



- Area of overlap of 3 Radiometer cells
- Area covered by top Radiometer cell alone
- Area covered by bottom radiometer cell alone

Figure 5-8: Geometry for Cases (i)

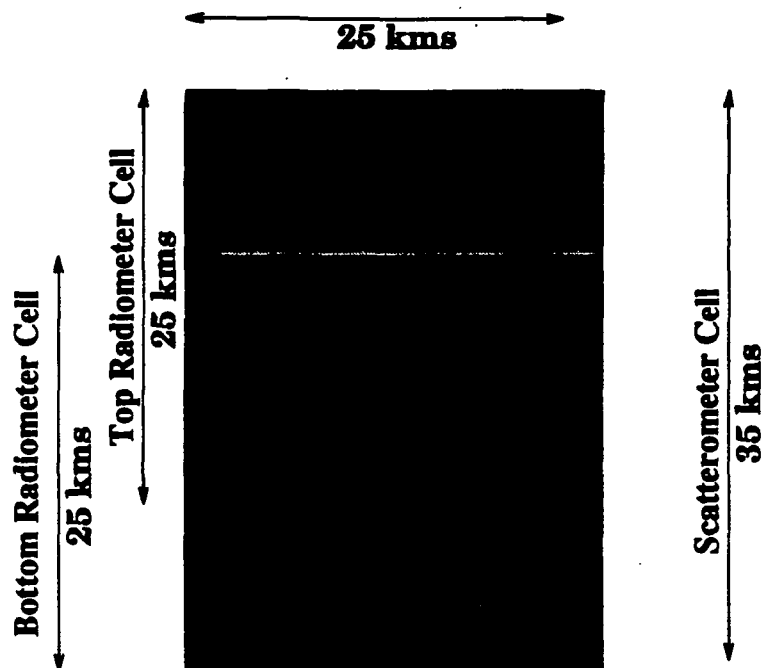
scatterometer cell. The radiometer and scatterometer cell structures for this case are shown in Figure 5-8.

- For the case where the centers of scatterometer & radiometer are offset by 5 kms only two radiometer cells are needed for correcting a single scatterometer cell. The radiometer and scatterometer cell structures for this case are shown in Figure 5-9.

The geometry of Case (iii) is shown in Figure 5-10.

To simplify the simulation further only the upwind case was considered.

The procedure used for the simulation is as follows



- **Overlap Area covered by both Radiometer Cells**
- **Area covered by top Radiometer Cell alone**
- **Area covered by bottom Radiometer Cell alone**

Figure 5-9: Geometry for Cases (ii)

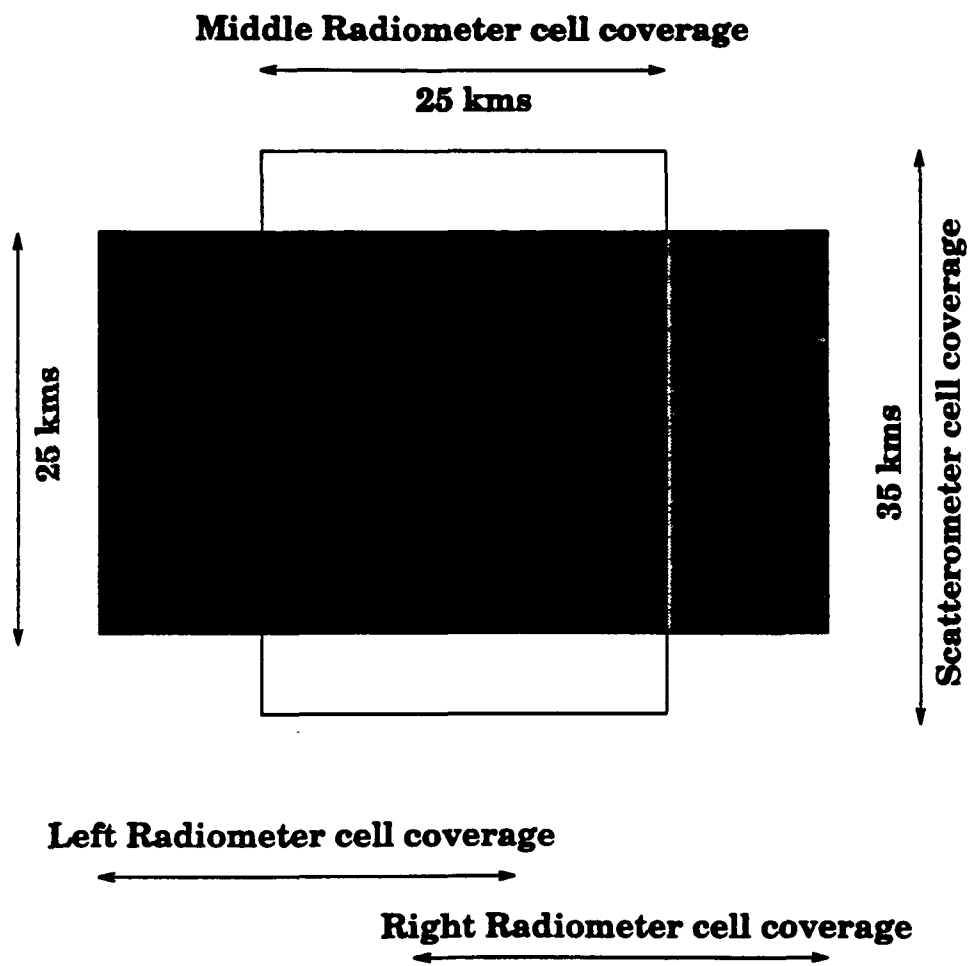


Figure 5-10: Geometry for Cases (iii)

- Select a scatterometer cell whose measurement of scattering coefficient is to be corrected and the radiometer cells associated with that scatterometer cell.
- The assignment of excess brightness temperatures for each of the radiometer subcells is by a seed-growing approach. Since the brightness temperatures of adjacent cells are correlated it is impractical to assume independent random brightness temperatures.
- The seed growing is implemented as follows:
 - Fix the number of seeds(storm centers) in the area of interest
 - Fix the co-ordinates of the seeds, the center of the radiometer and the scatterometer cells.
 - Assign random excess brightness temperature values between 80 & 200 K for the seeds.
 - Assume that brightness temperature falls off as $\exp^{-(r/r_0)^2}$ as we move away from the seeds. The rate of fall (set by r_0) can be fixed at any desired value. Here r is the distance to the seed from the point of interest.
 - Scanning the area of interest from left to right and top to bottom, the distance of each radiometer subcell to each of the seeds is calculated. It is highly probable that a storm which is nearest to a subcell will have greater influence on its brightness temperature than the one which is farther away. Based on this assumption the seed which is nearest to a subcell is selected. With the knowledge of brightness temperature of the nearest seed, the distance to the seed and the rate of fall the brightness temperatures for all the subcells are assigned.

Figures 5-11 through 5-14 show typical excess brightness temperature assignments for the radiometer subcells with two storms and $r_0 = 10$.

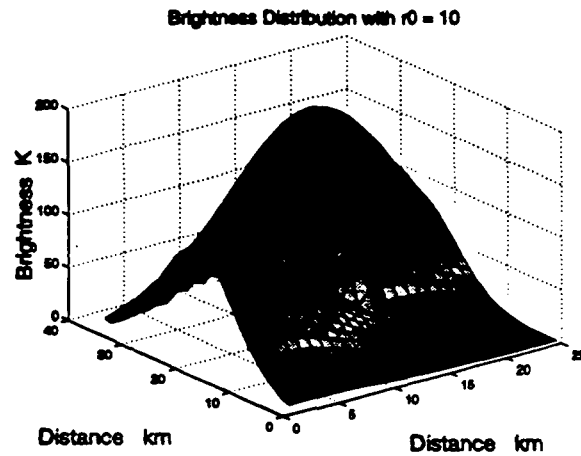


Figure 5-11: Typical brightness temperature assignment, $r_0 = 10$

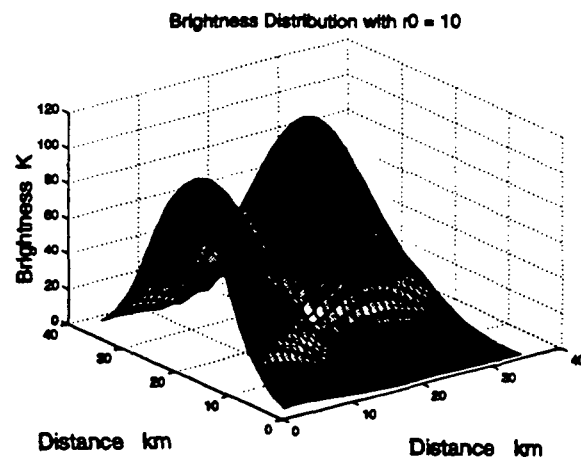


Figure 5-12: Typical brightness temperature assignment, $r_0 = 10$

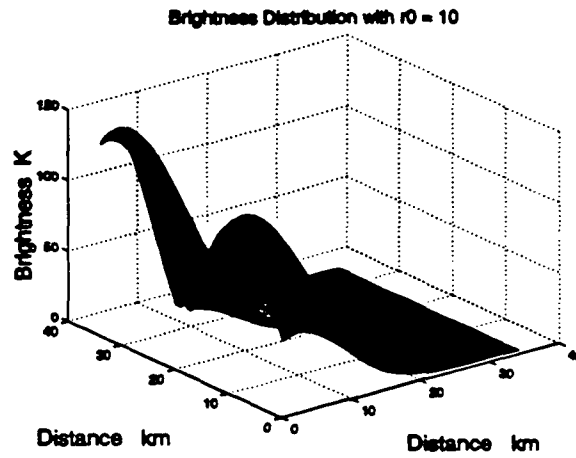


Figure 5-13: Typical brightness temperature assignment, $r_0 = 10$

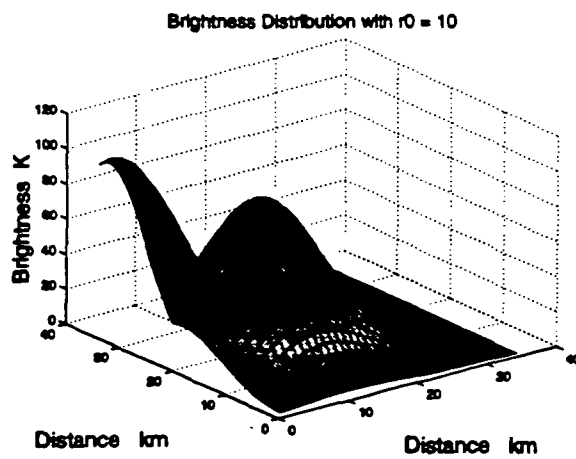


Figure 5-14: Typical brightness temperature assignment, $r_0 = 10$

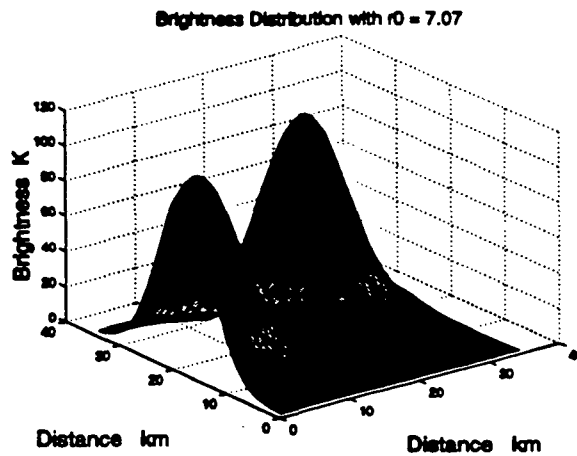


Figure 5-15: Typical brightness temperature assignment, $r_0 = 7.07$

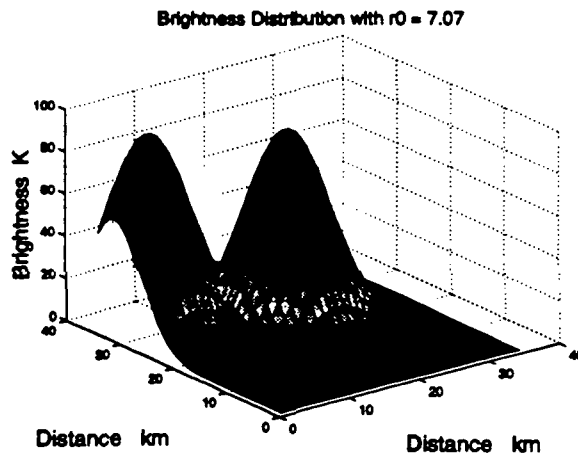


Figure 5-16: Typical brightness temperature assignment, $r_0 = 7.07$

Figures 5-15 through 5-17 show typical excess brightness temperature assignments for the radiometer subcells with two storms and $r_0 = 7.07$.

Figures 5-18 through 5-20 show typical excess brightness temperature assignments for the radiometer subcells with two storms and $r_0 = 4.47$.

The values of r_0 chosen for these simulations are consistent with rain-cell sizes encountered in real life. Values of r_0 in the range 2-3 are more practical [38].

The radiometer measures the average brightness temperature in a radiometer cell. The average brightness temperature is calculated using an area weighted average of the brightness temperatures in the subcells of the radiometer.

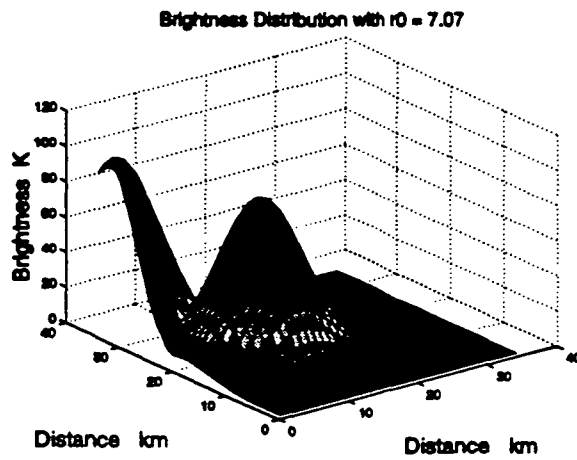


Figure 5-17: Typical brightness temperature assignment, $r_0 = 7.07$

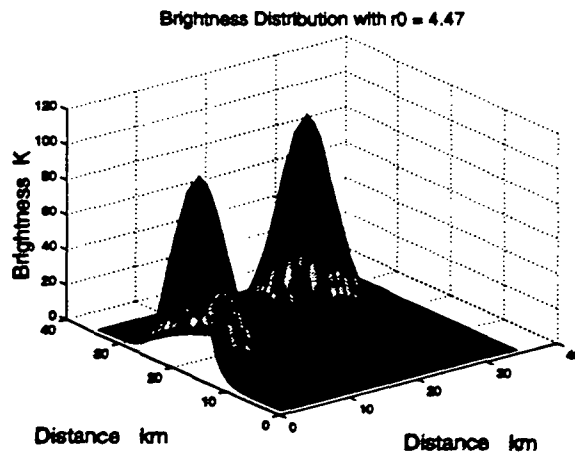


Figure 5-18: Typical brightness temperature assignment, $r_0 = 4.47$

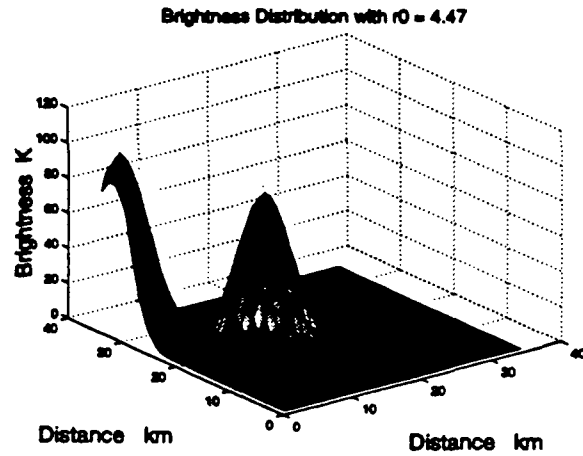


Figure 5-19: Typical brightness temperature assignment, $r_0 = 4.47$

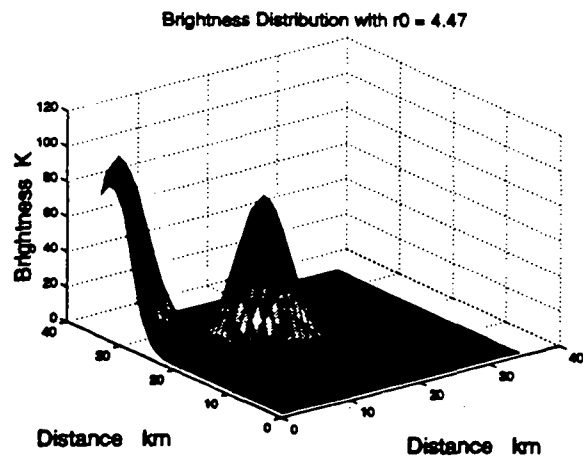


Figure 5-20: Typical brightness temperature assignment, $r_0 = 4.47$

Once excess brightness for each subcell is known, the procedure for radiometric correction is the same as that for the simple cases discussed above. The difference is that the radiometer and scatterometer footprints are not identical and two or more radiometer cells are used for correcting a single scatterometer cell.

Using the seed-growing approach excess brightness $TB_{subcell}(x, y)$ for each subcell (x, y) is obtained. Using excess brightness temperature in each subcell, the attenuation corresponding to each subcell is calculated using the cubic relation. After suitable frequency scaling attenuation at scatterometer frequency (13.4 GHz) and radiometer frequency (18.7 GHz). The apparent temperature measured by the radiometer and the backscatter coefficient (σ^0) are computed after taking into account the attenuation in the area of interest.

Apparent temperature of each subcell is

$$TB_{apparent_subcell}(x, y) = TB_{subcell}(x, y) + TB_{wind} \times \exp(-\alpha_{rad}(x, y)) \quad (5.21)$$

where

$$TB_{wind} = 82 + 1.06 \times u$$

u is the surface wind speed

$\alpha_{rad}(x, y)$ is attenuation in subcell (x, y) at radiometer frequency

The apparent temperature measured by each radiometer cell is the average of apparent temperatures (since all subcells are assumed to be identical) of all the subcells which fall in their domain.

$$TB_{avg_apparent} = \frac{\sum_{i=1}^M \sum_{j=1}^N TB_{apparent}(sub_cell)}{M \times N} \quad (5.22)$$

where

M and N are number of subcells in x and y directions in a radiometer cell.
Measured scattering coefficient for each scatterometer sub-cell is

$$\sigma_{measured}^{o}(sub_cell) = \sigma^o \times \exp(-2 \times \alpha_{scat}(x, y)) \quad (5.23)$$

where

σ^o is ideal backscatter that would be measured in the absence of attenuation
 $\alpha_{scat}(x, y)$ is attenuation in subcell (x, y) at radiometer frequency

The σ^o actually measured by the scatterometer is

$$\sigma_{measured}^o = \frac{\sum_{i=1}^M \sum_{j=1}^N \sigma_{measured}^{o}(sub_cell)}{M \times N} \quad (5.24)$$

where

M and N are number of subcells in x and y directions

The above procedure was repeated for different values of brightness temperatures for the seeds and the resulting wind errors were calculated.

Using u_{bias} as initial wind estimate and measured apparent temperature and backscattering coefficient as inputs the correction process is set rolling in an iterative fashion until there is not much improvement in wind speed estimate.

The following steps are involved in the iterative process

- An initial estimate (guess) of surface wind speed is made
- Assuming a calm surface and neglecting the wind speed effects leads to errors in the attenuation estimates. Increasing wind speed leads to increasing surface roughness, generation of foam, and then to larger patches of foam coverage. These changes in the composition of the sea surface can be characterized as an increase in surface emissivity. To reduce the errors in the

attenuation estimate, the sea surface can be described for a 10 m/s wind speed instead of assuming a calm sea surface.

- Brightness contribution from the sea surface is calculated for this wind estimate (u_{bias}).

$$TB_{bias} = 82 + 1.06 \times u_{bias} \quad (5.25)$$

- The excess brightness temperature is calculated by subtracting the contribution of the surface from the total apparent temperature measured by the radiometer.

$$TB_{est,s} = TB_{avg_{apparent}} - TB_{bias} \quad (5.26)$$

- Attenuations at radiometer and scatterometer frequencies are estimated using $TB_{est,s}$ after frequency scaling.
- The measured σ^o is corrected for attenuation suffered using attenuation estimate α_{13_est} (in Nepers).

$$\sigma^o_{corrected} = \sigma^o_{measured} \times \exp(2 \times \alpha_{13_est}) \quad (5.27)$$

- Surface wind speed can be estimated from corrected sigma by inverting the SASS model function.

$$u_{est} = 10^{\frac{\sigma_{measured} - 10G}{10H}} \quad (5.28)$$

- The wind speed error is the difference between the u_{est} and the true wind speed u .

$$u_{error} = u_{est} - u \quad (5.29)$$

- Using the u_{est} as the new wind bias u_{bias} , the surface contribution is calculated

$$TB_{bias} = (82 + 1.06 \times u_{est}) \times \exp(-\alpha_{18_{est}}) \quad (5.30)$$

where

$\exp(-\alpha_{18_{est}})$ accounts for the loss to the surface contribution.

- Using this new surface contribution the excess brightness temperature is calculated. An attenuation estimate corresponding to this new value of excess is made and this new attenuation estimate is used to correct the measured sigma to again get an estimate of wind speed. This iterative procedure is continued until there is no appreciable improvement in wind speed estimation.

When the attenuation seen by the scatterometer cell is drastically different from those seen by the radiometer cells, large wind errors occur, but these are fairly rare.

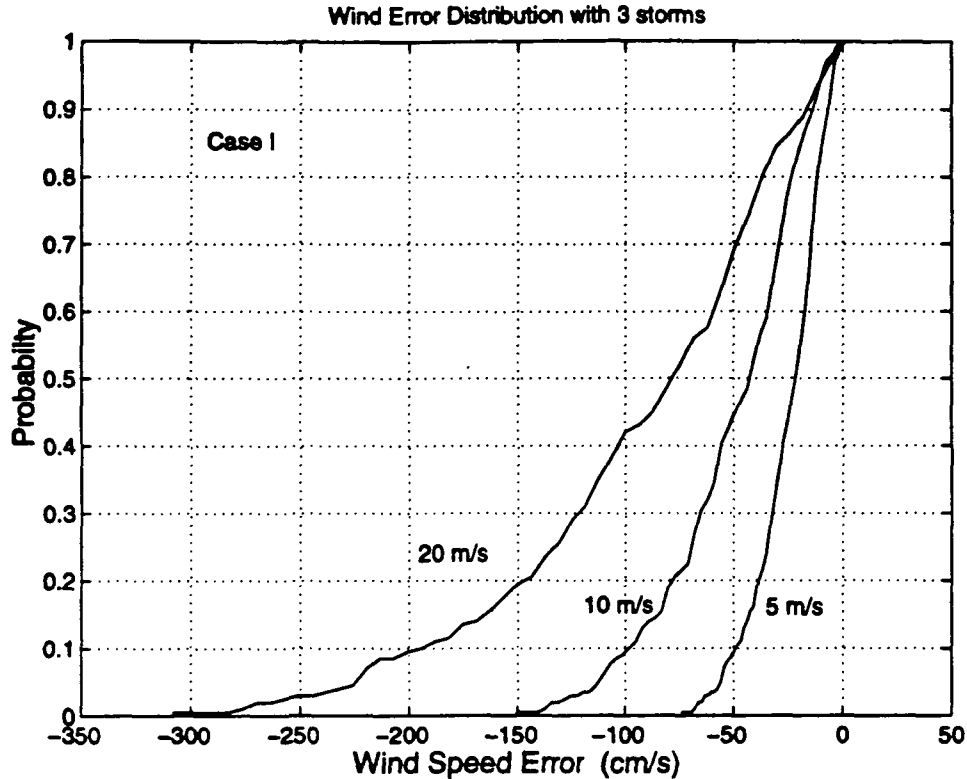


Figure 5-21: Probability distribution of wind error for Case I, $\tau_o = 10$

The distribution functions for wind error for the Case I are shown in Figures 5-21 through 5-23 for $\tau_o = 10, 7.07$ and 4.47 respectively. As can be seen from the simulation results, the errors are high when the τ_o value is high. A high τ_o value implies a slow decay of the excess brightness temperature (hence attenuation) from the initial seed value. High τ_o results in the whole area of interest having a high attenuation, which hinders the correction process. These cases of high attenuation through the scatterometer footprint are generally ignored because the scatterometer measurement do not make sense. Correcting such cases is not required.

The distribution functions for wind error for Case II are shown in Figures 5-24 through 5-26 for $\tau_o = 10, 7.07$ and 4.47 respectively.

The simulations results for Case II are not much different from Case I. This is because in both cases scatterometer and radiometer footprints look at almost the

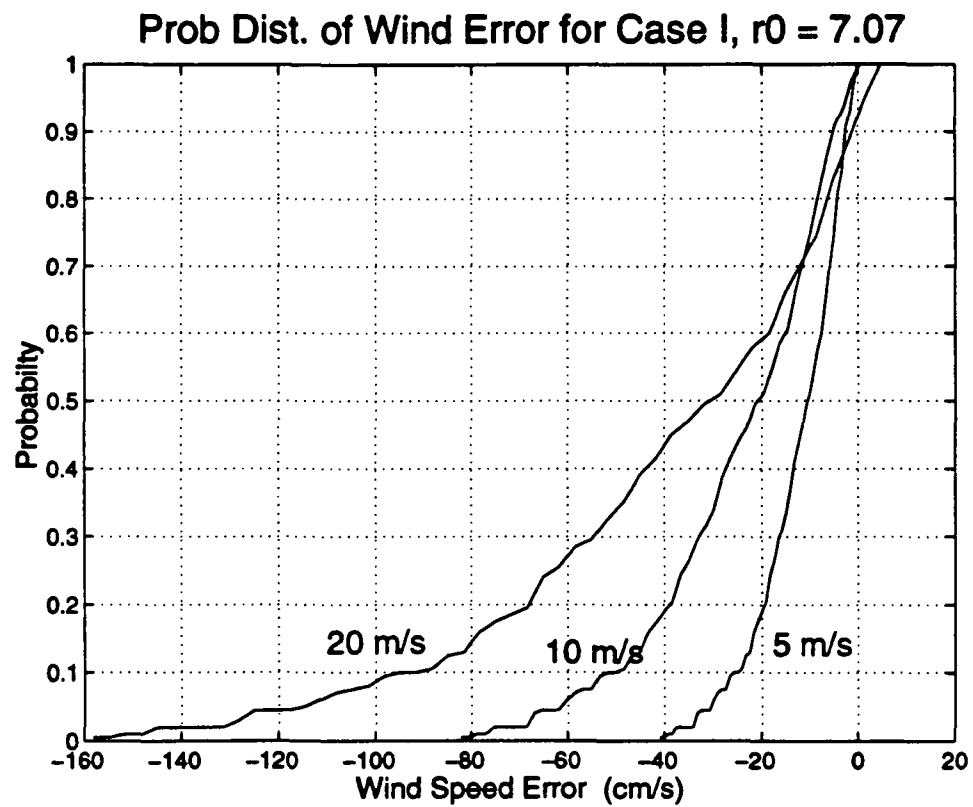


Figure 5-22: Probability distribution of wind error for Case I, $r_0 = 7.07$

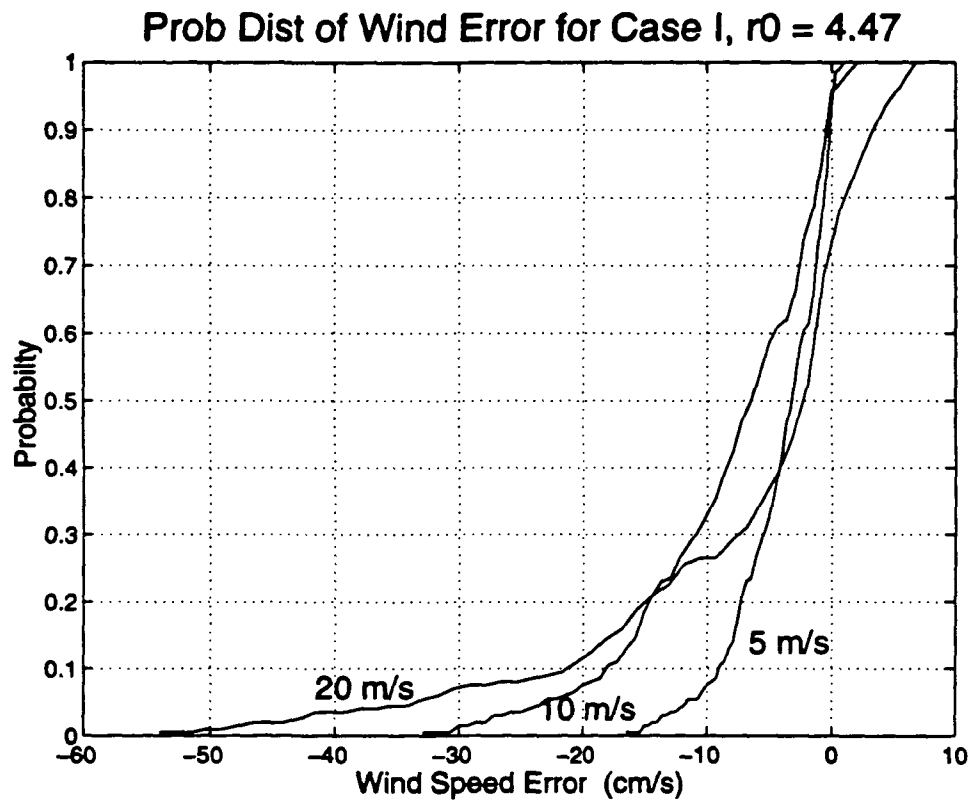


Figure 5-23: Probability distribution of wind error for Case I, $r_0 = 4.47$

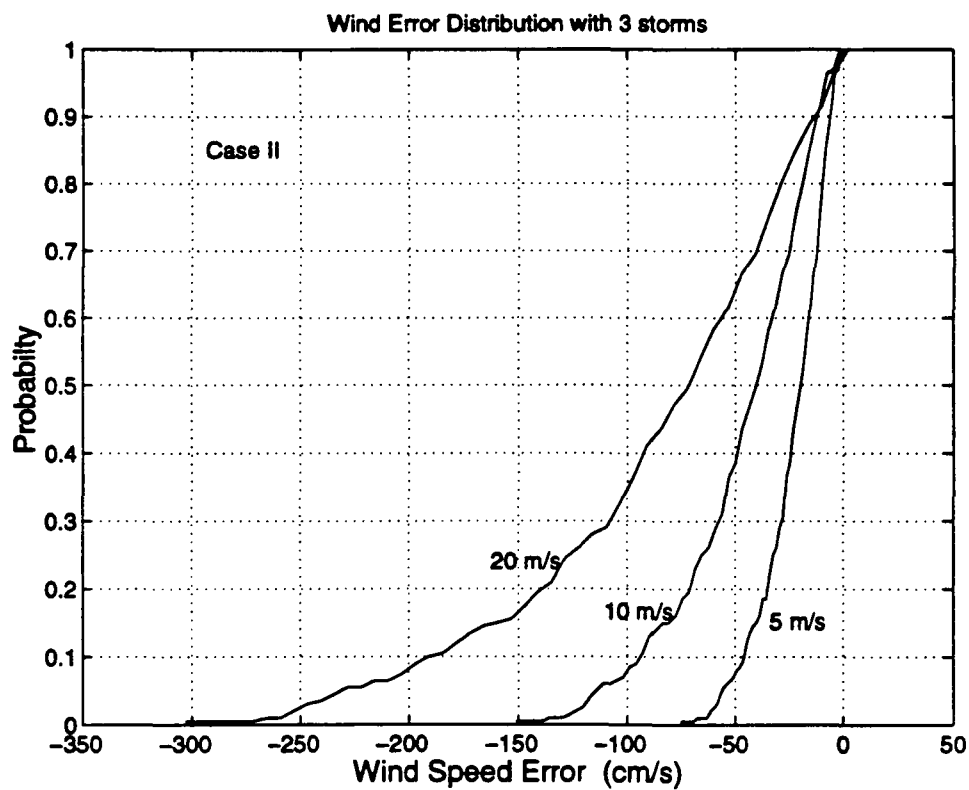


Figure 5-24: Probability distribution of wind error for Case II, $r_o = 10$

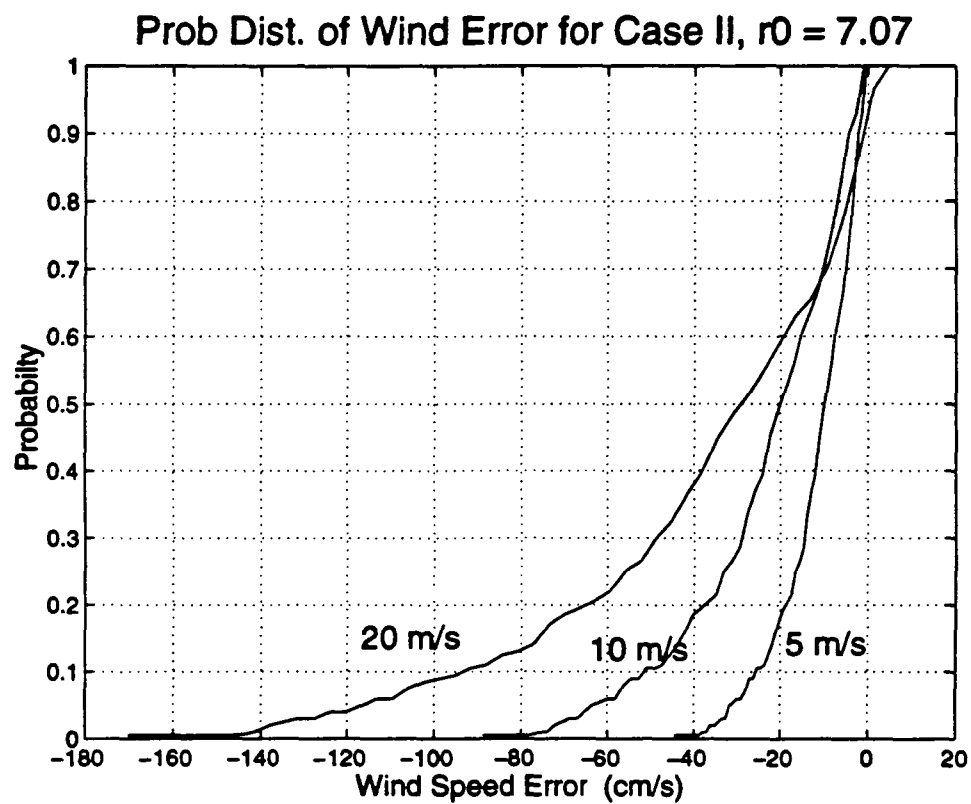


Figure 5-25: Probability distribution of wind error for Case II, $r_0 = 7.07$

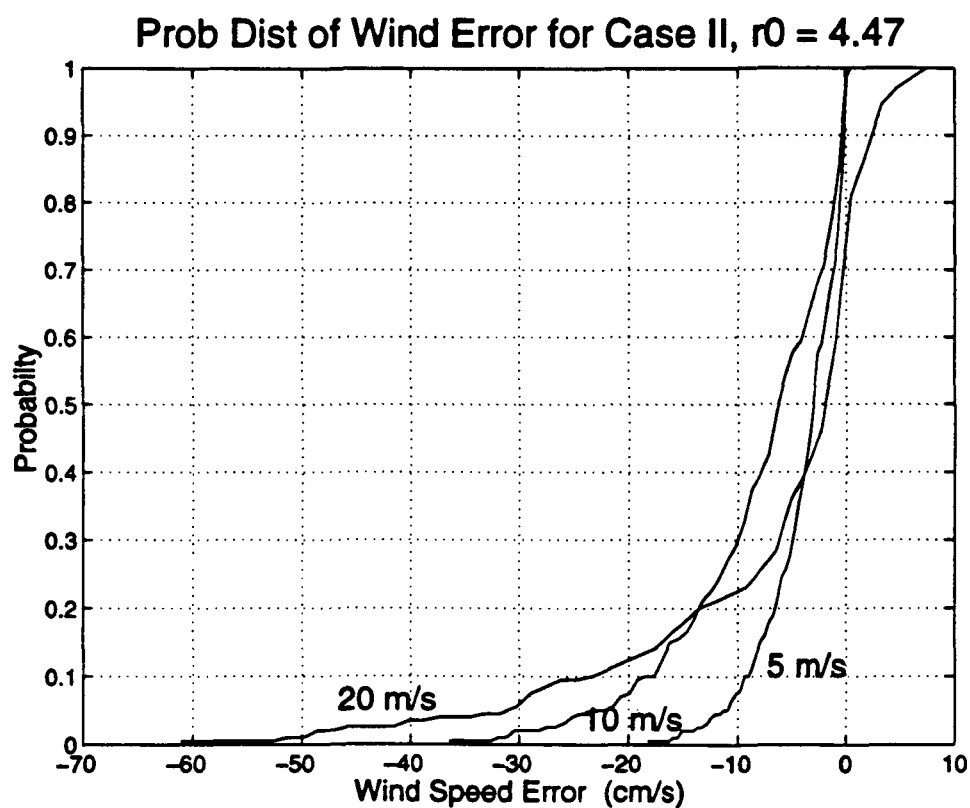


Figure 5-26: Probability distribution of wind error for Case II, $r_o = 4.47$

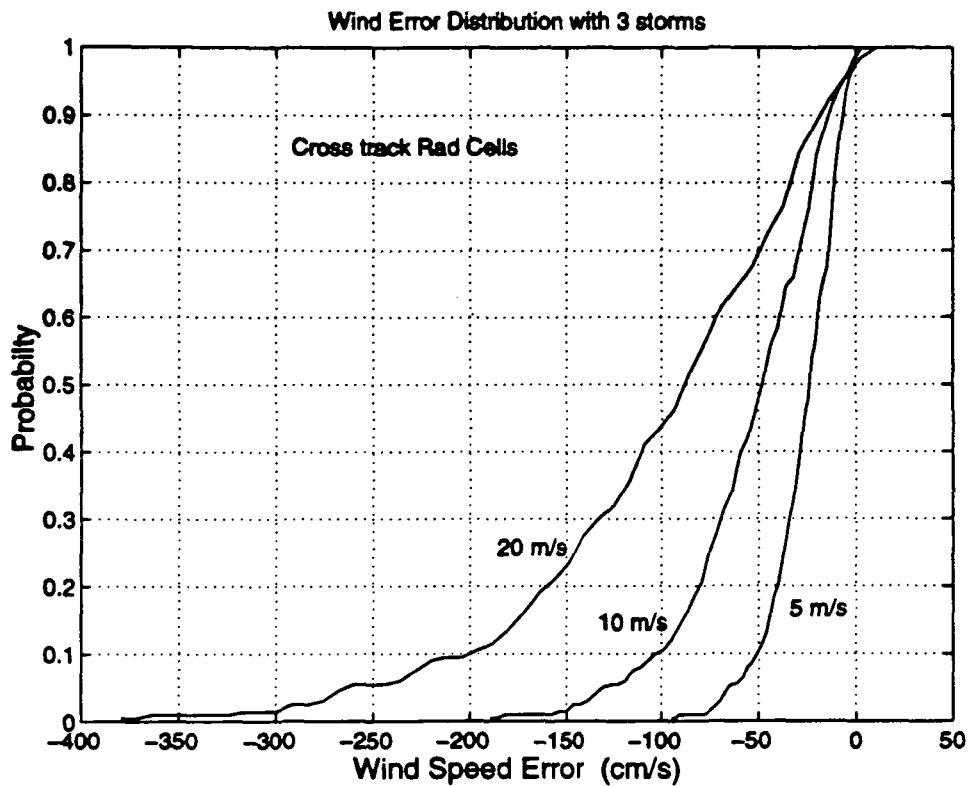


Figure 5-27: Probability distribution of wind error for Case III, $\tau_o = 10$

same area. In Case I the radiometer footprints cover areas which are not in the scatterometer footprint. This tends to increase the errors in wind estimate.

This problem is amplified in Case III which uses radiometer footprints in the across-track direction. Here the radiometer footprints cover a large area which is outside the scatterometer footprint. Logically, one would expect Case III to have larger errors in wind estimate compared to Case I and Case II. The simulation results for Case III are shown in Figures 5-27 through 5-29. The results are consistent with our expectations, but most errors are still small.

Considering the centers of radiometer and scatterometer and radiometer footprints coincide and taking 10 km sampling in the along track direction and cross track direction into account, there are 9 radiometer centers which fall within the scatterometer footprint. The geometry for this case is shown in Figure 5-30. Considering all 9 radiometer cells for correction of a single scatterometer cell sim-

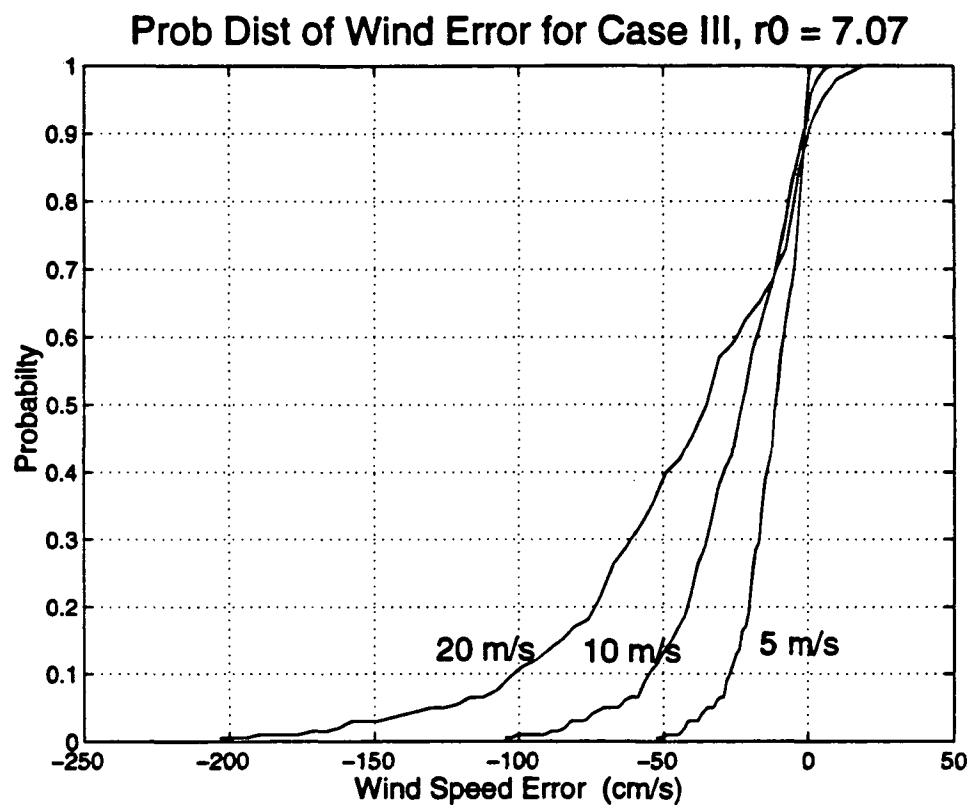


Figure 5-28: Probability distribution of wind error for Case III, $\tau_o = 7.07$

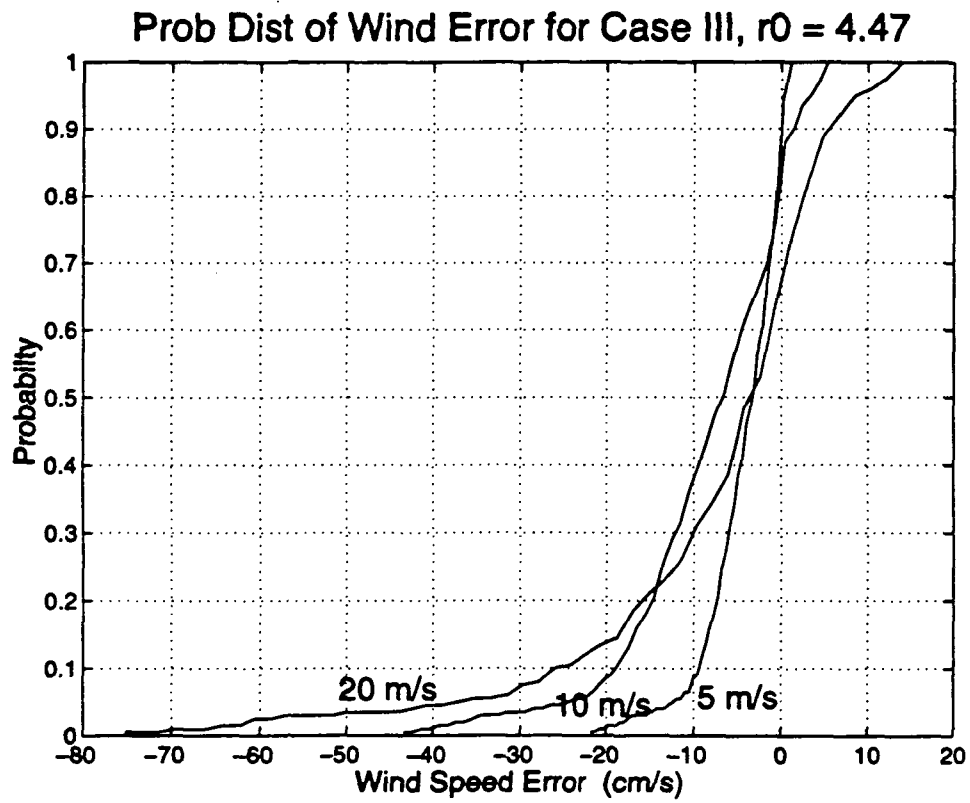
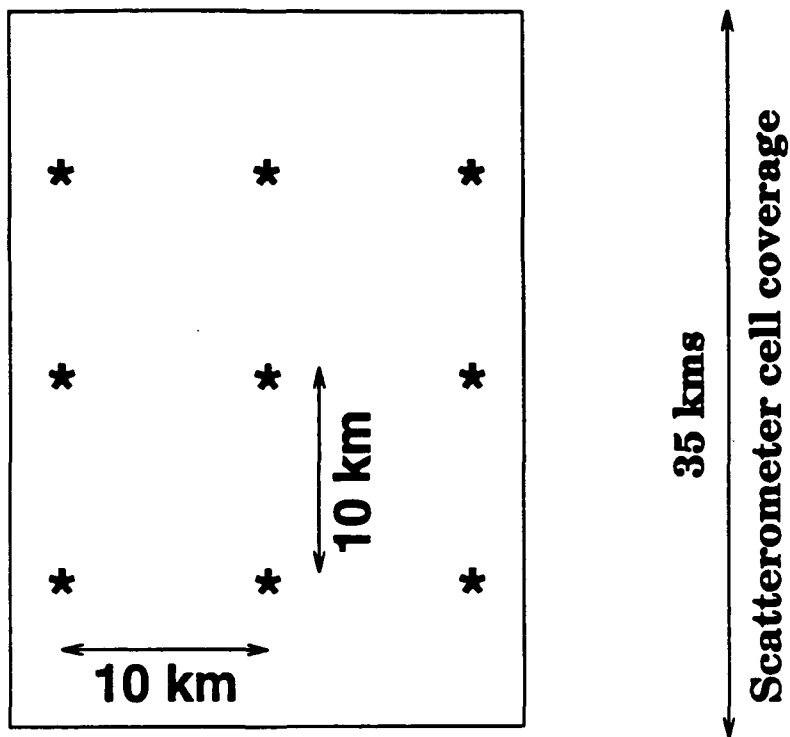


Figure 5-29: Probability distribution of wind error for Case III, $r_0 = 4.47$



* Center of Radiometer cell

Figure 5-30: All radiometer cells with centers inside scatterometer cell

ulations were performed. The results are shown in Figure 5-31. The wind speed errors are slightly bigger than those for Case I and Case II. The high values of wind errors are not common and they occur with a very low probability (typically 0.01).

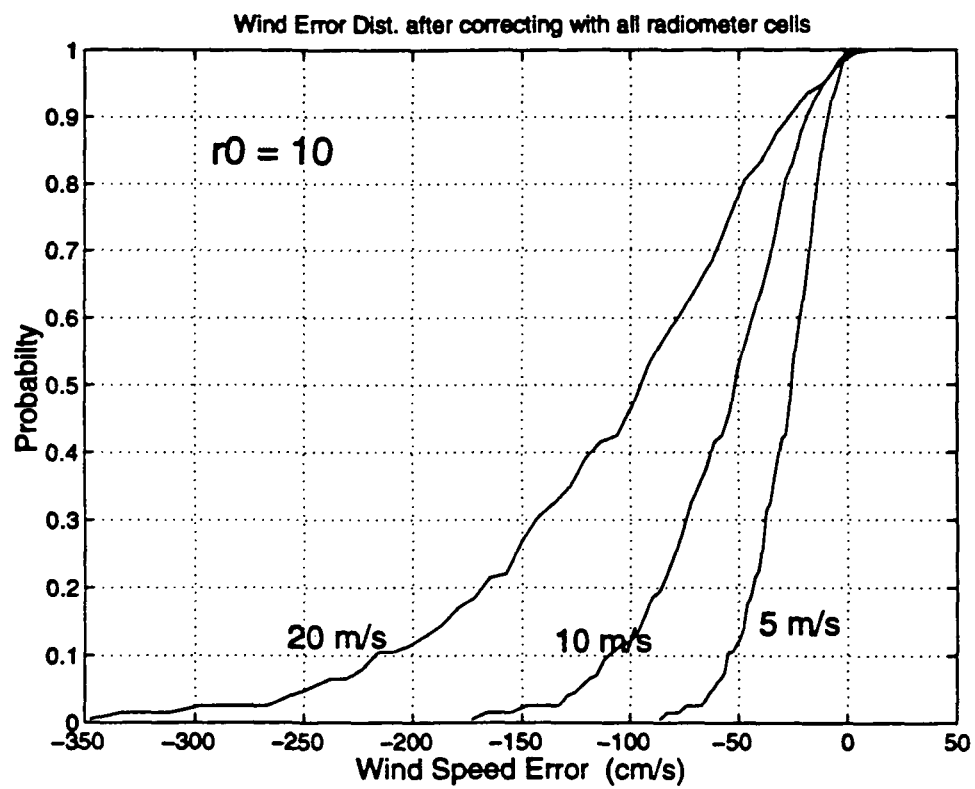


Figure 5-31: Wind error Distribution when all radiometer cells are used for correction, $r_0 = 10$

Chapter 6

Conclusions And Future Research Recommendations

6.1 Conclusion

The wind speed errors calculated using the footprint dimensions of the SeaWinds scatterometer and AMSR 18.7 radiometer are small in most cases. The small errors are a result of using a radiometer footprint smaller than the scatterometer footprint. Another significant factor for the small errors is the assumption that the scan patterns of the active and passive systems are nearly the same. Rectangular footprints were used to illustrate the nature of the problem of correcting a large scatterometer cell with two or more radiometer cells. In a practical situation the footprints are not rectangular, the scan patterns might not be the same and the rainfall contours are much more complex. Even though the problem becomes more complex, the general procedure of error correction is the same as that for the simple cases discussed here.

Simulations performed with simple cases where scatterometer and the radiometer footprints are identical show that the iterative correction process works. The

simulations with more than one sub-cell illustrate the problems with correcting partially filled cells. Correction for uniformly filled cells is more effective than the correction for partially filled situation.

With different foot-print sizes the correction process degrades one more step. When the scatterometer and radiometer footprints are different, the conditions in the scatterometer are different from that of the radiometer footprint. How different the conditions are depends on the relative position of the centers of the two foot-prints and also on the fraction of the radiometer cell which overlaps the scatterometer cell. Even if the whole of the radiometer cell falls within the scatterometer cell since the scatterometer cell is bigger than the radiometer cell the conditions outside the radiometer cell might be drastically different from that in the area common to the radiometer and scatterometer footprints. In these cases the correction using the radiometer cell is not very effective. Using more than one radiometer cell to correct a single scatterometer cell helps, but again using more radiometer cells results in the radiometer measurements from regions outside the scatterometer footprint also.

Since the exact scan patterns of the radiometer and scatterometer are not known different cases arise based on the relative position of the centers of the two footprints. Simulations were performed for four different cases. The results from the four cases are almost the same which shows that the correction procedure is effective even when the scan patterns are offset by 5 km.

The simulation of cloud and rain conditions by the seed-growing approach may not be the exact situation one would encounter. Only three storms were considered in a 45×45 km area. In reality more than three storms of diameter 5 km can be found in a 45×45 km region. Use of a three dimensional cloud and rain would be more appropriate and accurate.

Rectangular footprints were used in all the simulations. In reality the footprints are elliptical. Results will not vary much if elliptical footprints are used.

With elliptical footprints the subcells can still be rectangular but of a smaller dimension (0.1×0.1 km). With smaller rectangular subcells the footprints are close to elliptical (a bit irregular though).

For these simulations we have assumed that the true wind direction is known. This might not be the case in practice. The surface temperature is assumed to be constant over area of interest. Variation in surface temperature over dimensions of interest (25×25 km) are quite common. This surface temperature variation must be incorporated in the correction algorithm. The surface temperature variation affects the calculation of surface contribution and also the cubic relation. The empirical relation between excess brightness temperature and attenuation is surface temperature dependent and the accuracy of the attenuation estimate is dependent on accurate knowledge of surface temperature.

Errors in wind estimate are possible due to inaccurate models. There is still scope for improvement in developing scatterometer model functions. Errors due to instrument noise have not been considered in this simulations. In practice errors due to noise and scatterometer model function uncertainty will probably exceed attenuation errors.

6.2 Future Research Recommendations

Some suggestions for future research in this direction are as follows

- Better models for clouds and rain
- Further understanding of relation between attenuation and excess brightness temperatures
- Study of the rain-cell patterns and their seasonal variability
- Change in NRCS due to impact of the rain drops on the ocean surface
- Incorporate the surface temperature variations in the algorithm

- Judicial selection of radiometer cells used for correction to avoid large errors in wind estimate
- Find ways of using all radiometer cells which fall within scatterometer cell but with unequal weighting

Bibliography

- [1] R. Atlas, *et al.*, Global surface wind and flux fields from model assimilation of Seasat data. *J. Geophys. Res.*, vol. 92, pp 6477-6487, 1987
- [2] W.J. Pierson, Examples of, reasons for, and consequences of poor quality of wind data from ships for marine boundary layer: Implications for remote sensing, *J. Geophys. Res.*, vol. 95, pp. 13,313 - 13,340, 1990.
- [3] F.M. Naderi, M.H. Freilich, D.G. Long, Spaceborne radar measurements of wind velocity over the ocean - An overview of the NSCAT scatterometer system, *Proceedings of the IEEE*, vol. 79, No. 6, pp. 850-866, 1991.
- [4] R.K. Moore and F.T. Ulaby, The radar radiometer, *Proc. IEEE*, vol. 57, no. 4, pp. 587-590, April 1969.
- [5] R.K. Moore and W.J. Pierson, Surface weather and wave conditions *Proc. Joint Oceanographic Assembly, (Tokyo, Japan)*, Sept. 13-25, 1970.
- [6] R.K. Moore and A.K. Fung, Radar determination of winds at sea, *Proc. IEEE*, vol. 67, no. 11, pp. 1504-1521, Nov. 1979.
- [7] L.C. Scroeder, *et al.*, The relationship between wind vector and normalized radar cross-section used to derive Seasat-A satellite scatterometer winds, *J. Geophys. Res.*, vol. 87, pp. 3318-3386.
- [8] F. J. Wentz, S. Petcherych, L.A. Thomas, A model function for ocean radar cross sections at 14.6 GHz, *J. Geophys. Res.*, vol. 89, pp. 3689-3704, 1984.

- [9] F. J. Wentz, L.A. Mattox, S. Peteherych, New Algorithms for microwave measurements of ocean winds: Applications to SEASAT and Special Sensor microwave imager, *J. Geophys. Res.*, vol. 91, pp. 2289-2307, 1986.
- [10] W.L. Jones, L.C. Schoeder, J.L. Mitchell, Aircraft Measurements of the microwave scattering signature of the ocean *IEEE. J. Oceanic Eng.*, vol. OE-2, pp. 52-61, 1977.
- [11] D.G. Long, J.M. Mendel, Identifiability in wind estimation from scatterometer measurements, *IEEE trans. Geosci. Remote Sensing*, vol. 29, pp. 268-276, Mar. 1991.
- [12] W.J. Pierson, A monte Carlo comparison of the recovery of winds near upwind and downwind from the SASS-1 model function by means of the sum of squares algorithm and a maximum likelihood estimator, NASA Contractor Rep. 3839, 1984.
- [13] R.H. Stewart, *Methods of Satellite Oceanography*, Univ. of Calif. Press, San Diego, CA, 360 pp. 1985.
- [14] Michael H. Freilich, David G. Long, Michael W. Spencer, SeaWinds: A Scanning Scatterometer for ADEOS-II - Science Overview *Proc. IEEE*, pp. 960-963, 1994.
- [15] A. Stogryn, Effect of Scattering by Precipitation on Apparent Sky Temperature in the Microwave Region, Space General Corporation, Report SGC 613 TM-1, El Monte, California, 1964.
- [16] David K. Barton, *Radars. Vol. 2 - The Radar Equation*, Artech House Inc., pp. 219-220, 1974.
- [17] F.T. Ulaby, R.K. Moore, A.K. Fung, *Microwave Remote Sensing*, vol. I, Addison-Wesley Publishing Company, Reading, Massachusetts, 1981.

- [18] G. Mie, Beitrage zur Optik truber medien, speziell Kolloidaler metalasungen, *Ann. Physik* vol. 25, p. 377, 1908.
- [19] K.S. Fraser, N.E. Gaut, E.C. Reifenstein, H. Sievering, Interaction Mechanisms - Within the Atmosphere, *Manual of Remote Sensing*, R.G. Reeves, ed., American Society of Photogrammetry, Falls Church, Virginia, Chapter 5, 1975.
- [20] J.W. Ryde, D. Ryde, *Attenuation of Centimeter Waves by Rain, Hail, Fog and Clouds*, General Electric Co., Wembley, England, 1945.
- [21] K.L.S. Gunn, T.W.R. East, The Microwave Properties of Precipitation Particles, *Quart. J. Royal Meteorol. Soc.*, 80, pp. 522-545, 1954.
- [22] A. Benoit, Signal Attenuation Due to Neutral Oxygen and Water Vapor, Rain and Clouds, *Microwave J.*, 11, pp. 73-80, 1968.
- [23] R.G. Medhurst, Rainfall Attenuation of Centimeter Waves: Comparison of Theory and Measurement, *IEEE Trans. Ant. Prop.*, AP-13, pp. 550-564, 1965.
- [24] J.T. de Bettencourt, Statistics of Millimeter-Wave Rainfall Attenuation, *Journal de Recherches Atmospheriques.*, 8, pp. 89-119, 1974.
- [25] R.A. Porter, An Analytical Study of Measured Radiometric Data, Vol. I, *Radiometric Technology Inc.*, JPL Contract 952397, NASA Accession No. N 70-20193, Dec 1969.
- [26] W.T. Kreiss, The Influence of Clouds on Microwave Brightness Temperatures Viewing Downward Over Open Seas, *Proc. of the IEEE.*, vol. 57, no. 4, pp. 440-446, April 1969.
- [27] S.L. Valley, *Handbook of Geophysics and Space Environment*, McGraw-Hill Book Company, New York, 1965.

- [28] B.J. Mason, *The Physics of Clouds*, Oxford University Press, Amen House, London, pp. 94-95, 1957.
- [29] X. Weizhaung, A Satellite Based Radar Wind Sounder, Dissertation, University of Kansas, 1990.
- [30] D. Deirmendjian, Scattering and Polarization Properties of Water Clouds and Hazes in the Visible and Infrared, *Applied Optics*, vol. 3, no. 2, pp. 187-196, 1964.
- [31] D. Deirmendjian, *Electromagnetic Scattering on Spherical Polydispersions*, Chapter 3, American Elsevier Publishing Company, Inc, New York, 1964.
- [32] E.C. Reifstein, N.E. Gaut, Microwave Properties of Clouds in the Spectral Range 30-40 GHz, Tech. Rep. No. 12, Environ. Res. and Tech., Inc., 1971.
- [33] M.T. Chahine *et al.*, *Manual of Remote Sensing*, R.N. Colwell, ed., vol. I, 2ed., Chapter 5, American Society of Photogrammetry, 1983.
- [34] S.T. Wu, A.K. Fung, A Theory of Microwave Apparent Temperature Over the Ocean, *NASA Contractor Report*, NASA CR-2329, Nov. 1973.
- [35] George Dome, Oceanic wind vector determination using SEASAT satellite, D. Eng. thesis, University of Kansas., Lawrence, 1980.
- [36] George Dome *et al.*, Use of a Satellite Multi-Frequency Radiometer to Determine Attenuation Suffered by a Satellite Radar *AGARD Conf. Proc.*, no. 284, NATO AGARD, Neuilly-sur-Seine, France, pp. 20-1 to -12.
- [37] F.T. Ulaby, R.K. Moore, A.K. Fung, *Microwave Remote Sensing*, vol. III, Addison-Wesley Publishing Company, Reading, Massachusetts, 1981.
- [38] Julius Goldhirsh, Bert Musiani, Rain Cell Size Statistics Derived from Radar Observations at Wallops Island, Virginia, *IEEE Trans. on Geoscience and Remote Sensing*, Vol. GE-24, No. 6, Nov 1986, pp. 947-954.

CRINC

